CONGO WETLANDS HYDROLOGY USING SAR, INSAR, AND RADAR ALTIMETRY

A Dissertation

Presented to

the Faculty of the Department of Civil and Environmental Engineering

University of Houston

In Partial Fulfillment

of the Requirements for the Degree of

Doctor of Philosophy

in Geosensing Systems Engineering and Sciences

by

Ting Yuan

May 2017

CONGO WETLANDS HYDROLOGY USING SAR, INSAR, AND RADAR ALTIMETRY

Ting Yuan

Approved:

Chair of the Committee
Hyongki Lee, Ph.D.
Assistant Professor
Civil & Environmental Engineering

Committee Members:

Ramesh L. Shrestha, Ph.D.
Hugh Roy & Lillie Cranz Cullen
Distinguished Professor
Civil & Environmental Engineering

Craig L. Glennie, Ph.D.
Associate Professor
Civil & Environmental Engineering,

R. Edward Beighley, Ph.D.
Associate Professor
Civil & Environmental Engineering
Northeastern University

Hahn Chul Jung, Ph.D.
Lead Research Scientist
Hydrological Sciences Laboratory
NASA Goddard Space Flight Center

Suresh K. Khator, Ph.D.
Associate Dean
Cullen College of Engineering

Craig L. Glennie, Ph.D.
Geosensing Systems Engineering &
Sciences Program Director

Acknowledgement

I am profoundly grateful to my advisor, Dr. Hyongki Lee, for his support, guidance and encouragement. Dr. Lee introduced me into the area of remote sensing of hydrology. He has mentored me in building relevant background, research, and writing skills throughout my graduate studies. He has also been supportive in funding me to attend conferences, workshops, and his immense guidance towards the success of the NESSF fellowship I received. These invaluable experiences will serve as a leverage towards the next phase of my career. Without his support, this piece of work would not be possible. I would like to thank Dr. Hahn Chul Jung for his assistance in helping me set up InSAR processing in my early study phase, for his patience in illustrating hydrological models, and for his insightful comments to my research. I would like to thank Dr. Edward Beighley for his indispensable collaboration for providing HRR output for my research. I also would like to thank Dr. Ramesh Shrestha and Dr. Craig Glennie for serving as my committee members. Special thanks go to Dr. Douglas Alsdorf for his sharing ideas and continuous encouragement to a nascent researcher.

I would like to express my gratitude to all the group members: Ning Cao, Donghwan Kim, Zhiyue Sun, Modurodoluwa Okeowo, Hanwen Yu, Chi-Hung Chang and Abureli Aierken. The group meetings have always been fun and I have benefited from it a lot. I would like to thank Andrea Albright for proofreading my dissertation. Also, I would like to thank other colleagues in the NCALM laboratory: Preston Hartzell, Zhigang Pan, Xiao Zhang, Hongzhou Wang, Xiao Wang for their help during my stay in Houston. I also would like to thank Laura Murphy for her care and help.

Last but not the least, I would like to thank my family for their enduring love, patience and support.

This research was supported by NASA's Earth and Space Sciences Fellowship (NNX15AM70H), New Investigator Program (NNX14AI01G) and GRACE Program (NNX12AJ95G). The provision of ALOS PALSAR data from Japan Aerospace Exploration Agency (JAXA) and Alaska Satellite Facility (ASF), Envisat altimetry data from European Space Agency (ESA) are gratefully acknowledged.

CONGO WETLANDS HYDROLOGY USING SAR, INSAR, AND RADAR ALTIMETRY

An Abstract

of a

Dissertation

Presented to

the Faculty of the Department of Civil and Environmental Engineering

University of Houston

In Partial Fulfillment

of the Requirements for the Degree of

Doctor of Philosophy

in Geosensing Systems Engineering and Sciences

by

Ting Yuan

May 2017

Abstract

Extensive wetlands expand along the banks of the Congo river and its tributaries. Estimating wetlands water storages as well as its sources and sinks is of great importance to understand water balances in the fluvial systems and the role of wetlands in nutrient and sediment transport. In this dissertation, Synthetic Aperture Radar (SAR), Interferometry SAR (InSAR), and radar altimetry are deployed to study the spatio-temporal variations of water level changes ($\partial h/\partial t$) and water storages, and the influxes and effluxes through the wetlands. First, a regression model integrating PALSAR backscattering coefficient (σ_0), Envisat altimetry, and MODIS VCF is proposed to estimate $\partial h/\partial t$ in the Malebo Pool where non-forested and forested vegetations exist. The accuracy of σ_0 method is adequate in non-forested regions where InSAR could lose coherence during high water level, whereas the accuracy degrades in dense forested wetlands where InSAR could maintain coherence to measure relative $\partial h/\partial t$. Therefore, a stack of PALSAR interferograms are generated to map multi-temporal high spatial resolution $\partial h/\partial t$ over the forested wetlands near city Lisala. The InSAR measurements show that $\partial h/\partial t$ is subtle and the water flow is not well confined during low water seasons while $\partial h/\partial t$ shows greatest gradient perpendicular to river flow direction in high water seasons. Next, a new method is developed to reveal the inter-annual absolute water storages by integrating spatially varying $\partial h/\partial t$ and time series of water depth from Envisat altimetry. The mean annual amplitude over the studied 7,777 km^2 wetlands from 2002 to 2011 is 3.98$\pm$0.59 km^3, with maximum water volume to be 6.3$\pm$0.68 km^3 in the wet year of 2002 and minimum volume to be 2.2$\pm$0.61 km^3 in the dry year of 2005. Finally, mass balance analysis results suggest

that local water (i.e. upland runoff and rainfall) contributes more than 85% of total inflow while regional water (i.e. wetland river exchanges) supplies less than 15% of total inflow. Wetland river exchanges contribute 59% to 80% to the total outflow while evapotranspiration contributes 20% to 41% of the total outflow. A wetland model was applied to derive two site specific hydrological parameters, flow conductance (K_f) and depth exponent (β).

Table of Content

List of Figures

List of Tables

Chapter 1 Introduction

1.1 Statement of Problem

Wetland is among the most distinctive landscape features on earth (*Tockner and Stanford*, 2002). Its functions such as water buffering, carbon storage, biodiversity maintenance, fish production and aquifer recharge (*Keddy et al.*, 2009) are all related to human life. Wetlands formation and maintenance are highly connected to their seasonal flood dynamics (*Hughes*, 1997; *Ward et al.*, 1999; *Tockner and Stanford*, 2002). During water residence in the wetland, biogeochemical environment of the floodwater is modified due to the influence of sedimentation, sorption and redox reactions and biotic processes (*Richey et al.*, 1989; *Hamilton*, 2002). Different water sources could make a difference in the sediment supplies, carbon and nutrient exchange. The hydrology and hydrodynamics of wetlands are essential to understand the flux of sedimentation, nutrient and other solutes (*Richey et al.*, 1989; *Dunne et al.*, 1998; *Hamilton*, 2002) through wetlands as well as the impacts of flooding and droughts to the wetland ecosystem.

The Congo River meandering over 4,374 km is the world's second largest river in terms of discharge (41,000 m^3/s) and drainage area (3.7 million km^2) (*Lehner et al.*, 2008). It is not only an important transportation route and lifeline, but also provides food and fishery to the Congolese people. The elevation of Congo River decreases only 115 m through its middle reach from Kisangani to Kinshasa by traversing the "shallow bowl", *cuvette centrale congolasise* (*Hughes*, 1992). Extensive wetlands and swamps, estimated to be 190,000 km^2, expand along the banks of the river and its tributaries (*Hughes*, 1992; *Keddy et al.*, 2009). The Congo wetlands play an important role in regulating global water

and carbon cycles, climate and environments (*Barbier*, 1994; *Neue et al.*, 1997; *Hayashi et al.*, 1998). Despite its enormous size and significance to global and regional climate and environment, Congo Basin is one of the least studied major river basins and little is known about its hydrology and hydrodynamics (*Keddy et al.*, 2009). The number of peer-reviewed papers related to Congo Basin hydrology are an order of magnitude fewer than that of the Amazon River Basin (*Alsdorf et al.*, 2016). This is mainly due to historical political instability and conflicts that have plagued this region. There were more than 400 stream gauges in the Congo Basin until 1960 while there are only about 10 operating gauges nowadays (*Alsdorf et al.*, 2016). In addition because most of the *in situ* gauges are installed in the rivers, not in the wetlands, the two-dimensional flow in the wetlands cannot be measured with the gauges (*Alsdorf et al.*, 2007a). Alternatively, remote sensing is now a viable tool to measure water over the wetlands. A review of prior studies applying remote sensing techniques to measure wetlands water are reviewed below, with a focus on radar altimetry, Synthetic Aperture Radar (SAR), and Interferometry SAR (InSAR) is given in the next section.

1.2 Measuring Wetland Water from Space

1.2.1 Satellite Altimetry in Wetland Water Level Monitoring

Satellite radar altimetry is an effective remote sensing technique in measuring water level over inland water bodies. Initial efforts of applying satellite altimetry for continental water bodies started in 1987 (*Rapley et al.*, 1987). Later, several studies applied high-rate range measurements contained in Geophysical Data Record (GDR) from TOPEX to study inland water level (*Birkett*, 1995, 1998; *Kouraev et al.*, 2004). Significant amounts of data

loss occurred during periods of low water level because the returned waveform is biased by the interruptions of surrounding topography. This limitation can be overcome by retracking individual return waveforms (*Berry et al*, 2005; *Frappart et al.*, 2006). Among the four retracking algorithms (Ocean, Ice-1, Ice-2, Sea Ice) applied to Envisat RA-2 raw-data, Ice-1 algorithm provides most suitable measurements for inland water bodies (*Frappart et al.*, 2006). Retracked radar altimetry measurements have been successfully applied to measure water levels over both open water and water surfaces beneath vegetation (e.g., *Frappart et al.*, 2005, 2006a; *Kim et al.*, 2009; *Lee et al.*, 2011, 2015; *Yuan et al.*, 2015). The unique ability of radar altimetry for measuring both open and vegetated water surface has enabled the hydraulic analysis between the channel and adjacent wetlands in the Congo (*Lee et al.*, 2011) and Amazon Basins (*Da Silva et al.*, 2012). In addition, measurements from radar altimetry have a single fixed datum (*Birkett et al.*, 2002) and it is able to measure absolute water level changes ($\partial h/\partial t$) in the channel and wetlands (*Kim et al.*, 2009; *Lee et al.*, 2014). However, radar altimetry is a profiling tool providing measurements only along its ground tracks and the cross-track resolution of satellite altimetry is low (e.g. 80 km for Envisat at the equator). Thus, substantial water bodies located between its ground tracks cannot be sampled by radar altimetry.

1.2.2 SAR Observations in Wetland Hydrology

As an active microwave sensor, Synthetic Aperture Radar (SAR) has all-day and all-weather imaging capability. SAR images have been successfully used to map wetlands vegetation and inundation extent with high spatial resolution (30 – 100 m). The SAR images are composed of both intensity and phase information. SAR intensity data is usually

converted to backscattering coefficient (σ_0) to map wetlands flood extent and vegetation types. The performance of the SAR systems in mapping flooded extents beneath vegetated region depends on their polarization modes and wavelengths. Horizontal-Horizontal (HH) polarization SAR images are optimal in differentiating flooded and non-flooded areas beneath vegetation canopy regardless of wavelengths (*Hess et al.*, 1995). A SAR system with longer wavelength has better canopy penetration capability than shorter wavelength. C-band sensors with a wavelength of 5.7 cm can penetrate herbaceous vegetation but are not able to penetrate closed forest canopy. On the other hand, L-band sensors with a wavelength of 24 cm can penetrate both herbaceous vegetation and forest canopy (*Hess et al.*, 1995). L-band SAR sensors on board Japan Earth Resources Satellite (JERS-1) and Advanced Land Observation Satellite (ALOS-1) have demonstrated their ability to map wetland inundation in large river basins with dense vegetation canopy, such as the Congo and Amazon Basins (*Rosenqvist and Birkett*, 2002; *Hess et al.*, 2003; *Lee et al.*, 2014). In addition, *Trung et al.* (2013) studied changes in land cover classes in the Tonle Sap wetland using Phase Array L-band Synthetic Aperture Radar (PALSAR) and Moderate Resolution Imaging Spectroradiometer (MODIS) data with a land cover model as a function of water level.

There have been efforts to quantify the relation between hydrologic conditions and backscattering coefficient (σ_0) using theoretical scattering models. For example, *Kasischke et al*. (2003) correlated C-band ERS-2 σ_0 with regional hydrologic changes, vegetation types, and biomass in the Everglades wetlands of Florida. They found that the ERS-2 σ_0 is closely related to both soil moisture and water level changes in the Marl Prairie sites. *Grings et al.* (2006, 2008) used C-band Envisat ASAR images with electromagnetic

models, and hydrological and vegetation data from fieldwork to examine SAR backscatter responses to water level changes over marshes in the Parana River Delta. *Kim et al.* (2014) has investigated the influence of water level changes on PALSAR σ_0 and developed a regression method to estimate water level changes by differencing PALSAR σ_0.

Apart from using SAR σ_0, SAR Interferometry (InSAR) using the phase differences between two SAR images has demonstrated its ability to map two-dimensional water level changes with high spatial resolution (~30 m) and high accuracy (centimeter level). The capability of InSAR to explore $\partial h/\partial t$ in wetlands was first demonstrated by *Alsdorf et al.* (2001) using L-band HH-polarized SIR-C data over the Amazon wetland. InSAR-derived spatially dense $\partial h/\partial t$ measurements were then utilized to map the passage of a flood wave in the Amazon wetland using L-band JERS-1 data (*Alsdorf et al.*, 2007a). *Wdowinski et al.* (2008) also used the JERS-1 SAR data to map the $\partial h/\partial t$ over the Everglades wetlands in Florida. Besides the L-band SAR data, *Lu and Kwoun* (2008) found that interferograms generated with C-band Radarsat-1 and ERS SAR data can also maintain adequate coherence under medium-low canopy closure over the Louisiana swamp forests. The advantage of this InSAR technique is that it provides highly accurate water level changes over the vegetated wetlands with high spatial resolution (usually 10 – 30 m). However, there exists several shortfalls as well. First, a coherent SAR pair, constrained by temporal and spatial baselines and surface scattering characteristics, is required to generate the interferogram (*Jung and Alsdorf*, 2010). Secondly, the interferograms may only be generated over the wetlands with stable trunks of vegetation (e.g., swamp forests) (*Alsdorf et al.*, 2001; *Lu and Kwoun*, 2008; *Wdowinski et al.*, 2008) or structures (*Kim et al.*, 2005) which enable the reflected radar signal to follow the double-bounce travel path. Finally,

the interferograms generated from InSAR can only provide a spatially relative gradient of water level changes.

1.2.3 Integration of SAR and Radar Altimetry in Wetland Hydrology

SAR and altimetry have distinct advantages and limitations in measuring wetlands hydrology. SAR images have good spatial coverage and resolution in mapping inundated extents but does not measure water level. InSAR is able to provide high spatial resolution relative $\partial h/\partial t$ but needs vertical reference to obtain absolute $\partial h/\partial t$. Radar altimetry is able to measure water level in both wetlands and open water surface. But it cannot map water extent or spatially detailed water level changes. Complementary characteristics of the two techniques imply enhanced ability to monitor wetlands hydrology by combining them. Integration of the two measurements has been successful using three strategies.

The first strategy is integrating inundation extents from L-band SAR σ_0 and water level from radar altimetry to estimate water storage changes in the large river basins (*Frappart et al.*, 2005; *Lee et al.*, 2014). This method is useful to quantify wetlands water storage changes which is a key, governing parameter in continental scale hydrological modelling (*Richey et al.*, 1989; *Vörösmarty et al.*, 1989; *Coe*, 1998). The second strategy is constructing regression models with PALSAR σ_0 and water level measurements from altimetry to map water depth in the flooded forests with high spatial resolution (*Lee et al.*, 2015). The methods relying on the L-band SAR backscattering coefficients to estimate the flooded extents or water depth are only limited by the temporal coverage of the SAR data (*Prigent et al.*, 2007; *Aires et al.*, 2013). In other words, since the preferred L-band wavelength SAR data for studying forested wetlands is only provided by a few satellites

of JERS-1 (1992 – 1997), ALOS (2006 – 2011), and ALOS-2 (2014 – present), there is a significant time gap that is not covered by these datasets (e.g. 1998 – 2005). Moreover, the long revisiting periods of JERS-1 (44 days) and ALOS (46 days) can result in missing the flood peaks.

The third strategy is to obtain high spatial resolution absolute water level change maps by integrating radar altimetry and InSAR measurements. Radar altimetry derived absolute water level change can be used as a vertical reference for InSAR measured two dimensional relative water level change map (*Kim et al.*, 2009). Spatially detailed water level change maps provide opportunity to investigate hydraulics of complex water flow, subjected to bathymetry and hydraulic variations (*Alsdorf et al.*, 2007a; *Jung et al.*, 2010). These maps are also useful to calibrate wetland hydrodynamic models (*Jung et al.*, 2012). The limitation of this method lies in the availability of InSAR measurements, which is constrained by its coherence.

1.3 Motivation and Objectives

From the last section, there are two ways to measure spatially detailed $\partial h/\partial t$ in the wetlands: 1) correlating SAR σ_0 and water level with a regression or electromagnetic model; 2) integrating InSAR derived relative $\partial h/\partial t$ with a vertical reference from radar altimetry or *in situ* gauges. Several studies have focused on mapping inundation extents in Congo wetlands using SAR σ_0 (*Rosenqvist and Birkett*, 2002; *Rosenqvist*, 2008; *Lee et al.*, 2014). *Rosenqvist and Birkett* (2002) generated two high spatial resolution (~100 m) inundation maps over the whole Congo Basin using L-band JERS-1 mosaics, and suggested that at least three SAR acquisitions within one year would be sufficient to describe the

complex hydrology in the Congo Basin. *Rosenqvist* (2008) presented multi-temporal inundation maps and mapped flooding duration in the Congo Basin with ALOS ScanSAR images. *Lee et al.* (2014) delineated the inundation extents of the flooded forest, herbaceous wetlands, and open water in the *Cuvette Centrale* with PALSAR ScanSAR. *Lee et al.* (2015) developed a regression model with PALSAR ScanSAR, Envisat altimetry and MODIS Vegetation Continuous Fields (VCF) to generate three water depth maps over the forested wetlands in the *Cuvette Centrale*. Since SAR σ_0 has only been used to map flooding extents or water depth in the forested wetlands, its ability to measure $\partial h/\partial t$ over different vegetation fields has not been explored. The first objective of this dissertation is to examine temporal variability of SAR σ_0 in the Congo wetlands over different vegetation fields and explore its ability to measure $\partial h/\partial t$ with Envisat altimetry and MODIS VCF.

In addition, only a couple of studies have used InSAR and satellite altimetry data to map spatially detailed $\partial h/\partial t$ of the Congo's wetlands. *Jung et al.* (2010) used two interferograms generated with L-band JERS-1 images obtained in 1996 over the interfluvial wetlands near the confluence of the mainstem and its major tributaries including the Ubangi and Sangha, and reported that the flow patterns are not well defined and have diffuse patterns. *Lee et al.* (2015) generated two PALSAR interferograms over similar central regions and revealed dense fringe patterns showing increasing $\partial h/\partial t$ toward the mainstem. Since multi-temporal $\partial h/\partial t$ and hydraulic processes have not been extensively investigated, the second objective is to generate multiple $\partial h/\partial t$ maps with PALSAR images over the middle reach of the Congo near the city of Lisala, and to quantify and characterize the flow dynamics in the wetlands.

Lee et al. (2011) quantified the water filling and draining the entire Congo wetlands to be 111 km^3 with multiple remote sensing techniques, including GRACE, JESR-1 SAR images, Shuttle Radar Topography Mission (SRTM) Digital Elevation Model (DEM) and MODIS. *Lee et al.* (2014) estimated the water storage changes over the flooded forest, herbaceous wetlands, and open water in the *Cuvette Centrale* using PALSAR ScanSAR and Envisat altimetry measurements from 2006 to 2010, and concluded that GRACE-derived TWS changes are mostly controlled by surface water storage changes. However, long-term local scale water storages over the wetlands are not known due to lack of temporal coverage of SAR images. Therefore, another key target of this dissertation is to estimate water storage variations by developing a model between water depths and storages.

Water storage changes in wetlands is usually the composite consequences of different influxes and outfluxes. Different water sources could make a difference in the sediment supplies, carbon and nutrient exchange. Few studies have investigated the sources and sinks of the water in the Congo wetlands. *Lee et al.* (2011) has investigated the source and amount of water in the Congo wetland in sub-basin scale and concluded that local water is the main source of Congo's wetlands water. However, quantitative estimations of the wetlands sources and sinks have not been reported yet. The last objective of this dissertation is to investigate influxes and outfluxes of the Congo wetlands.

In summary, the objective of this dissertation is to further improve our understanding of the Congo wetlands hydrology in finer temporal and spatial scales by innovatively integrating data from radar altimetry, InSAR and SAR. The scientific questions of this research to address are as follows: What is the spatio-temporal variations

of $\partial h/\partial t$ in the Congo wetlands? What is the inter-annual variations of water storages in the Congo wetlands and what contributes to its inter-annual variations? How does the water fill and leave the Congo wetlands?

1.4 Document Structure

Chapter 2 reviews the data processing of satellite altimetry and InSAR.

Chapter 3 examines seasonal variations of ALOS PALSAR σ_0 in the Malebo Pool where non-forested and forested vegetation are found. A regression model integrating PALSAR σ_0, Envisat altimetry, MODIS VCF was proposed to estimate $\partial h/\partial t$.

Chapter 4 generates fifteen interferograms from ALOS PALSAR to map the multi-temporal $\partial h/\partial t$ over the forested wetlands along the middle reach of the Congo main-stem using the Small Temporal Baseline Subset (STBAS) strategy.

Chapter 5 develops a new method to estimate absolute water storages over the wetlands by establishing relations between water depths (d) and water volumes (V) using 2-D water depth maps from the integration of InSAR and altimetry measurements.

Chapter 6 investigates fluxes across the Congo wetlands using mass balance equation. A wetland model integrating water surface slope, water depth from satellite altimetry was applied to derive hydrological parameters K_f and β which are specific to the Congo wetlands.

Chapter 7 summarizes the main results and conclusions. Several recommendations for future research are outlined.

Chapter 2 Theoretical Background

2.1 Satellite Altimetry

2.1.1 Satellite Altimetry Measurement Principles

Satellite altimetry was initially designed to measure sea surface height. It measures sea surface elevation by transmitting a nadir-looking electromagnetic pulse travelling at the speed of light and measuring its two-way travel time when the return from the instantaneous sea surface is received, as shown

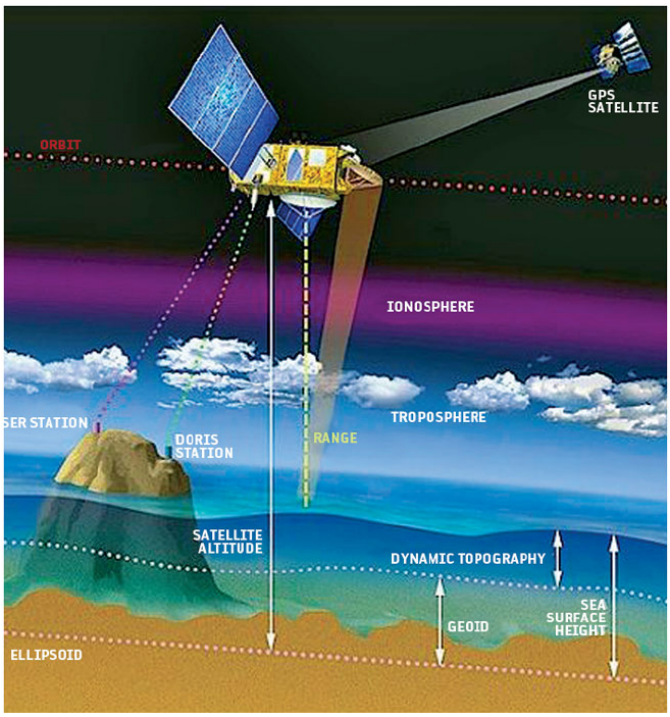

Figure 2-1 Concept of satellite altimeter. (Courtesy of ESA)

Distance between the antenna and the earth surface can be written as

$$R = ct/2, \tag{2-1}$$

where R is measured distance between satellite antenna and sea surface, c is speed of light, and t is electromagnetic pulse two-way travel time.

Corrections including propagation corrections, surface corrections, geophysical corrections and instrument corrections (*ESA*, 2007) need to be added to get the correct distance between earth surface and satellite:

$$R_c = R + \Delta R_{wt} + \Delta R_{dt} + \Delta R_{iono} + \Delta R_{ssb} + \Delta R_{instr}, \quad (2\text{-}2)$$

where R_c is corrected distance, ΔR_{wt} is wet tropospheric correction, ΔR_{dt} is dry tropospheric correction, ΔR_{ino} is ionosphere correction, ΔR_{ssb} is sea surface bias correction, ΔR_{instr} is instrument correction.

Sea surface height can be estimated by given altitude of satellite:

$$H = H_{sat} - R_c, \quad (2\text{-}3)$$

where H is surface height, H_{sat} is altitude of satellite, R_c is corrected distance.

2.1.2 Satellite Altimetry Retracking Method

Satellite altimeter measures the ranges by recording the power distribution of reflected pulses. The on-board tracker records the radar pulses, also called waveform, in a range of gates or bins. Figure 2-2 illustrates a schematic description of a radar altimeter pulse returned from sea surface. The altimeter transmits a spherical expanding signal towards the sea surface. When the pulse hits the sea surface at nadir at $t=t_0$, the transmitted pulse illuminates the sea surface and the returned signal is measured by the altimeter antenna. While the leading edge of pulse continues illuminating the sea surface ($t_0<t<t_1$), the illuminated area on the sea surface expands and returned power increases. At the time

of trailing edge immediately arrives the sea surface $t=t_1$, the returned energy reaches its maximum. Thereafter ($t> t_1$), with the trailing edge of the pulse arriving the sea surface, the illuminated area becomes an annul and the backscattered energy to the altimeter starts to decay. Over calm sea surfaces, the waveform has a straight rapid leading edge and a slowly decaying trailing edge.

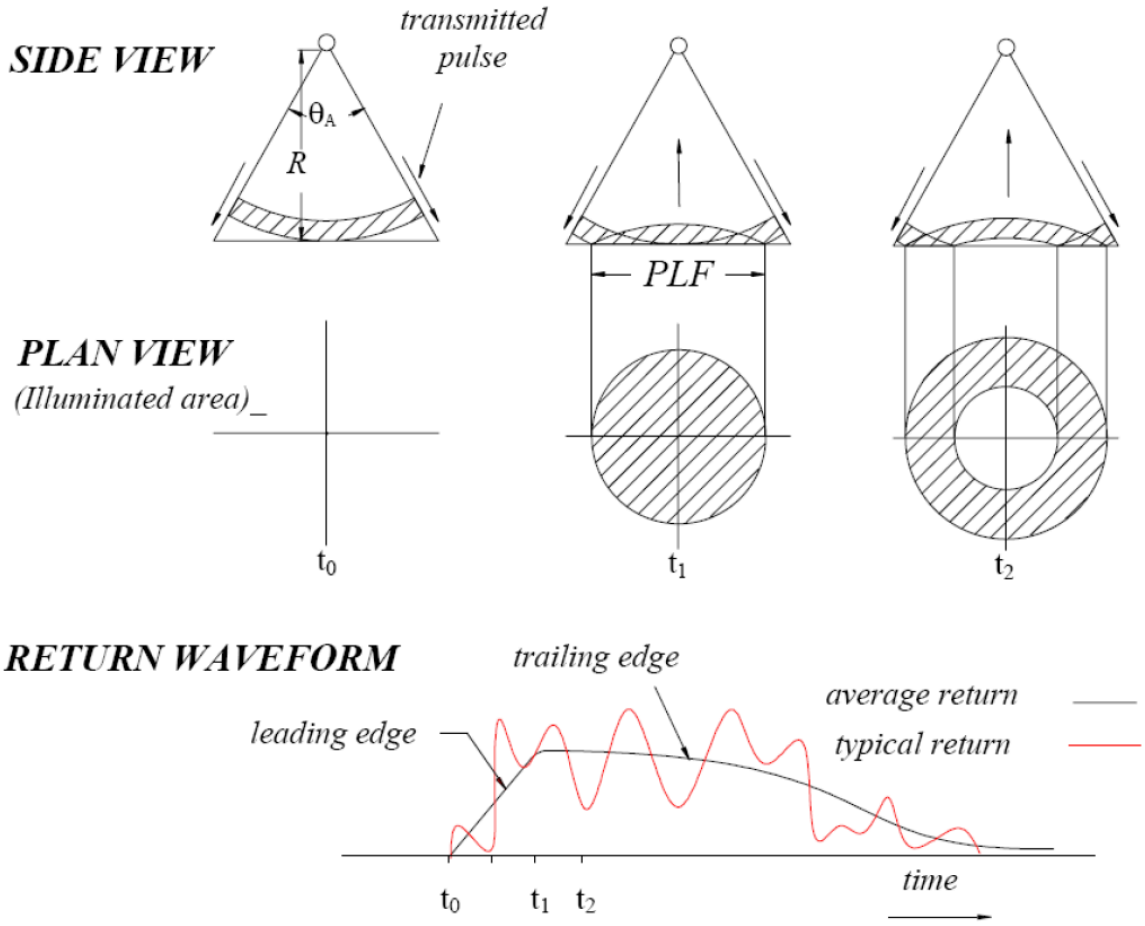

Figure 2-2 Interaction of transmitted pulse from altimeter, illuminated area on the sea surface and corresponding recorded returned waveform. PLF stands for pulse-limited footprint and θ_A is antenna beam width (*Deng*, 2003).

Although satellite altimetry was initially designed to measure sea surface height, it has been successfully used for non-ocean surfaces, including ice-sheets, lakes, rivers and

wetlands. Since the non-ocean surfaces have different characteristics, different retracking methods have been developed to address these differences, including NASA β-retracker (*Zwally*, 1996), surface/threshold retracker (*Davis*, 1997), Offset Center of Gravity (OCOG), also known as ICE-1 (*Wingham et al.*, 1986; *Bamber*, 1994), ICE-2 (*Legresy and Remy*, 1997) and SEA ICE retracker (*Laxon*, 1994). Among all the tracking methods, ICE-1 algorithms has been demonstrated to provide more accurate water level measurements (*Frappart et al.*, 2006). Since ICE-1 retracking measurements from Envisat RA-2 are the only retracking measurements used in this dissertation, ICE-1 retracking algorithm is introduced as follows. Figure 2-3 illustrates the schematic plot of OCOG algorithm.

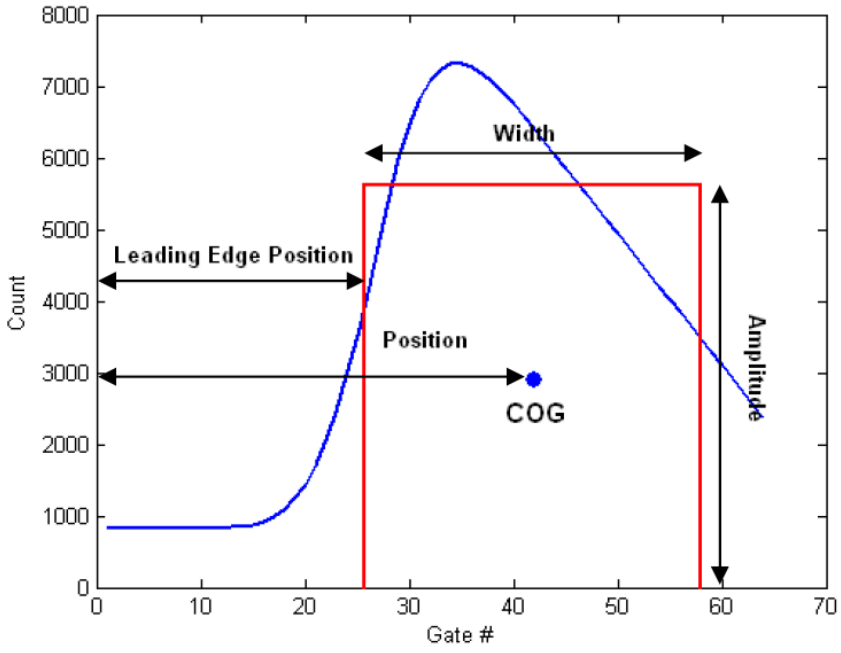

Figure 2-3 Schematic plot of OCOG retracker (From (*Lee*, 2008)).

$$\mathrm{COG} = \sum_{i=1+n_a}^{64-n_a} iP^2(i) \Big/ \sum_{i=1+n_a}^{64-n_a} P^2(i), \tag{2-4}$$

$$\text{Amplitude} = \sqrt{\sum_{i=1+n_a}^{64-n_a} P^4(i) / \sum_{i=1+n_a}^{64-n_a} P^2(i)}, \text{ and} \quad (2\text{-}5)$$

$$\text{Width} = \left(\sum_{i=1+n_a}^{64-n_a} P^2(i)\right)^2 / \sum_{i=1+n_a}^{64-n_a} P^4(i). \quad (2\text{-}6)$$

The leading edge position (LEP) is estimated using

$$LEP = COG - Width/2. \quad (2\text{-}7)$$

2.2 Interferometric SAR

InSAR processing consists of two or more SAR images. SAR images can be collected in three different modes: dual-antenna standard mode composed of single transmitter and dual antenna, dual-antenna "ping-pong" mode composed of two transmitters and two antennas, and repeat-pass mode composed of single transmitter and single antenna. Repeat-pass mode collects SAR images at different times which is the mode used for spaceborne platforms. In this dissertation, repeat-pass mode will be assumed, unless otherwise noted. This section will describe the algorithms for InSAR data processing from geometric views and demonstrate intermediate results in InSAR processing with an interferogram example generated using L-band ALOS PALSAR images.

2.2.1 Overview of InSAR Processing

SAR interferometry processing involves two SAR images illuminating the same region with the antenna at slightly different positions. The SAR interferometric processing flow is shown in Figure 2-4. A pair of ALOS PALSAR images obtained on August 4, 2007 and December 20, 2007 are used to illustrate this process. GAMMA software packages (*Werner et al.*, 2000) are used for the InSAR processing in this dissertation.

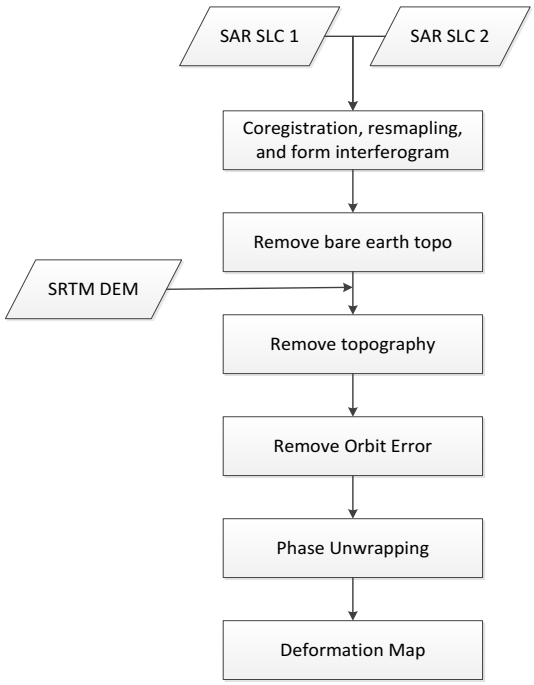

Figure 2-4 Flow chart of InSAR data processing.

SAR images are complex data composed of both intensity and phase information, named Single Look Complex (SLC) data before multi-looking. Assume S_1 is master image or reference image and S_2 is the slave image. Each SAR image can be written as

$$S_1 = U_1 \exp(\mathrm{i}\varphi_1), S_2 = U_2 \exp(\mathrm{i}\varphi_2), \tag{2-8}$$

where S_1, S_2 are complex values of SAR images, U_1 and U_2 are SAR images intensity values, φ_1 and φ_2 are SAR images phase information. Figure 2-5 shows two multi-look complex ALOS PALSAR images. It is noted that the phase data in the SAR images are modulo of 2π.

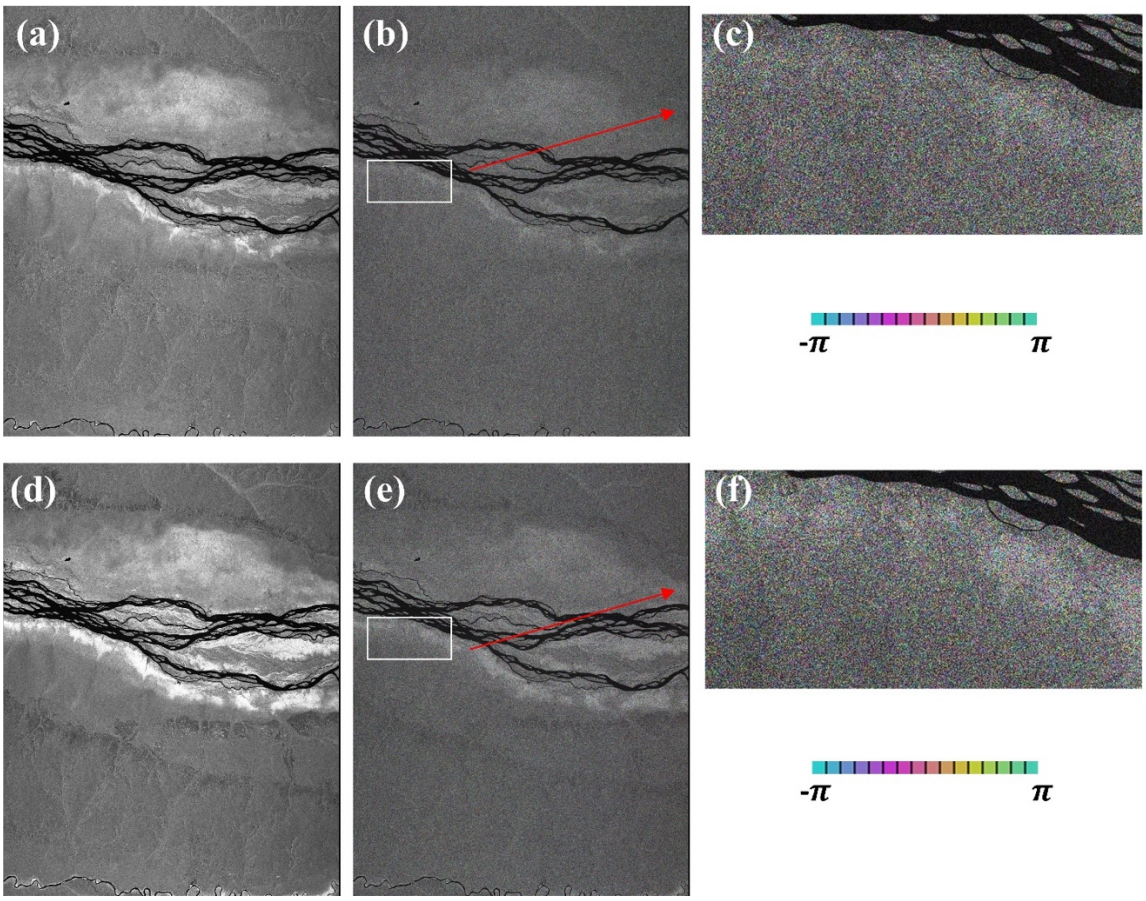

Figure 2-5 Intensity, phase and zoom-in phase of two complex ALOS PALSAR images obtained on Aug 4, 2007 (a, b, c) and Dec 20, 2007 (d, e, f). from ALOS PALSAR.

2.2.2 InSAR Geometry

Radar interferometry geometry is given in Figure 2-6. The plane of Figure 2-6 is the *imaging plane* and is normal to the satellite flight direction. The direction along the flight track, which is perpendicular to the plane of the page or image plane, is called "along track direction" or "azimuth direction". The direction of transmitting microelectronic wave is called range direction or line of sight (LOS).

Assuming two SAR images are acquired by antenna at A_1 and A_2, imaging a point *P* on the surface with elevation of z. The SAR image obtained by SAR antenna at A_1 with

height h above reference surface is called the master or reference image. For a given point P on the ground with topographic height z, it is imaged by antenna at A_1 with range ρ_1 and look angle θ. The second SAR image is obtained by antenna at A_2, which is called the slave image. The slave SAR image illuminates point P with range ρ_2. The separation of the antenna at A_1 and A_2 is called baseline B. The component parallel to the line of sight is called parallel baseline $B_{\parallel}$ while the one perpendicular to the line of sight direction is called perpendicular baseline $B_{\perp}$.

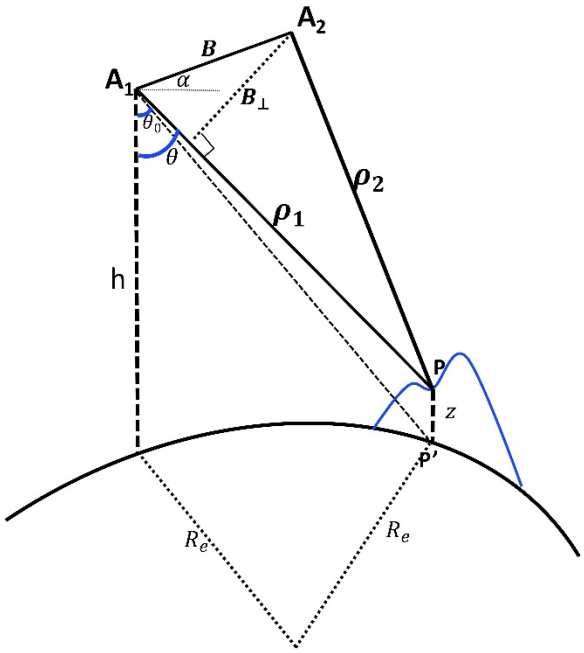

Figure 2-6 Geometry of SAR interferometry in the plane normal to azimuth direction.

2.2.3 Interferogram Formation

The generation of interferograms requires SAR images to be coregistered with sub-pixel accuracy. The coregistragion process is usually done in two steps. The first step is to estimate initial azimuth and range offsets from satellite orbital information and a moving window approach. The second step is to resample the slave image to the reference of the master image.

After resampling of the slave image, the interferogram can be generated by cross-multiplying the master SAR image and the conjugate complex of the co-registered slave SAR image, such as

$$\varphi = S_1 S_2^*. \tag{2-9}$$

By recalling SAR geometry shown in Figure 2-6, the phases φ_1 and φ_2 of SAR images are functions of distance between the antenna and surface object, which can be expressed as

$$\varphi_1 = \frac{4\pi}{\lambda}\rho_1, \ \ \varphi_2 = \frac{4\pi}{\lambda}\rho_2. \tag{2-10}$$

The interferometry phase is the phase difference between the two SAR images:

$$\varphi = \varphi_2 - \varphi_1 = \frac{4\pi}{\lambda}(\rho_2 - \rho_1), \text{ and} \tag{2-11}$$

$$\delta\rho = \rho_2 - \rho_1. \tag{2-12}$$

Figure 2-7 demonstrates an interferogram generated from the two SAR images shown in Figure 2-5. The interferogram contains dense fringes, which can be observed in Figure 2-7 (b). It should be noted that the interferometric phase is computed by calculating the arctangent of the ratio of imaginary part and the real part of the complex interferogram. Thus, the value of interferometric phase is wrapped between -π and π.

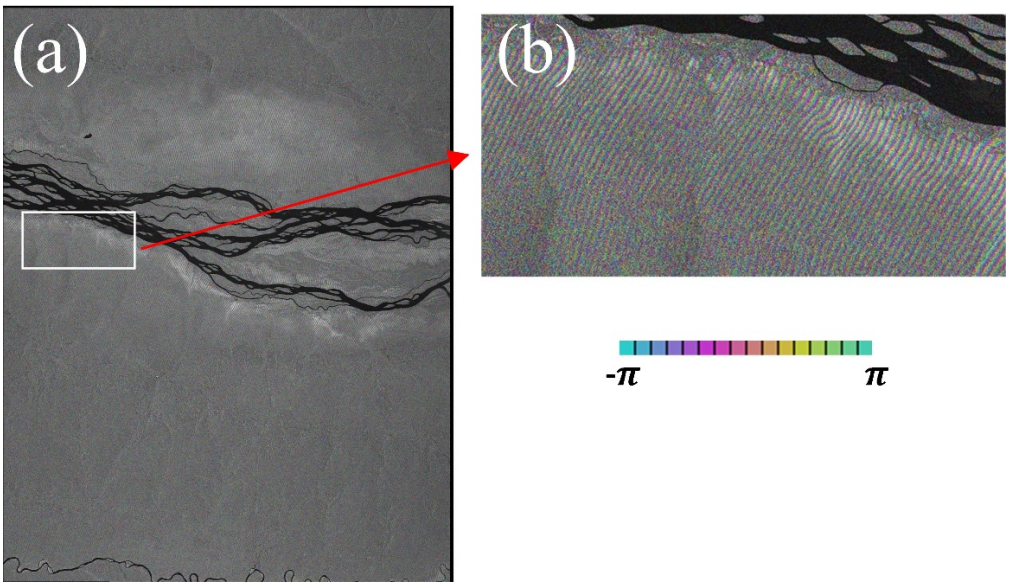

Figure 2-7 (a) The complex interferogram generated from two SAR images in Figure 2-5. (b) Zoom-in of the region enclosed in the white box in (a).

2.2.4 InSAR Flattening

The interferogram in Figure 2-7 shows dense fringes across the image which makes it difficult to extract useful signals, such as topographic height or surface deformation from the interferometric phase. The following section will describe algorithms to remove phase contributions from reference surface based on the geometry shown in Figure 2-6.

From the law of cosines for triangular A_1A_2P in Figure 2-6, we have the following relationship for ρ_1, ρ_2 and baseline B:

$$\cos(90° - \theta + \alpha) = \sin(\alpha - \theta) = \frac{\rho_1^2 + B^2 - \rho_2^2}{2B\rho_1}. \quad (2\text{-}13)$$

Substituting Equation (2-12) into Equation (2-13), Equation(2-13) can be simplified by assuming $B \ll \rho$:

$$\delta\rho = B\sin(\alpha - \theta) + \frac{B^2}{2\rho_1}, \quad (2\text{-}14)$$

where θ is the looking angle of antenna A_1, and α is baseline angle with respect to reference surface.

Substituting Equation (2-14) into Equation (2-11), we get

$$\varphi = \frac{4\pi}{\lambda} B \sin(\alpha - \theta) + \frac{4\pi}{\lambda} \frac{B^2}{2\rho_1}. \quad (2\text{-}15)$$

The look angle can be written as

$$\theta = \theta_0 + \delta\theta, \quad (2\text{-}16)$$

where θ_0 is the look angle on the reference surface, and $\delta\theta$ is the change of look angle due to presence of topography.

The phase contribution of the reference surface can be written as

$$\varphi_0 = \frac{4\pi}{\lambda} B \sin(\alpha - \theta_0) + \frac{4\pi}{\lambda} \frac{B^2}{2\rho_1}. \quad (2\text{-}17)$$

The process to remove the contribution of reference surface is referred to flattening. After removing the phase contributed from the reference surface, the flattened interferometric phase is:

$$\varphi_{flat} = \varphi - \varphi_0 \cong \frac{4\pi}{\lambda} B \sin(\alpha - \theta) - \frac{4\pi}{\lambda} B \sin(\alpha - \theta_0). \quad (2\text{-}18)$$

Substituting Equation (2-16) into Equation (2-18)

$$\varphi_{flat} \cong -\frac{4\pi}{\lambda} B \cos(\alpha - \theta_0)\, \delta\theta = -\frac{4\pi}{\lambda} B_{\perp 0} \delta\theta, \quad (2\text{-}19)$$

where $B_{\perp 0}$ is perpendicular baseline with respect to line of sight to P' on the reference surface.

Looking angle for P' on the reference surface can be written as

$$\cos(\theta_0) = \frac{{\rho_1}^2 + (R_h + h)^2 - (R_z + z)^2}{2\rho_1(R_h + h)}, \tag{2-20}$$

where R_h is distance of antenna A_1 to the earth center, and R_z is distance of point P to the earth center.

Substituting Equation (2-16) into Equation (2-20), we obtain

$$\delta\theta = \frac{z}{(1+h/R_h)(R_h/R_z)sin(\theta_0)}. \tag{2-21}$$

Substituting Equation (2-21) into Equation(2-19), the flattened interferometric phase can be written as

$$\varphi_{flat} \cong -\frac{4\pi}{\lambda}\frac{B_{\perp 0}}{(1+h/R_h)(R_h/R_z)\rho_1 \sin(\theta_0)} z. \tag{2-22}$$

By using this algorithm, the interferometric phase due to the reference surface can be removed. Figure 2-8(a) illustrates the interferogram after removing the phase contribution of reference surface which is also called flattened interferogram. As shown in Figure 2-8(a), most of the dense fringes in Figure 2-7 are removed.

Height ambiguity is an important quantity to interpret the flattened interferogram. It is the amount of topographic variation corresponding to one cycle interferometric phase, which can be computed by substituting 2π into Equation (2-22),

$$h_a = -\frac{\lambda}{2}\frac{(1+h/R_h)(R_h/R_z)\rho_1 \sin(\theta_0)}{B_{\perp 0}}. \tag{2-23}$$

The height ambiguity for the interferogram example in this chapter is 105 m with wavelength λ of 23.6 cm, altitude of ~700 km, semi-major axis of reference ellipsoid WGS 84 of 6378137.0 m, looking angle of 34.4º, and perpendicular baseline length of 485 m. In other words, 105 m of topographic difference can cause one fringe in the interferogram.

Apart from topographic variations, surface deformation, orbital error and atmospheric errors will also contribute to the phase variations.

2.2.5 Differential Interferogram

To obtain the surface deformation information, the topographic phase in the flattened interferogram must be removed using DEM data. SRTM DEM is used to remove the topographic phase component in this dissertation.

With the presence of deformation in the slave SAR image, the range observation for point P can be written as

$$\rho_2 = \rho_1 + \delta\rho + \Delta\rho, \tag{2-24}$$

where $\Delta\rho$ is the deformation component along LOS.

Substituting Equation (2-24) in to Equation (2-22)

$$\varphi_{flat} \cong -\frac{4\pi}{\lambda}\frac{B_{\perp 0}}{\left(1+\frac{h}{R_h}\right)\left(\frac{R_h}{R_z}\right)\rho_1 \sin(\theta_0)} z + \frac{4\pi}{\lambda}\Delta\rho. \tag{2-25}$$

For two-pass interferometry, the phase contribution from the topographic relief can be estimated by the external DEM and baseline

$$\varphi_{sim\_dem} = -\frac{4\pi}{\lambda}\frac{B_{\perp}}{\rho_1 \sin(\theta_0)} z. \tag{2-26}$$

After removing the topographic component from the flattened interferogram, a differential interferogram is generated. The relation between deformation and observed interferometric phase can be expressed as

$$\Delta\rho = -\frac{\lambda}{4\pi}\varphi_{def}. \tag{2-27}$$

Figure 2-8(b) illustrates the flattened interferogram after removing the phase contribution from topographic relief. The interferogram after removing topographic phase is also called a differential interferogram. Equation (2-27) implies that each fringe in the differential interferogram represents a half wavelength deformation. In case of ALOS PALSAR data, each fringe represents 12.8 cm of deformation in the LOS direction.

2.2.6 Orbital Error and Atmospheric Error

The upland area in Figure 2-8(b) shows a gradual trend of phase change from the bottom right corner which is likely due to orbital error. The orbital error in the interferogram is usually estimated using a first- or second-order polynomial, then removed from the differential interferograms. Figure 2-8(c) is the differential interferogram after removing the orbital error. Fringes in the interferogram in Figure 2-8(c) are mostly due to water level changes.

Atmospheric component $\Delta\varphi_{\mathrm{atm}}$ is characterized by high spatial correlation but low temporal correlation (*Berardino et al.*, 2002). This can be removed or mitigated by using a high pass filter for the pixels in the time domain or by atmospheric model (*Berardino et al.*, 2002; *Foster et al.*, 2006; *Li et al.*, 2006). As can be seen in Figure 2-8(c), the atmosphere effect is not significant. Thus, removal of atmospheric effect is not necessary in this example. However, it can hamper InSAR observation in some cases.

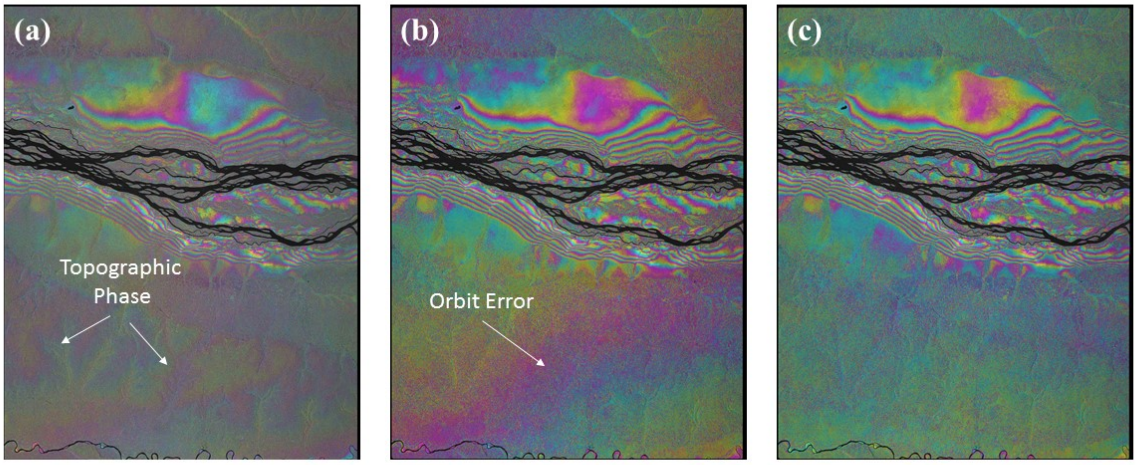

Figure 2-8 Intermediate interferograms generated from ALOS PALSAR images on Aug 4, 2007 and Dec 20, 2007.

2.2.7 Phase Unwrapping

In Figure 2-8(c), the phase in the differential interferogram represents wrapped phase which is a modulo of 2π. Unwrapping is necessary to get the continuous phase from the wrapped interferogram. Minimum cost flow is used in this dissertation to unwrap the wrapped interferogram. Figure 2-9 shows the comparison between wrapped and unwrapped phases. The wrapped phase is within the magnitude of -π and π. The process of unwrapping adds multiple of 2π to the wrapped phase.

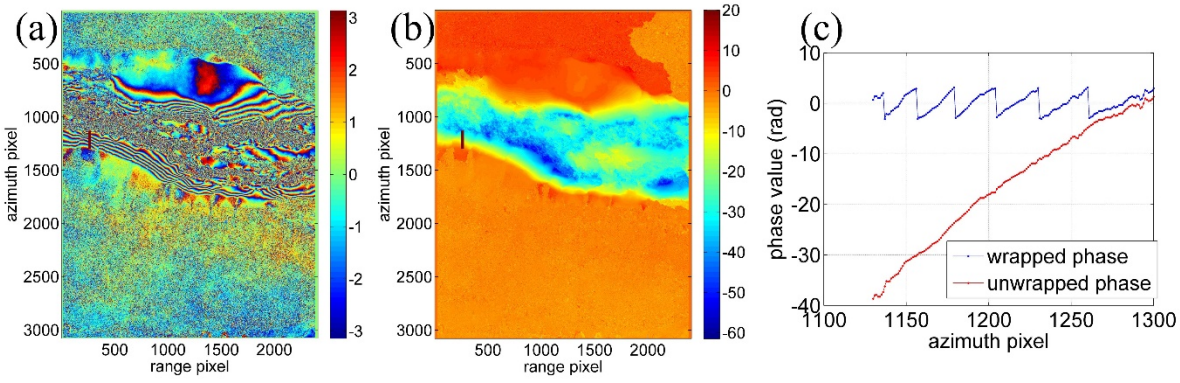

Figure 2-9 (a) Wrapped interferogram, (b) Unwrapped interferogram and (c) Comparison of wrapped and unwrapped phases along the red lines in (a) and (b).

2.2.8 InSAR Coherence

Coherence of an interferogram is used to estimate the quality of InSAR measurements is defined as below:

$$\gamma_{total} = \frac{\langle S_1 S_2^* \rangle}{\sqrt{\langle S_1 S_1^* \rangle \langle S_2 S_2^* \rangle}}. \quad (2\text{-}28)$$

The magnitude of the coherence ranges from 0 to 1. Higher coherence suggests better interferogram quality. For most cases, coherence of the interferogram is usually less than 1 due to decorrelation between the SAR images. Three major factors that contribute to decorrelation are spatial baseline decorrelation, temporal decorrelation and thermal noise (*Zebker and Villasenor*, 1992).

$$\gamma_{total} = \gamma_{thermal}\gamma_{spatial}\gamma_{temporal}, \quad (2\text{-}29)$$

where $\gamma_{thermal}$ is system noise, $\gamma_{spatial}$ is related to the platform positions during the SAR acquisition time which can be quantified by the spatial baseline between the satellite positions, and temporal decorrelation, $\gamma_{temporal}$, is caused by changes of feature surface scattering centers between the two SAR acquisitions.

Figure 2-10 presents the coherence of the interferogram in Figure 2-9.

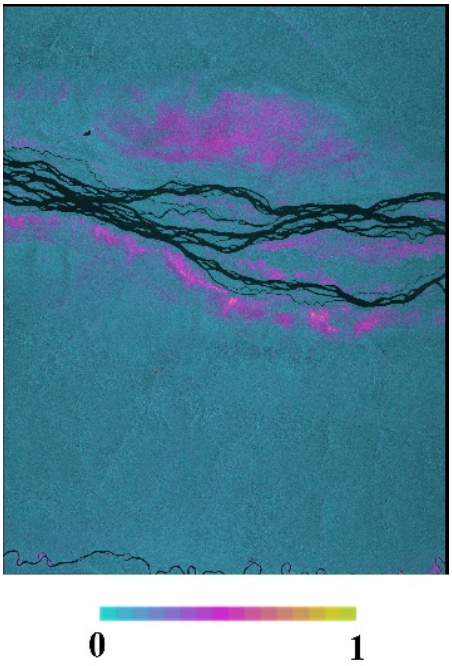

Figure 2-10 InSAR coherence for the interferograms in Figure 2-9.

Chapter 3 Towards Estimating Wetland Water Level Changes using PALSAR σ_0

3.1 Introduction

SAR σ_0 has been widely used to classify flooded and non-flooded areas with their vegetation types based on the fact that hydrological changes over wetlands can result in variations in SAR backscattering coefficients (*Hess et al.*, 2003; *Martinez and Le Toan*, 2007). Accordingly, there have been efforts to quantify the relationship between hydrologic conditions and σ_0 using theoretical scattering models (*Kasischke et al.*, 2003; *Grings et al.*, 2006, 2008). Apart from electromagnetic models, regression models have also been applied to correlate SAR σ_0 and water level changes. *Kim et al.* (2014) has investigated relationships between L-band PALSAR σ_0 and water level changes from *in situ* gauges over the Everglades freshwater marshes. However, the Everglades may be the only wetland in the world equipped with a dense network of water gauges installed for restoration projects, while most of the wetlands in the world lack cost-prohibitive *in situ* water gauges. Alternatively, satellite radar altimetry has been successfully used to monitor water level changes over rivers, lakes, and wetlands (*Birkett et al.*, 2002; *Lee et al.*, 2009). *Lee et al.* (2015) developed a regression method with PALSAR σ_0, Envisat altimetry and MODIS VCF to generate three water depth maps over the flooded forest in the central Congo Basin. Since PALSAR σ_0 has only been used to map water depth in the forested wetlands in the Congo Basin, its capability of measuring $\partial h/\partial t$ with radar altimeter measurements over different vegetation fields has not been explored. In this study, wetland water level changes

obtained from Envisat altimetry were used to investigate seasonal variations of L-band PALSAR σ_0 over different vegetation fields. In addition, because the radar backscattering mechanism depends on vegetation types as well, the VCF (*DiMiceli et al.*, 2011; *Hansen et al.*, 2013) product derived from the MODIS was used to investigate the PALSAR backscattering sensitivity to different vegetation fields under different hydrologic conditions. Finally, wetland water level changes were estimated based on the relationship between backscattering sensitivity to water level changes and VCF data, which were compared with water level changes obtained from InSAR and Envisat altimetry.

3.2 Study Area

The Congo River is the largest river in Africa with a large number of islands. The largest number of channels and islands are found in the Malebo Pool, located upstream of the Livingstone Fall. The Malebo Pool is surrounded by extensive palms and papyrus swamps along the edges, with floating mats of Eichhornia frequently passing through (*Bailey and Banister*, 1986). The annual amplitude of water level change in the Malebo Pool is about 3 m, and water flows quickly towards the Livingstone Fall with an average flow of 30,000 $m^3 \cdot s^{-1}$ and 60,000 $m^3 \cdot s^{-1}$ in flooding time (*Thieme et al.*, 2005). The biggest island in the Malebo Pool is called the Île Mbamou, which is our study area (Figure 3-1). It separates the Congo River into two channels, and most of the water flows through the channel south of the Île Mbamou to the Livingstone Fall.

Figure 3-1(a) shows 3-arcsecond resolution C-band SRTM DEM over our study region. Interestingly, SRTM DEM values are distinctly different over the southern and northern parts of the Île Mbamou. Since this SRTM DEM is generated with C-band (5.6

cm wavelength) SAR data which cannot fully penetrate vegetation canopy (*Lu and Kwoun*, 2008; *Baugh et al.*, 2013), the measured scattering phase center is usually above bare ground and lower than the tree height (*Brown et al.*, 2010). Consequently, the SRTM elevations are biased upward above the ground into the tree canopy, and do not represent the bare-earth topography. Therefore, it is likely that the higher SRTM DEM values over the southern island partly represent its higher canopy height. This is consistent with the land cover map shown in Figure 3-1(b) from the GLCNMO (Global Land Cover by National Mapping Organizations) 2008 (*Tateishi et al.*, 2010). The southern part of the Île Mbamou is dominated by "broadleaf evergreen forest" while the northern part of the Île Mbamou is occupied by "herbaceous vegetation" and "open canopy". However, old French literature found in (*Sita*, 1968) indicates that the topography between the southern and northern parts of the island may indeed be different.

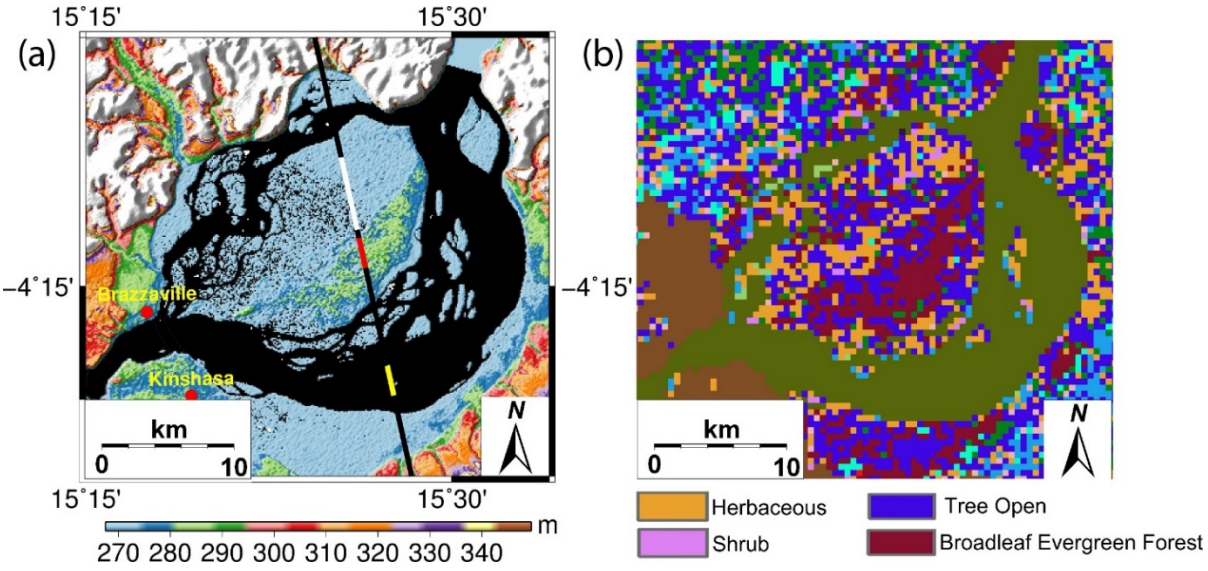

Figure 3-1 (a) Envisat's pass 143 (black line) over our study area. The central island represents the Île Mbamou. Background is the C-band SRTM DEM; (b) Land cover map from GLCNMO2008.

3.3 Dataset

3.3.1 Envisat Radar Altimetry

Envisat RA2 Geophysical Data Record (GDR) of pass 143, from the period of October 2002 (cycle 10) to September 2010 (cycle 93) was used. The ascending pass 143 flies over the Malebo Pool from south to north, sequentially intersecting the southern reach of the Congo River, the Île Mbamou, and northern reach of the Congo River (Figure 3-1(a)). The Envisat RA2 GDR contains 18-Hz (~350 m along-track sampling) retracked range observations using OCEAN, ICE-1, ICE-2, and SEA ICE retrackers. Among these, the ICE-1 retracker (*Wingham et al.*, 1986) was chosen. The instrument corrections, media corrections (dry and wet troposphere corrections from the European Centre for Medium-Range Weather Forecasts model, and the ionosphere correction based on Global Ionosphere Maps), and geophysical corrections (solid Earth and pole tides) were applied. In addition, the 5.6 m level Ultra Stable Oscillator (USO) anomalies for cycles 44–85 were corrected using the European Space Agency's correction table.

3.3.2 PALSAR Backscattering Coefficients

Fourteen ALOS PALSAR images were obtained at ascending flight direction with a look angle of 34.3°, spanning from June 2007 to February 2011, as listed in Table 3-1. Seven of them were obtained with Fine Beam Single (FBS) mode (HH polarization) while the other seven were obtained with Fine Beam Dual (FBD) mode (both HH and HV polarizations) (*Pope et al.*, 1997; *Rosenqvist et al.*, 2007). HH polarization mode images were adopted because it is known to be more sensitive to water level changes beneath vegetation (*Pope et al.*, 1997; *Grings et al.*, 2009) and provides better interferometric

coherence (*Kim et al.*, 2009). PALSAR raw data was processed to obtain Single Look Complex (SLC) images. It is noted that different bandwidths of FBD and FBS data lead to different ground range resolutions, *i.e.*, 28 MHz for FBS data and 14 MHz for FBD data (*Shimada et al.*, 2009). To obtain consistent resolutions, the FBD images were oversampled by a factor 2 in the range direction. The SLC images were then co-registered to a common SLC image obtained on December 13, 2008. To reduce the effects of radar speckle noises, a 4 × 9 multi-look factor was applied to all SLC images. As a result, the spatial resolution of the multi-looked images becomes approximately 30 m × 30 m. The backscattering coefficient (σ_0) can be computed with absolute calibration factors as

$$\sigma_0 = 10 \log_{10}(DN^2) + CF \text{ (dB)}, \tag{3-1}$$

where *DN* is the digital number of the amplitude image, and *CF* is the radiometric calibration factor (−51.9 dB for FBS HH data, and −51.8 dB for FBD HH data) (*Werner et al.*, 2000). A median filter with a 3 × 3 window was also applied to further reduce speckle noises. Since the topography is quite smooth over the study area, gamma naught γ_0 (σ_0 divided by the cosine of the incidence angle) is not considered in this study. Finally, all the σ_0 images were geocoded using a 3-arcsecond SRTM DEM oversampled to 1-arcsecond resolution. However, it is noted that a 1-arcsec SRTM DEM over Africa is now freely available (*JPL*, 2014).

Table 3-1 List of PALSAR scenes used this study.

Scene ID	Operation Mode	Date	Path	Frame	Polarization Mode
ALPSRP073347100	FBD	2007/06/10	607	7100	HV/HH
ALPSRP086767100	FBD	2007/09/10	607	7100	HV/HH
ALPSRP093477100	FBS	2007/10/26	607	7100	HH
ALPSRP100187100	FBS	2007/12/11	607	7100	HH
ALPSRP127027100	FBD	2008/06/12	607	7100	HV/HH
ALPSRP153867100	FBS	2008/12/13	607	7100	HH
ALPSRP180707100	FBD	2009/06/15	607	7100	HV/HH
ALPSRP194127100	FBD	2009/09/15	607	7100	HV/HH
ALPSRP207547100	FBS	2009/12/16	607	7100	HH
ALPSRP214257100	FBS	2010/01/31	607	7100	HH
ALPSRP234387100	FBD	2010/06/18	607	7100	HV/HH
ALPSRP247807100	FBD	2010/09/18	607	7100	HV/HH
ALPSRP261227100	FBS	2010/12/19	607	7100	HH
ALPSRP267937100	FBS	2011/02/03	607	7100	HH

3.3.3 MODIS VCF

The MODIS 250 m VCF collection 5 product was used in this study to represent the spatial heterogeneity of vegetation in the Île Mbamou. The VCF product is derived from all seven bands of MODIS data (*DiMiceli et al.*, 2011; *Hansen et al.*, 2013). It contains proportional estimates for vegetative cover types, including woody vegetation, herbaceous vegetation and bare ground, and thus is useful to show how much of a land

cover such as “forest” or “grassland” exists (*DiMiceli et al.*, 2011). The VCF data is available from 2000–2010, and a mean VCF value was calculated which is shown in Figure 3-2. Figure 3-2 shows clear difference in VCF over the northern (10%–20%) and southern (50%–70%) parts of the island. It indicates that the northern part is mostly covered with non-forest vegetation whereas the southern part is dominated by forest.

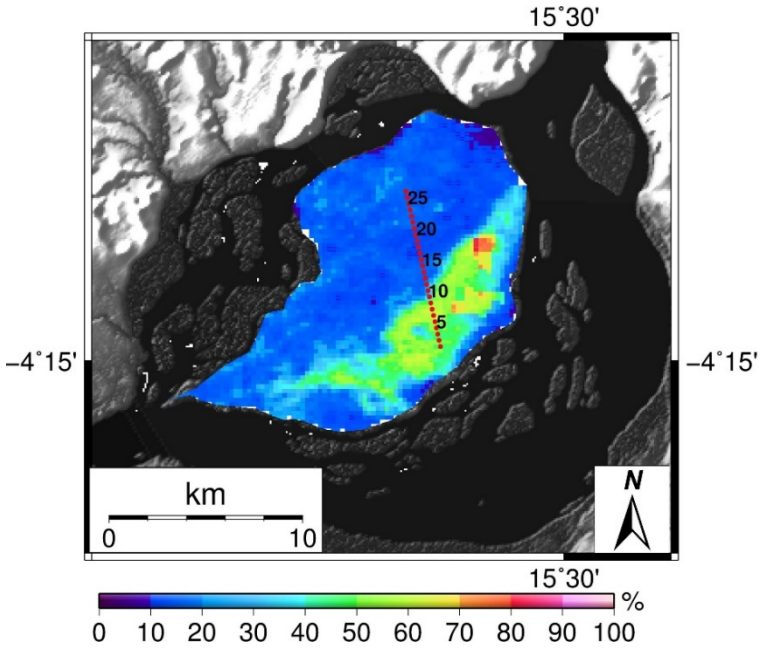

Figure 3-2 Map of MODIS VCF averaged using VCF data from 2000–2010 over the Île Mbamou. Envisat 18-Hz nominal footprints with their numbers are also plotted which are referenced in Section 3.5.2.

Overall, distinctly different vegetation types over the northern and southern parts of the island, along with the intersecting Envisat track make the Île Mbamou an ideal domain to test a regression model toward estimating water level changes based on σ_0 changes and MODIS VCF. Hereinafter, the northern Île Mbamou refers to the non-forested areas and the southern Île Mbamou refers to the forested areas.

3.4 Envisat Altimetry and Interferometric SAR Data Processing

3.4.1 Water Level Changes from Envisat Altimetry

Typically, several high-rate (e.g., 18-Hz in case of Envisat altimetry) measurements obtained over intersections of the satellite track and water bodies (river, lake, reservoir, wetlands) are spatially averaged to generate time series of water level. Figure 3-3 illustrates the surface height profiles along Envisat pass 143 obtained from several Envisat cycles over the Malebo Pool. Water levels fluctuations are observed over the southern Congo reach, and southern and northern parts of the Île Mbamou (marked with "1", "2", and "3", respectively, in Figure 3-3). Water level change time series were the generated by combining successive overpasses. Figure 3-4(a) shows the time series of water level change over the southern reach of the Congo River ("1" in Figure 3-3) using Envisat altimetry measurements (blue line) and daily *in situ* gauge observations at Brazzaville (red). The black dots in Figure 3-4(a) indicate the daily *in situ* data temporally closest to the Envisat altimetry data, which are used to compute the RMSE and correlation coefficient. After editing out spurious data, it shows overall good agreement between Envisat altimetry and *in situ* gauge data with a root-mean-square error (RMSE) of 34.9 cm and correlation coefficient of 0.95. Part of the RMSE would be due to the fact that Brazzaville is located where the northern and southern Congo River meet, which resulted in a higher amplitude for the *in situ* time series. Similarly, we generated water level time series by spatially averaging several 18-Hz Envisat altimetry measurements over the southern and northern parts of the Île Mbamou ("2" and "3" in Figure 3-3, respectively), which both revealed 2–3 m of distinct seasonal variations (Figure 3-4(b)). Error bars in Figure 3-4(b) represent

95% confidence intervals. Interestingly, from Figure 3-4(b), it suggests that the water over the forested area stays for a longer period of time than the water over the non-forested area (roughly 3 or 4 months), which may indicate that the forested land has a longer residence time.

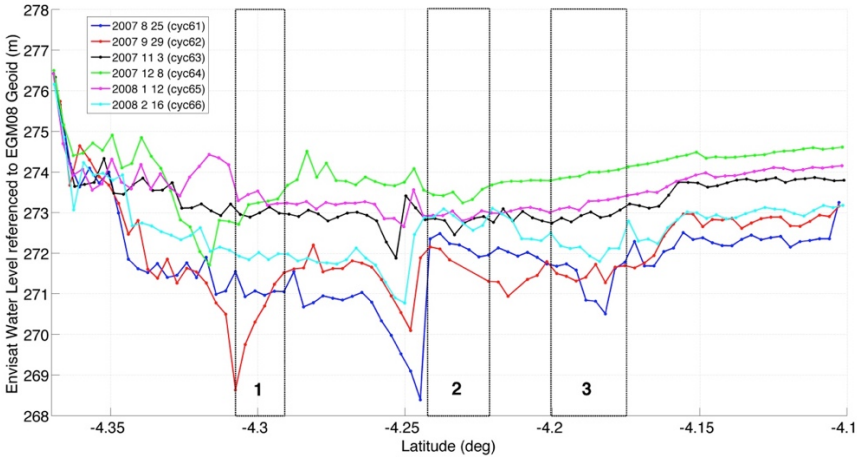

Figure 3-3 Water level fluctuations referenced to EGM08 geoid over the Île Mbamou along Envisat pass 143. The "1", "2", and "3" correspond to regions with yellow, red, and white colors along the Envisat pass in Figure 3-1.

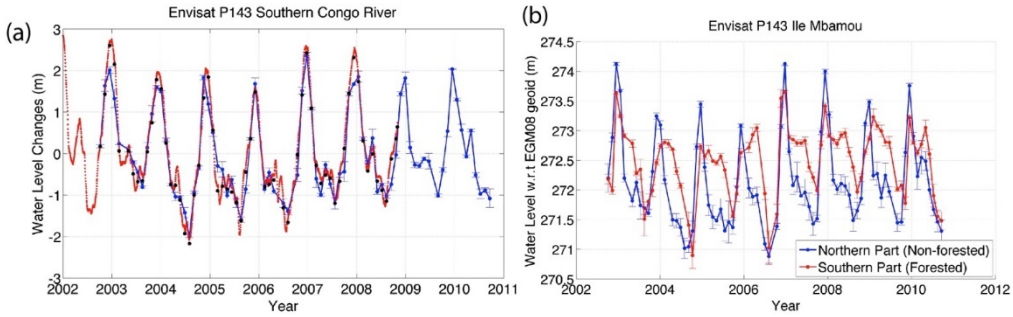

Figure 3-4 (a) Time series of water level changes from Envisat altimetry over region "1" and from the *in situ* gauge at Brazzaville (red). (b) Time series of water level changes from Envisat altimetry over region "2" and region "3".

3.4.2 Comparison of Water Level Changes from Envisat Altimetry over the Everglades and *in Situ* Data

In order to demonstrate Envisat altimeter's capability for measuring water level changes over these vegetated wetlands in the Île Mbamou where no *in situ* record exists,

an indirect verification was performed by comparing the Envisat altimetry derived water level changes and *in situ* records over the Everglades wetlands in Florida, USA. Figure 3-5 shows Envisat ground tracks over the Everglades with its VCF as background. We generated six water level change time series using the 18-Hz ICE-1 retracked measurements from passes 194 and 465, and compared them with nearby gauge data. As summarized in Table 3-2, VCF values extracted over the Envisat stations indicate that stations EnvP194_1, EnvP194_2, EnvP194_3, EnvP194_4, and EnvP465 are covered with non-forested vegetation and station EnvP194_5 is covered with forested vegetation. In Figure 3-6, the blue lines represent time series of water level changes from Envisat altimetry and red dots represent nearby *in situ* gauges. The black dots in Figure 3-6 indicate the *in situ* data temporally closest to the Envisat altimetry data, which are used to compute RMSE and correlation coefficient. Figure 3-6 and Table 3-2 show that all the Envisat altimetry time series agree very well with *in situ* data regardless of the canopy density. The unstable performance of Envisat altimetry over EnvP194_3 in 2007 and 2009 is suspected to be due to the dry conditions of the surface that persisted for about three months as can be seen from *in situ* data. After all, although the forest types in the Everglades and the southern Île Mbamou may be different, this comparison study over the Everglades shows that Envisat altimetry can measure water level changes beneath both non-forested and forested land cover accurately.

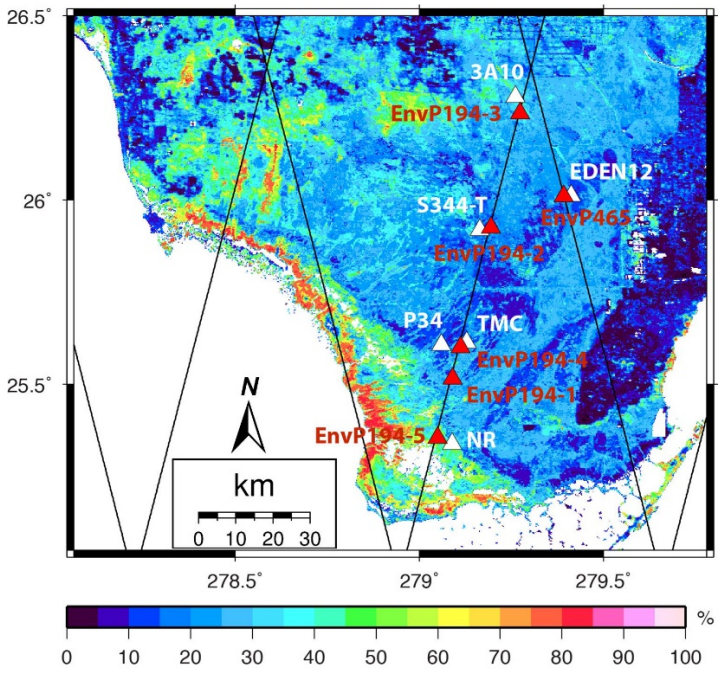

Figure 3-5 VCF Map of the Everglades with Envisat ground tracks. The Envisat stations and adjacent *in situ* gauges are indicated with red and white triangles, respectively.

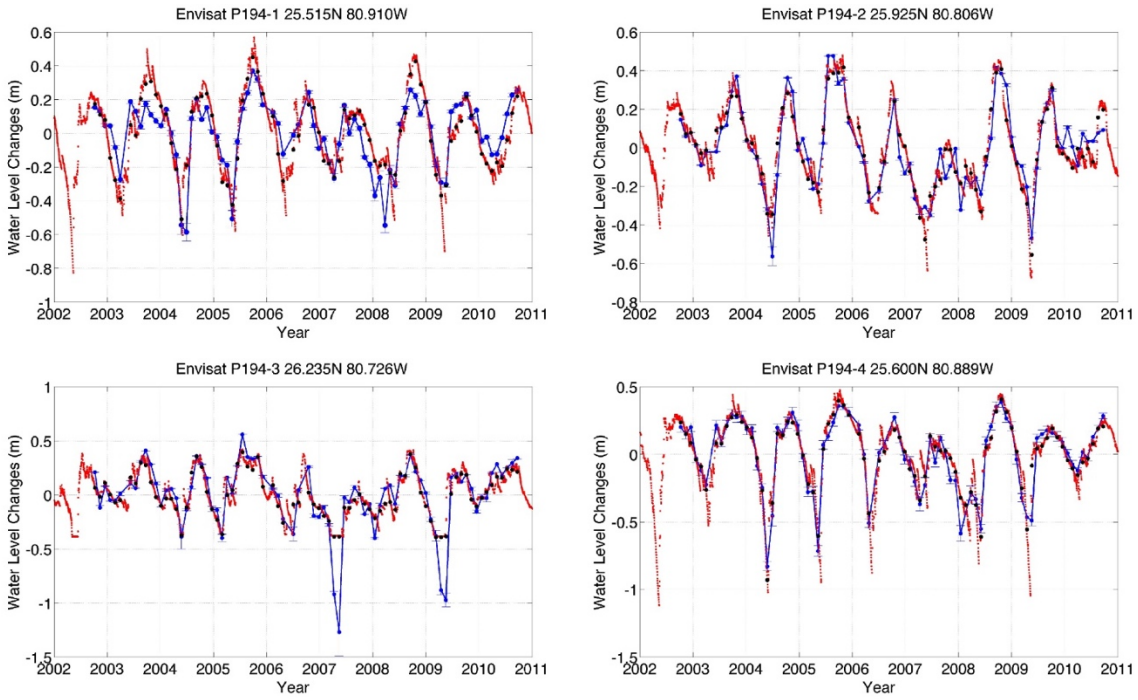

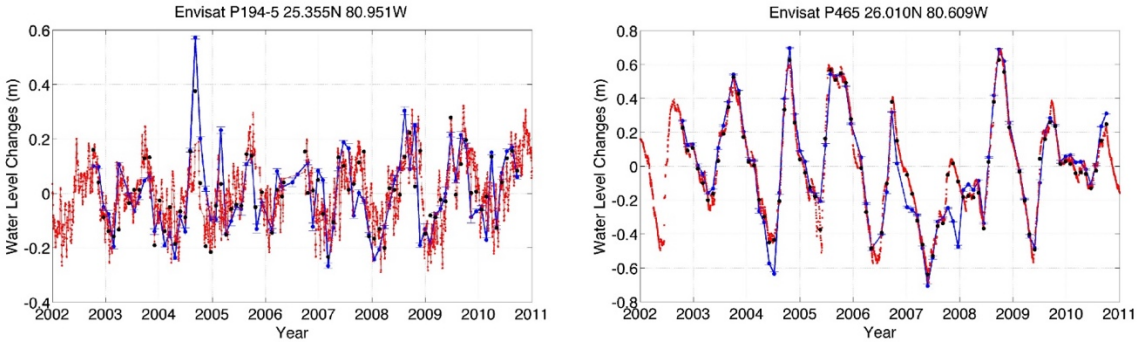

Figure 3-6 Time series of water level changes from Envisat altimetry (blue) and nearby *in situ* gauges (red). The black dots indicate the *in situ* data temporally closest to the Envisat altimetry data.

Table 3-2 Comparison between water level changes obtained from Envisat altimetry and *in situ* data over the Everglades wetlands

Altimetry Time Series	*In Situ* Gauges	Distances between the Altimetry Station and Gauge (km)	RMSE (cm)	Correlation Coefficient	VCF (%)
EnvP194-1	P34	10.7	12.2	0.83	25
EnvP194-2	S344-T	3.2	8.6	0.92	19
EnvP194-3	3A10	5.1	17.1	0.87	27
EnvP194-4	TMC	2.3	8.0	0.97	29
EnvP194-5	NR	4.4	9.8	0.75	48
EnvP465	EDEN12	2.1	8.6	0.96	21

3.4.3 Water Level Changes over Each Envisat's High-rate Nominal Footprint

Next, we generated water level change time series over each of Envisat's 18-Hz nominal ground track location using the high-rate *stackfile* method (for details, refer to (*Lee et al.*, 2008, 2009)). Each Envisat high-rate (18-Hz) *stackfile* bin serves as the 18-Hz nominal ground track to which the 18-Hz water level change time series are referred. For each GDR record from a given Envisat cycle and pass, the corresponding row is predicted

based on an equator crossing table which is computed by interpolating the precision orbit ephemeris (POE) of Envisat. In other words, for example, for an ascending pass, the row can be computed such as (*Kruizinga*, 1997):

$$row_{asc} = \frac{T_{asc} - T_{eqAsc}}{\Delta T}, \tag{3-2}$$

where T_{asc} is the time tag on the ascending pass of a surface height measurement, T_{eqAsc} is the time tag when the ascending pass crosses the equator and ΔT is the time spacing of the surface height measurements. The equator crossing tables are the basis of mapping transformation between time tags in GDR record and row-column addresses of the low-rate (1-Hz) *stackfile* bins (for details, refer to Chapter 2 of (*Kruizinga*, 1997)). If the predicted 1-Hz *stackfile* row-column address is equivalent to the given bin address of the empty *stackfile* array, then for each 1-Hz stackfile bin, 18-Hz *stackfile* bins (or 18-Hz nominal ground tracks), in which the water levels are "stacked", are created. The latitudes and longitudes of the 18-Hz bins (or ground tracks) are calculated by linearly interpolating two adjacent 1-Hz nominal ground track latitudes and longitudes, which are stored in the 1-Hz *stackfile* bin header. The 18-Hz nominal ground tracks over the Île Mbamou are plotted in Figure 3-1(a).

3.4.4 Water Level Changes from InSAR

To be compared with the water level changes from altimetry, two differential interferograms using PALSAR pairs obtained on October 26 2007–November 11 2007 (water increasing period) and December 16 2009–January 31 2010 (water decreasing period) were generated, and their spatial gradient of the water level changes between the acquisition dates (results in Section 3.5.3) were obtained. Perpendicular and temporal

baselines of the interferograms are summarized in Table 3-3. After flat-earth phase removal, the interferometric phase mainly contains contributions from the topographic relief and surface deformation in the radar range direction. The differential interferogram, which presumably contains phase changes only due to wetland water level changes (*Alsdorf et al.*, 2001; *Lu and Kwoun*, 2008; *Kim et al.*, 2009), were generated after removing the topographic phases using the SRTM DEM. Because inaccurate orbit vector information provided in the PALSAR metadata often leaves residual fringes in the interferograms, the baseline error was modeled using the best-fitting polynomial to remove the artifacts due to the orbital error. The differential interferograms were then smoothed using adaptive filtering to enhance the fringe visibility, and finally geocoded to yield the displacement maps using the look-up table generated from existing geocoded SRTM DEM and SAR image orbital information (*Wegmuller*, 1999). Considering the radar wavelength and incidence angle of the PALSAR images, 1.0 radian of interferometric phase is equivalent to 2.4 cm of vertical water level change (*Jung et al.*, 2010).

Table 3-3 Description of InSAR pairs used to generate interferograms.

Attribute	Water Increasing Season	Water Decreasing Season
Perpendicular Baseline	116 m	79 m
Ambiguity Height	439 m	645 m
Date	October 26 2007	December 16 2009
	December 11 2007	January 31 2010

3.5 Estimating Wetland Water Level Changes Based on σ_0 Changes

3.5.1 Temporal Variation of σ_0

Figure 3-7 shows the geocoded PALSAR σ_0 images over the study region. It is clear to see the temporal variations in the backscattered intensity, but with distinctly different patterns over the northern and southern parts of the Île Mbamou. For example, in June (June 10, 2007 or June 12, 2008) which corresponds to the low-water season, the entire island reveals similar intensity while in December (December 11, 2007, December 13, 2008, or December 16, 2009), the high-water season, the southern part appears much brighter than the northern part. This can be explained if the northern part of the island has mainly non-forested low canopy vegetation whereas the vegetation on the southern part is mainly highly dense forest as indicated by the VCF map in Figure 3-2. During the high-water season, the northern Île Mbamou (non-forested) would be mostly submerged and little radar energy would be backscattered to the satellite due to specular scattering. On the other hand, over the southern Île Mbamou (forested), increasing water level would lead to stronger double-bounce backscattering.

As shown in Figure 3-8, the σ_0 over the northen and southern Île Mbamou (over the black boxes in the averaged σ_0 map in Figure 3-7) show seasonal variations which are expected to be related to the water level changes. Mostly, the peaks and troughs of the non-forested land σ_0 variation correspond to the troughs of peaks of the forested land σ_0 variation, respectively. In the case of the forested land, increasing water level leads to stronger radar return due to enhanced double-bounce backscattering. On the contrary, the radar backscattering over the non-forested land is governed by the specular scattering during high-water season, leading to weaker radar return. However, stronger radar return is observed during the low-water season due to the double-bounce backscattering (*Lu and Kwoun*, 2008; *Kim et al.*, 2014) or multipath backscattering (*Kasischke et al.*, 2003) in non-

forested vegetation. From Figure 3-8, it also shows that σ_0 over the non-forested northern Île Mbamou reveals stronger temporal variations than those over the forested southern Île Mbamou.

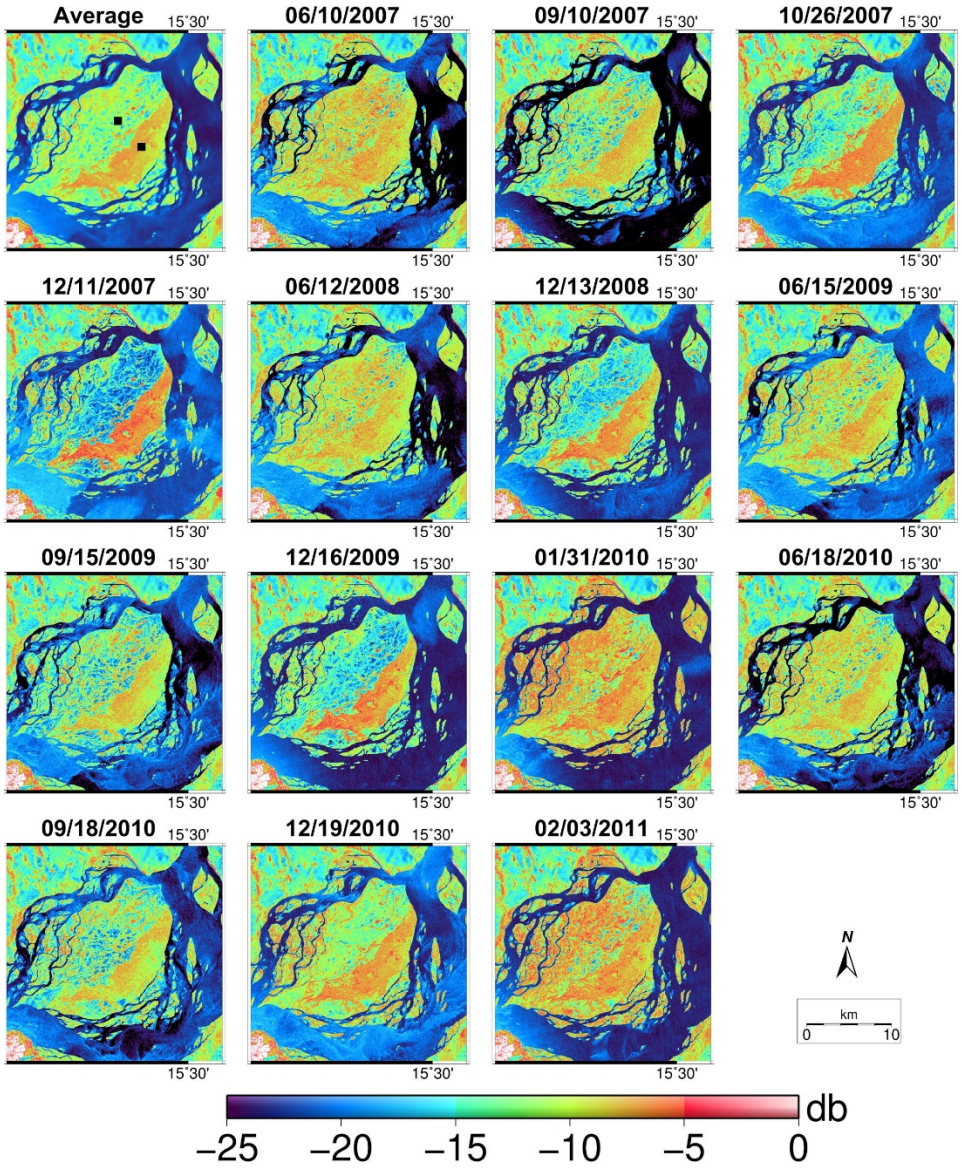

Figure 3-7 Images of PALSAR σ_0 used in this study. PALSAR σ_0 values over the northern part of the island, and the southern part of the island marked with black boxes in the "Average" image are used for Figure 3-8.

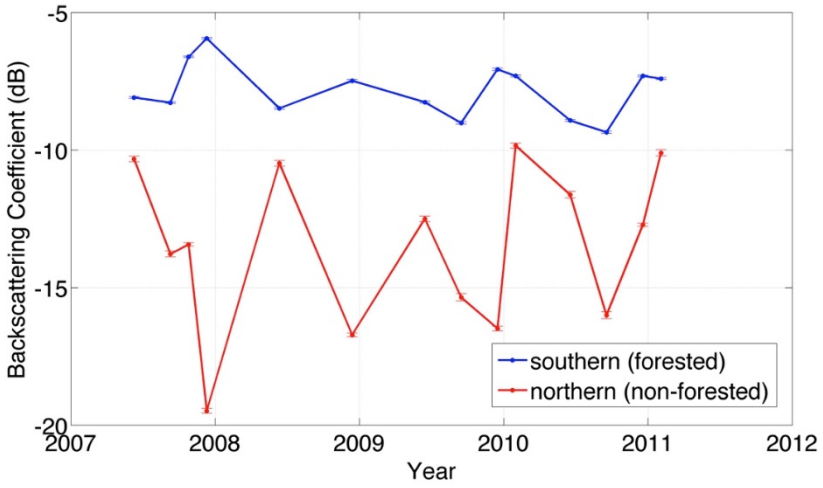

Figure 3-8 Variations of PALSAR σ_0 over the northern and southern parts of the island, averaged over the 31 × 31 black boxes shown in Figure 3-7. Error bars represent 95% confidence intervals.

It is noted that another important driver of temporal variation in L-band σ_0 over non-forested vegetation is variation in soil moisture (*Kasischke et al.*, 2003). It is expected that σ_0 would increase if the surface soil condition transits from dry to wet. Although the northern Île Mbamou may experience a seasonal dry condition, it is expected that the σ_0 variation observed in Figure 3-7 and Figure 3-8 is not likely due to the soil moisture variation based on Figure 3-9 which compares the time series of Envisat water level changes and PASLAR σ_0 changes over the northern Île Mbamou. As shown in Figure 3-9, PALSAR σ_0 increases when the water level decreases. In other words, the increase in PALSAR σ_0 does not occur during the dry or early wet period, but during the decreasing water period due to the enhanced double-bounce (or multipath) backscattering. Therefore, the PALSAR σ_0 data used in this study (listed in Table 3-1) do not show variation due to soil moisture increase, at least over the Envisat altimetry footprint locations.

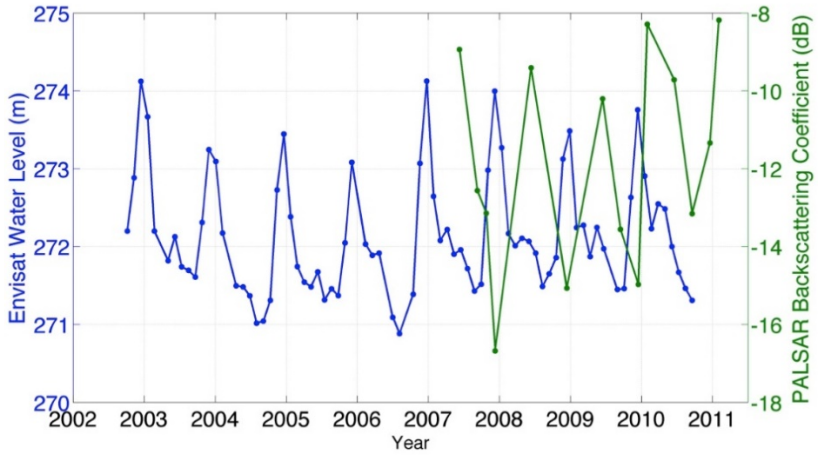

Figure 3-9 Time series of water levels from Envisat altimetry (blue, left-axis) and backscattering coefficient from PALSAR (green, right-axis) over the non-forested northern Île Mbamou.

3.5.2 Effects of Water Level Changes on PALSAR σ_0

3.5.2.1 Relationship between Envisat Water Level Changes and PALSAR σ_0 Changes

Here, linear regression analysis between water level changes from Envisat altimetry and PALSAR σ_0 changes over each Envisat's 18-Hz nominal ground track (or footprint) location was performed. The σ_0 changes over the ground track locations were obtained by performing a bilinear spatial interpolation. The water level changes generated over each of the 18-Hz *stackfile* bins are linearly interpolated to each PALSAR acquisition dates using two consecutive Envisat altimetry measurements obtained before and after the PALSAR acquisition dates, and compared with the corresponding PALSAR σ_0 changes. For each Envisat's 18-Hz nominal footprint, the lowest water level was used as a reference and regression analysis between the changes of water levels and σ_0 was performed as shown in Figure 3-10 and Figure 3-11.

Figure 3-10 shows selected time series of water level changes from Envisat altimetry (blue in the upper panels) and σ_0 (green in the upper panels) over the forested

land. Results of linear regressions between them are illustrated in the bottom panels (Figure 3-10). The amplitude difference of the water level changes between adjacent 18-Hz nominal footprint is partially due to altimeter measurement error. Figure 3-10 shows positive correlation between the changes of water levels and σ_0, which indicates that increasing water levels lead to stronger σ_0 over the forested lands. The stronger σ_0 can be explained by the enhanced double-bounce backscattering due to the increasing water levels.

Figure 3-11 shows selected time series of water level changes from Envisat altimetry (blue in the upper panels) and σ_0 (green in the upper panels) over the non-forested land. Results of linear regressions between them are illustrated in the bottom panels (Figure 3-11). The blue and black lines represent the fitted line for "water increase I", and "water increase II", respectively (Figure 3-11 bottom panels). Figure 3-11 also shows the positive correlation between the changes of water levels and σ_0 over the non-forested lands until the water surface reaches a certain level. This can also be explained by the stronger double-bounce backscattering. If the water level continues to increase, then the negative correlation between the changes of water levels and σ_0 is observed over the non-forested lands, which can be explained by the enhanced specular backscattering. A schematic plot illustrating these different backscattering mechanisms is shown in Figure 3-12 (modified from Figure 3 in (*Kim et al.*, 2014)). The VCF threshold used to distinguish between the forested and non-forested lands will be discussed in the following section.

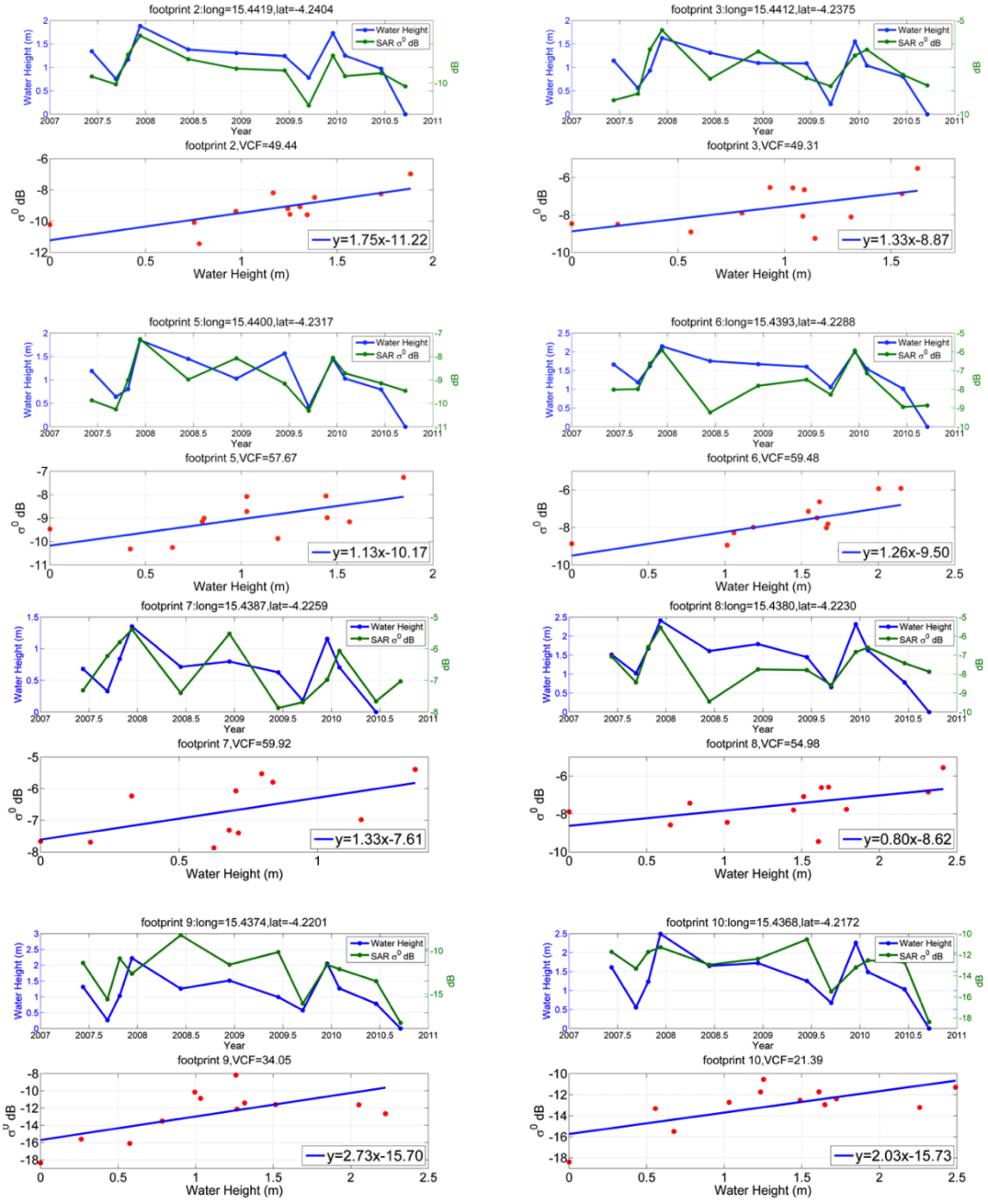

Figure 3-10 Selected time series of water level changes from Envisat altimetry and σ_0 over the forested land. Results of linear regressions between them are illustrated in the bottom panels. Refer to Figure 3-2 for the location of the footprints.

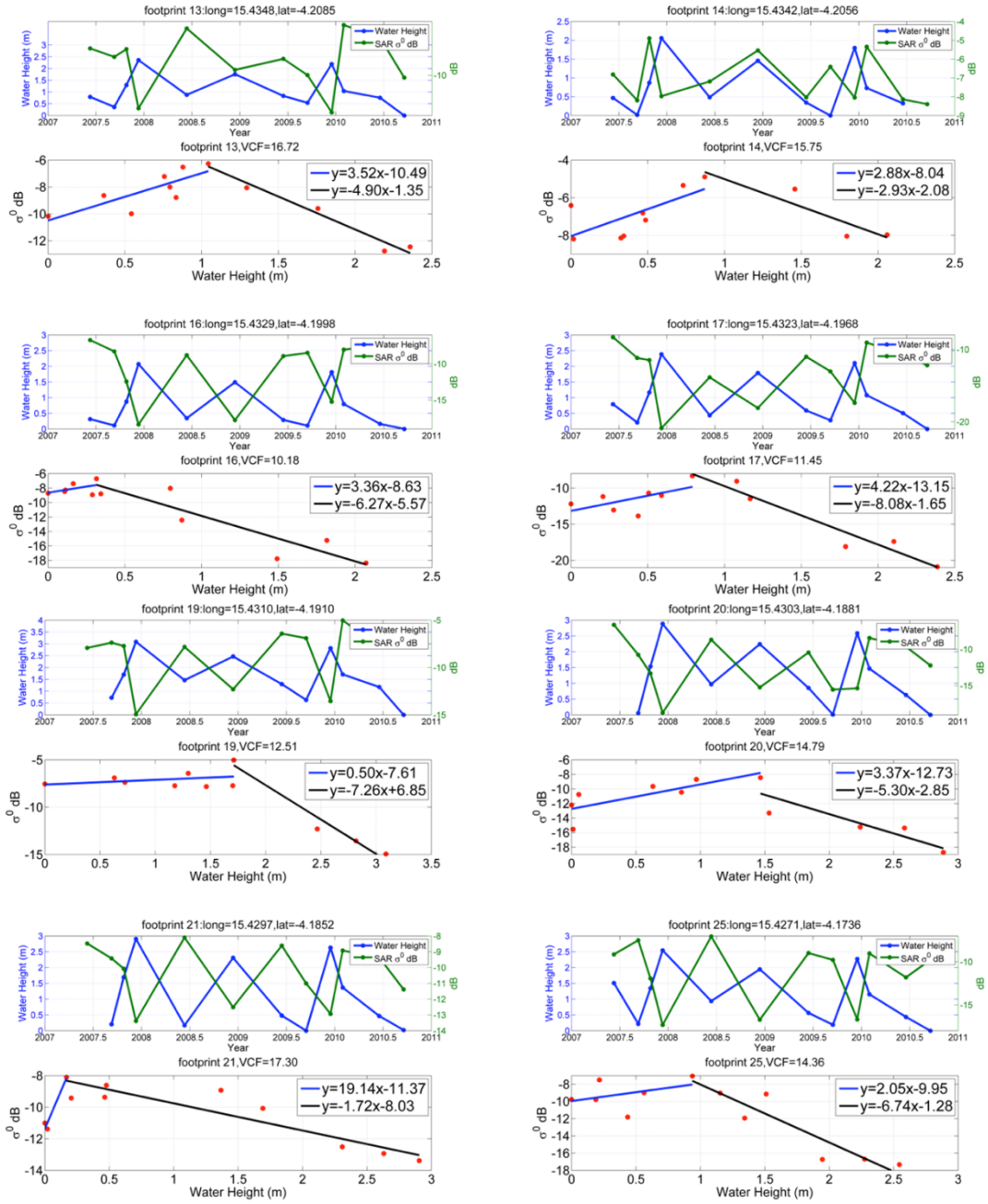

Figure 3-11 Selected time series of water level changes from Envisat altimetry and σ_0 over the non-forested land. Refer to Figure 3-2 for the location of the footprints.

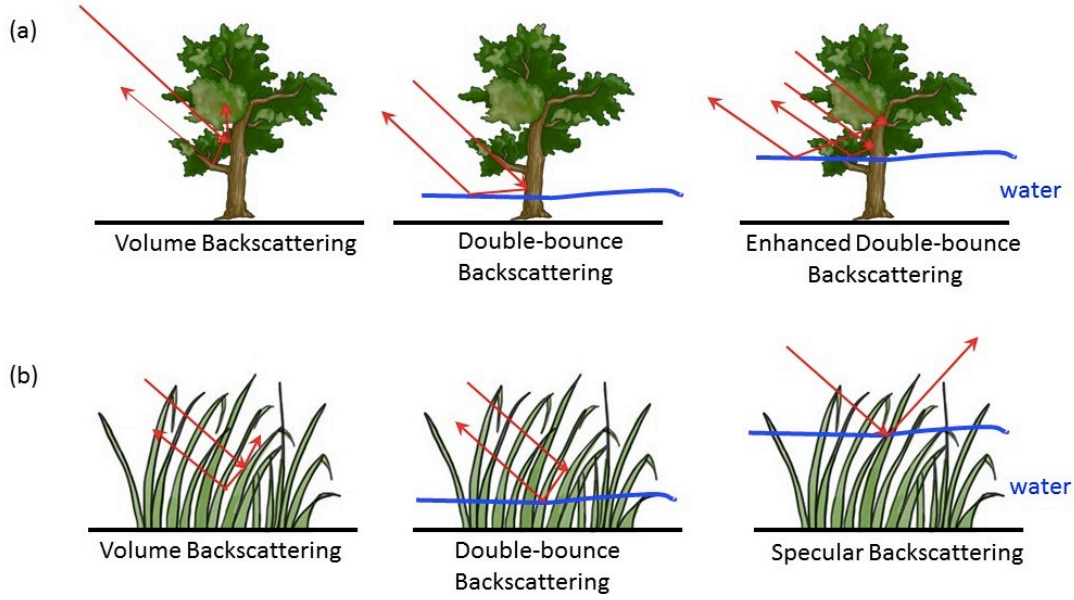

Figure 3-12 Different backscattering mechanisms over the (a) forested and (b) non-forested lands with different levels of water.

3.5.2.2 Distinguishing Forested and Non-Forested Lands

In Figure 3-10 and Figure 3-11, the mean VCF was used as a representative vegetation density value at each of Envisat's 18-Hz nominal footprint location, so the relation between the linear regression slopes and VCF can be investigated (see Section 3.5.2.3). It is noted that the spatial resolution of VCF (250 m) is finer than the altimeter along-track footprint interval (~350 m). First of all, a threshold should be determined to classify the forested and non-forested lands using VCF which is the percentage tree cover for every pixel. Various studies have used different VCF tree cover thresholds to determine forest land areas. For example, *Nelson et al.* (2004) used a threshold of 25% and produced estimates of forested land area similar to inventory estimates for the entire United States (US) and for the conterminous US. *Schmitt et al.* (2009) used 10% tree cover threshold and estimated global forest cover to be 39 million km^2. Over the entire Congo Basin, *Hansen et al.* (2008) used VCF Landsat training data and four years of MODIS inputs to classify

"non-treed" cover with a threshold of <10%. In this study, the threshold to distinguish between the forested and non-forested lands was based on the regression relationships between σ_0 and water level changes over each of the Envisat 18-Hz nominal footprints.

Figure 3-10 shows the time series of PALSAR σ_0 and interpolated Envisat altimetry water level changes over, for example, some of the footprint locations (footprints 2, 3, 5, 6, 7, 8, 9 and 10) which have VCF > 20%. There exists positive correlation between σ_0 and Envisat altimetry water level changes over these locations. In other words, higher water level leads to higher σ_0. This indicates that higher water level can lead to enhanced double-bounce backscattering over wetlands with VCF > 20%. The results of linear regressions are summarized in Table 3-4. Except for footprint 4, all of the locations with VCF > 20% have positive regression slopes. On the other hand, Figure 3-11, for example, shows the time series of σ_0 and interpolated Envisat altimetry water level changes over some of the footprint locations (footprints 13,14, 16, 17, 19, 20, 21 and 25) which have VCF < 20%. Interestingly, both positive and negative correlations were found to exist between σ_0 and water level changes. As water level increases up to ~1 m, σ_0 also increases as in the case of wetlands with VCF > 20%. However, when the water level increases more than ~1 m, σ_0 then starts to decrease. This can be explained if the double-bounce backscattering is enhanced with increasing water level only until a certain stage, and then specular backscattering becomes dominant with higher water levels over non-forested land. This finding is different from previous studies of (*Kasischke et al.*, 2003; *Kim et al.*, 2014) which employed only one regression model with a negative slope. Accordingly, two linear regression models were fitted: one with a positive slope and the other with a negative slope as shown in the bottom panels of Figure 3-11. The water level change which leads to the

highest σ_0 is used to split the water level change and σ_0 variables, so the two regression models can be applied separately. The regression results for all the footprint locations with VCF < 20% are summarized in Table 3-5. Based on these observed different sensitivities of σ_0, the VCF threshold of 20% will be used in the following sections to distinguish the forested and non-forested land covers

Table 3-4 Linear regression results over the southern forested Île Mbamou. Locations of Envisat 18-Hz nominal footprints are illustrated in Figure 3-2.

Envisat Footprint	Latitude (Degree)	Longitude (Degree)	VCF (%)	Slope	Intercept	R^2
1	15.4425	−4.2434	48.9	1.33	−9.29	0.15
2	15.4419	−4.2404	49.4	1.75	−11.2	0.56
3	15.4412	−4.2375	49.3	1.33	−8.86	0.32
4	15.4406	−4.2346	51.2	−0.23	−7.83	0.01
5	15.44	−4.2317	57.6	1.12	−10.17	0.41
6	15.4393	−4.2288	59.4	1.25	−9.49	0.41
7	15.4387	−4.2259	59.9	1.32	−7.6	0.31
8	15.438	−4.223	54.9	0.8	−8.62	0.27
9	15.4374	−4.2201	34.0	2.72	−15.69	0.4
10	15.4368	−4.2172	21.3	2.03	−15.73	0.46

Table 3-5 Linear regression results over the northern non-forested Île Mbamou. Locations of Envisat 18-Hz nominal footprints are illustrated in Figure 3-2.

Envisat Footprint	Latitude (Degree)	Longitude (Degree)	VCF (%)	Slope 1	Intercept 1	R^2	Slope 2	Intercept 2	R^2
11	15.4361	−4.2143	19.0	2.97	−16.71	0.74	−10.48	6.25	0.95
12	15.4355	−4.2114	15.4	8.58	−23.68	0.66	−9.83	2.36	0.82
13	15.4348	−4.2085	16.7	3.51	−10.49	0.64	−4.90	−1.35	0.96
14	15.4342	−4.2056	15.7	2.87	−8.041	0.48	−2.93	−2.07	0.84
15	15.4335	−4.2027	13.7	0.50	−8.48	0.02	−7.84	0.73	0.95
16	15.4329	−4.1998	10.1	3.35	−8.67	0.22	−6.27	−5.56	0.84
17	15.4323	−4.1968	11.4	4.21	−13.15	0.37	−8.08	−1.64	0.94
18	15.4316	−4.1939	12.6	1.25	−8.95	0.44	−3.95	−6.69	0.66
19	15.431	−4.191	12.5	0.49	−7.60	0.10	−7.26	6.84	0.96
20	15.4303	−4.1881	14.7	3.36	−12.73	0.61	−5.29	−2.85	0.78
21	15.4297	−4.1852	17.2	19.14	−11.36	0.95	−1.72	−8.02	0.85
22	15.4291	−4.1823	15.6	2.33	−12.20	0.23	−6.34	−0.04	0.73
23	15.4284	−4.1794	17.4	2.79	−10.91	0.81	−3.41	−4.20	0.50
24	15.4278	−4.1765	15.8	−2.13	−7.28	0.22	−17.06	29.91	0.99
25	15.4271	−4.1736	14.3	2.04	−9.94	0.16	−6.74	−1.27	0.86
26	15.4265	−4.1707	16.1	1.98	−9.70	0.34	−5.22	−4.63	0.60

3.5.2.3 Relationship between the σ_0 Sensitivity and VCF

Different regression slopes (dB/m) summarized in Table 3-4 and Table 3-5 over each of the footprints indicate varying sensitivities of σ_0 to water level changes over the forested and non-forested lands. For example, a steeper regression slope indicates higher σ_0 sensitivity to water level changes. Here, the relationship of the σ_0 sensitivity and VCF over the forested and non-forested lands was examined separately. Figure 3-13 shows the relationship between the regression slopes and VCF values over each of the footprints in forest (VCF > 20%). It shows that the regression slope (or σ_0 sensitivity) generally decreases with higher VCF (between 20% and 60%) (Figure 3-13). This can be explained if denser canopy leads to higher volume scattering from the canopy and less double-bounce backscattering with less radar energy that penetrates through denser canopy. In other words, although the same amount of water level increase occurs, a smaller amount of σ_0 increase is obtained if the area is covered with denser canopy.

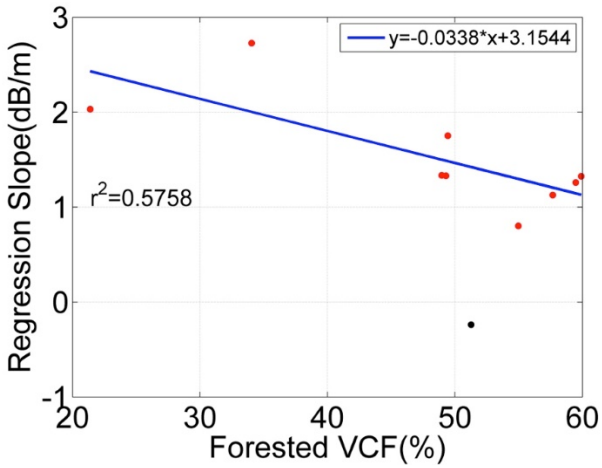

Figure 3-13 Regression analysis between the regression slope (dB/m) from Table 3-4 and VCF over the forested land. Black dot is treated as an outlier and excluded from the regression analysis.

On the other hand, in the non-forested land, as mentioned above, σ_0 first increases, then decreases as the water level increases. Here, the σ_0 response to water level changes was separated with respect to the water level increase which yields the highest σ_0. The saturation point of σ_0, which is described in (*Le Toan et al.*, 1997; *Costa et al.*, 2002) is generally determined by above-water biomass and above-water canopy height. Figure 3-14 shows the relationship between the water increase yielding the highest σ_0 (or "saturation height") and the corresponding VCF value in the non-forested land (between 10% and 20%). Generally, it shows that higher VCF results in a higher saturation height (Figure 3-14). In fact, this positive correlation is consistent with the conclusion drawn from (*Le Toan et al.*, 1997; *Costa et al.*, 2002) which used above-water biomass and above-water canopy height. The positive correlation indicates that higher VCF areas would need higher water levels to reach the saturation biomass and hence higher saturation height.

Next, to examine the σ_0 sensitivity in the non-forested land, the total span of water level increases was divided into two parts: "water increase I" ($0 < h <$ saturation height) and "water increase II" (saturation height $< h < h_{max}$), and then a linear regression was performed between the σ_0 sensitivity and VCF as done in the forest (Figure 3-13). Figure 3-15(a) shows regression analysis between the regression slope1 (dB/m) from Table 3-5 and VCF over the non-forested land for "water increase I". No obvious relationship can be observed in Figure 3-15(a). This indicates that the density of the non-forested vegetation does not influence on σ_0 sensitivity (or the double-bounce backscattering for "water increase I"). Figure 3-15(b) shows regression analysis between the regression slope2 (dB/m) from Table 3-5 and VCF over the non-forested land for "water increase II". Black dots in Figure 3-15 are treated as outliers and excluded from the regression analysis. A positive

correlation between σ_0 sensitivity and VCF can be found, indicating that lower non-forested vegetation density leads to steeper regression (negative) slope. In other words, the specular scattering which leads to a diminished radar return to the satellite is enhanced with less dense non-forested canopy. It should be noted that the regression slopes are all negative for "water increase II" when water level increase exceeds the saturation height because specular scattering becomes dominant as the canopy becomes submerged, and there is little chance for the radar signal to interact between canopy stems and the water surface (*Kwoun and Lu*, 2009).

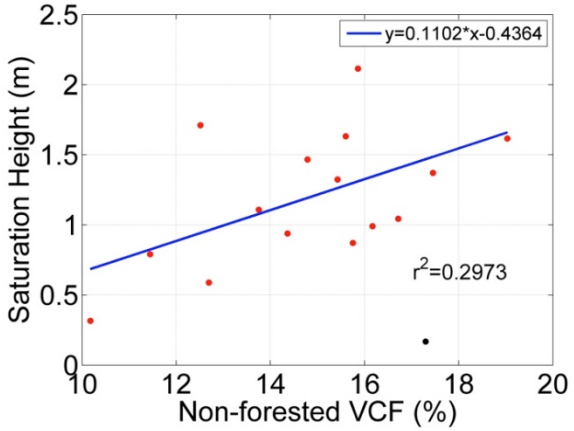

Figure 3-14 Relation between saturation height and VCF in the non-forested land. The black dots are treated as outliers and excluded from the regression analysis.

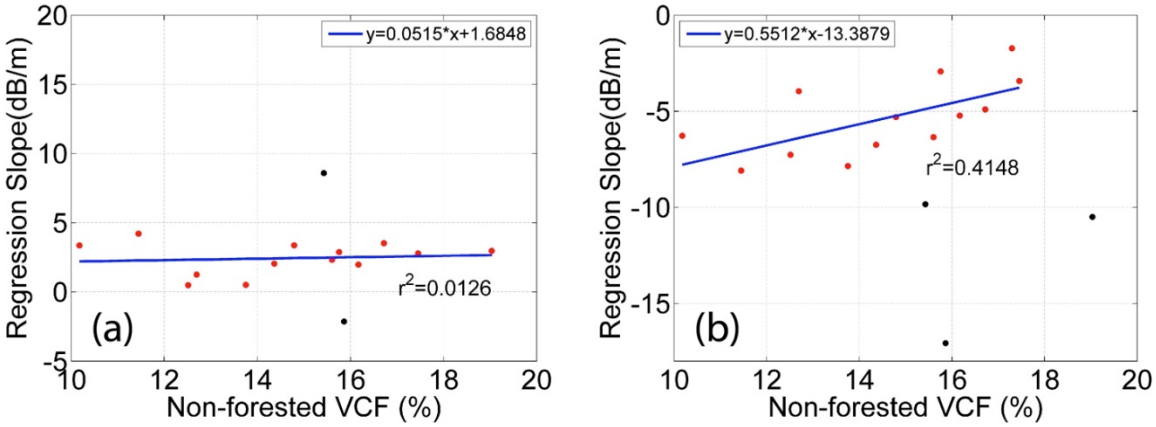

Figure 3-15 (a) Regression between the slope1 (dB/m) in Table 3-5 and VCF over the non-forested land for "water increase I"; (b) Regression between the slope2 (dB/m) in Table 3-5 and VCF over the non-forested land for "water increase II".

It is noted that the outliers excluded from the regression analyses in Figure 3-13-Figure 3-15 may be caused by altimeter measurement errors or by the coarse spatial resolution of the VCF product.

3.5.3 Water Level Changes Estimated from σ_0 Changes and VCF

In this section, based on the σ_0 sensitivities characterized over the Île Mbamou, water level changes are estimated between two pairs of SAR acquisition dates: one for the water increasing period (October 26 2007–December 11 2007) and the other for the water decreasing period (December 16 2009–January 31 2010), which are the same SAR pairs used to generate the two differential interferograms described in Section 3.4.4. First, 14 Envisat footprint locations were arbitrarily selected among the 26 footprint locations: five over the forested, and nine over the non-forested lands (green circles in Figure 3-18) for the purpose of performing the regression analysis as shown in Figure 3-16 on the σ_0 sensitivity (or the regression slope of dB/m) and VCF over forested and non-forested lands, separately, similar to the analysis done in Figure 3-13 and Figure 3-15, respectively. The rest of the footprints will be used to perform comparison with the Envisat altimetry water level changes for validation purpose. Next, using the regression result (dB/m *versus* VCF) from Figure 3-16, water level changes were computed over the 18-Hz Envisat footprints which were *not* used for the regression analysis (purple diamonds in Figure 3-18) such as:

$$\Delta h = \frac{\Delta\sigma_0}{(Regression\ Slope)\cdot VCF}\ (m), \tag{3-3}$$

where $\Delta\sigma_0$ (dB) is the σ_0 changes between the two dates, and the regression slope has a unit of dB/m/VCF(%) determined from Figure 3-16.

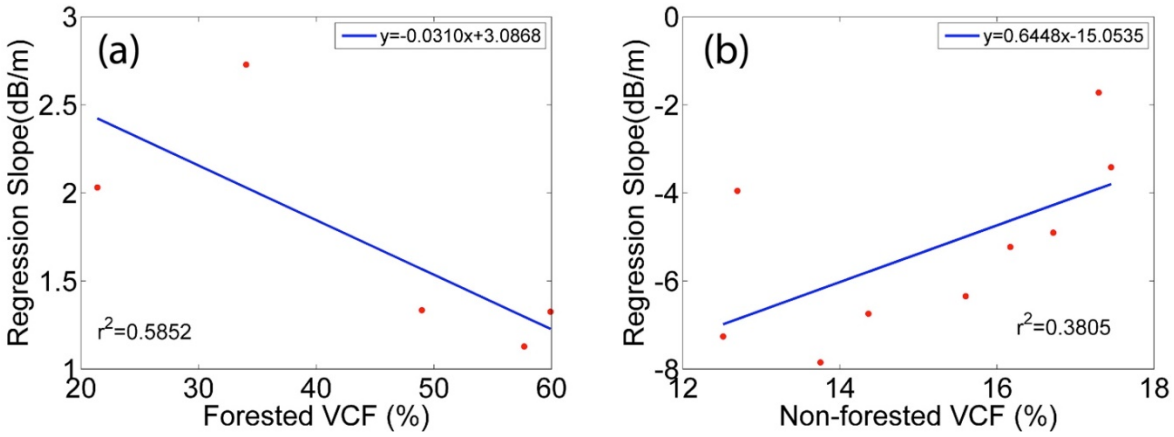

Figure 3-16 Regression analysis between the regression slopes (dB/m) and VCF using five Envisat footprints over the forested land and nine Envisat footprints over the non-forested land.

Before comparing the estimated Δh from Equation (3-3) with Δh obtained from Envisat altimetry water levels, Δh from InSAR which has a centrimetric accuracy (*Alsdorf et al.*, 2007b) and Δh from Envisat altimetry was first compared in order to further validate the altimetry results. Figure 3-17 shows the two wrapped differential interferograms generated over the forested area. Due to low coherences, the fringes over the non-forested area have been masked out, and validation of altimetry measurements can be performed over the forested southern Île Mbamou only. The interferogram shown in Figure 3-17(a) reveals a spatial variation in water level change between October 26 2007 and December 11 2007 whereas the interferogram in Figure 3-17(b) shows negligible spatial variation in water level change between December 16 2009 and January 31 2010. The differential interferometric phases along the Envisat 18-Hz footprints (black lines in Figure 17) have been extracted, unwrapped, and converted to vertical displacements. Since InSAR can measure only spatially relative water level changes, arbitrary constants (+0.766 m and −0.441 m for Figure 17(a), (b), respectively) have been added (red "+" in Figure 3-18) for better comparison with Envisat altimetry results in Figure 3-18. The InSAR and Envisat altimetry water level changes agree quite well with Root-Mean-Square-Error (RMSE) of

18.3 cm and 9.7 cm for the interferograms in Figure 3-17(a), (b), respectively. This further validates altimetry's capability for measuring water level changes beneath dense forest canopy.

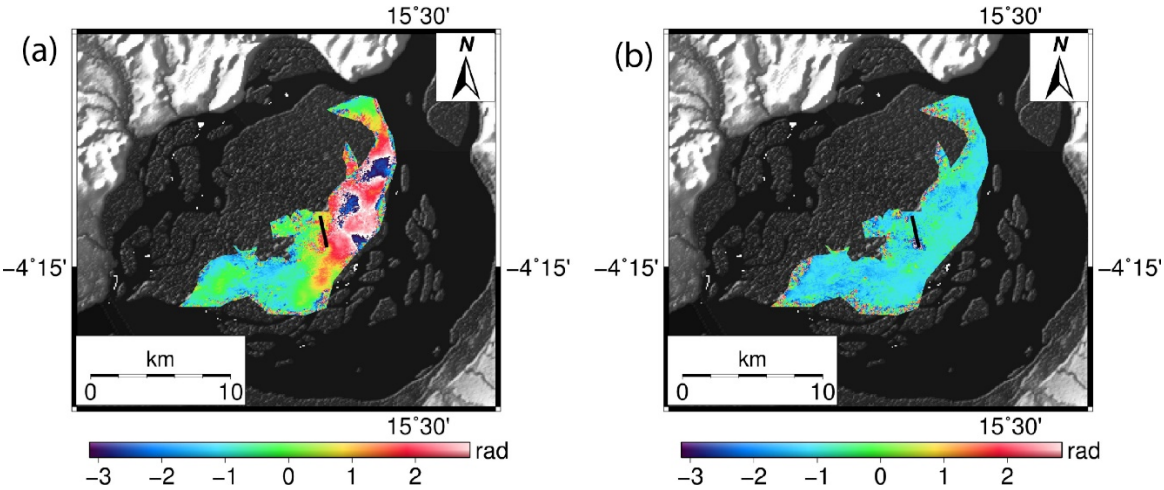

Figure 3-17 Wrapped differential interferograms over the Île Mbamou representing water level changes over the southern forested land between (a) October 26 2007–December 11 2007; and (b) December 16 2009–January 31 2010.

Next, water level changes obtained from Envisat altimetry (blue dots), InSAR (red pluses) and model predicted Δh using Equation (3-3) (magenta diamonds) were compared in Figure 3-18. Green dots in Figure 3-18 represent the footprint locations where Envisat altimetry water level changes and σ_0 are used to construct the regression model in Figure 3-16. The differences between model predicted Δh and altimetry derived water level changes are listed in Table 3-6. A mean RMSEs of 48.95 cm was obtained for the period of October 26 2007–December 11 2007 and 64.69 cm for the period of December 16 2009–January 31 2010 over the forested area. The large difference between Δh from Equation (3-3) and altimetry shown in red box in Figure 3-18, which indicates the boundary between the forested and non-forested areas, could be caused by errors in the VCF product in distinguishing different vegetation densities with its coarser spatial resolution (~250 m) than PALSAR (~30 m). If those footprints (footprints 11 and 12) are excluded, RMSEs

will be 37.86 cm for the period of October 26, 2007–December 11, 2007, and 58.80 cm for the period of December 16, 2009–January 31, 2010 in the non-forested area which is comparable with the result in (*Grings et al.*, 2008) that achieved 22 cm RMSE for the estimated water levels over marshes in the Parana Basin using Envisat ASAR σ_0 and electromagnetic models that address the vegetation structure and interaction mechanism. It is noted that our approach does not rely on any electromagnetic models requiring detailed vegetation properties (*Grings et al.*, 2006, 2008) or *in situ* measurements (*Kim et al.*, 2014) that may be rarely available over the remote river basins.

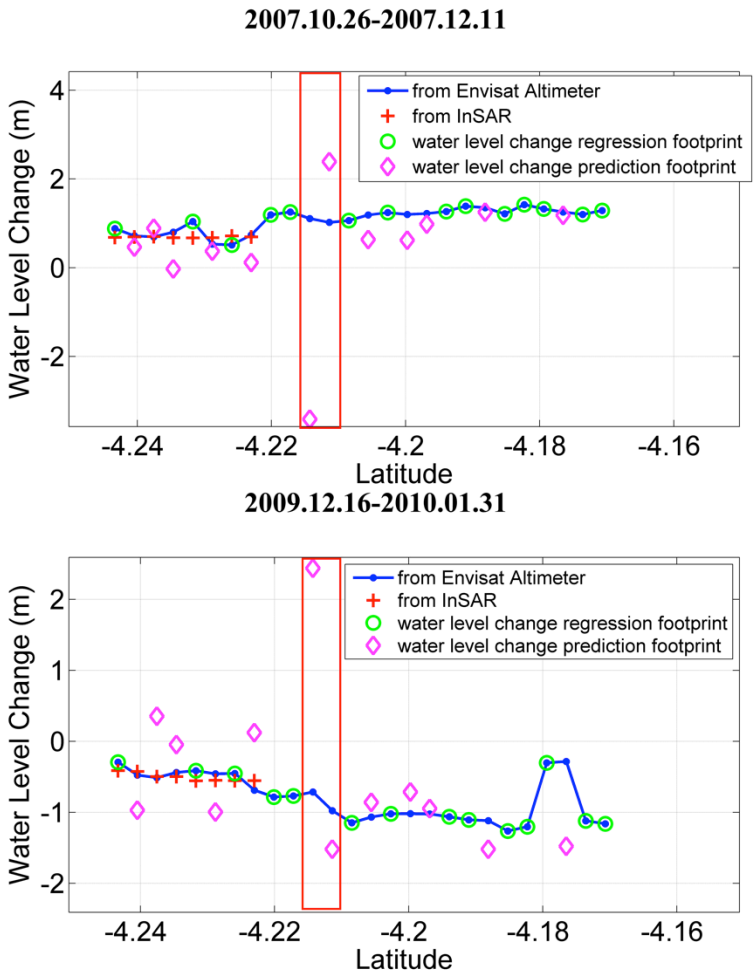

Figure 3-18 Comparison of water level changes obtained from Envisat altimetry, InSAR and regression model. The red boxes show the measurements at the boundary of forested and non-forested regions.

Table 3-6 Differences of Δh from Equation (3-3) and Envisat altimetry (purple in Figure 3-18). Values in parentheses are footprints located at the boundary of the forested and non-forested lands that were excluded in the RMSE computation.

	Differences for the Period of 26 October 2007–11 December 2007 (cm)	Differences for the Period of 16 December 2009–31 January 2010 (cm)
Forested Land	25.35	49.44
	−19.75	−86.56
	82.80	−39.20
	15.94	53.77
	61.97	−80.99
RMSE	48.95	64.69
Non-Forested Land	(452.42)	(−315.31)
	(−136.88)	(54.33)
	55.48	−20.67
	57.98	−30.43
	23.87	−7.70
	10.06	40.32
	7.56	119.36
RMSE	37.86	58.80

3.6 Conclusions

This study describes the seasonal variations of PALSAR σ_0 over the wetlands in the island of Île Mbamou where two distinctly different vegetation types are found, and its relationships with water level changes obtained from Envisat altimetry have been investigated. Positive correlation exists between σ_0 and water level changes over the forested land whereas both positive and negative correlations are observed over the non-forested land depending on the amount of water level increase. It was shown that the PALSAR backscatter response is enhanced during early water increasing season and then diminished with more increase in water level over the non-forested land. This study also performed the analysis of σ_0 sensitivity, and found that denser vegetation canopy leads to less sensitive σ_0 variation with respect to the water level changes regardless of the vegetation type (forested or non-forested). Furthermore, based on the σ_0 sensitivity

analysis, water level changes were obtained which were then compared with the Envisat altimetry measurements. Mean RMSEs of 57 cm and 48 cm were obtained over the forested and the non-forested lands by excluding the boundary footprints. Possible error sources include Envisat altimetry interpolation error, speckle noise in σ_0, resolution mismatch between σ_0 and VCF, and uncertainties in linear regressions. However, if considering most of the contemporary wetland hydrodynamic modeling has a scale of several hundred meters (*Wilson et al.*, 2007; *Jung et al.*, 2012), the overall mean RMSE of 53 cm at 30-m scale (SAR resolution), which can be interpreted as 5.3 cm RMSE at 300-m scale if the pixel-to-pixel noise is uncorrelated, shows that the method can be useful for calibration and validation of a hydrodynamic model.

In order to demonstrate that this method can be applied to other wetlands, a similar sensitivity analysis over the Everglades wetlands was performed. The regression slopes obtained using *in situ* water level changes and PALSAR σ_0 changes over six gauge locations (six red dots in Figure 3-19) in the non-forested, sawgrass-dominated Water Conservation Areas (WCAs) from Figure 4 of (*Kim et al.*, 2014) (using Path 149 results) were utilized. VCF values were extracted over those six gauge locations and a similar sensitivity analysis as in Figure 3-15 was performed. As it shows in Figure 3-19, a similar positive correlation is observed between the VCF and the regression slopes (dB/m) as in Figure 3-15(b). Therefore, although it is not possible to perform similar analysis over other forested areas due to the lack of *in situ* data, it is expected that water level changes can be estimated over wetlands based on different L-band σ_0 responses to water level changes in different vegetation fields.

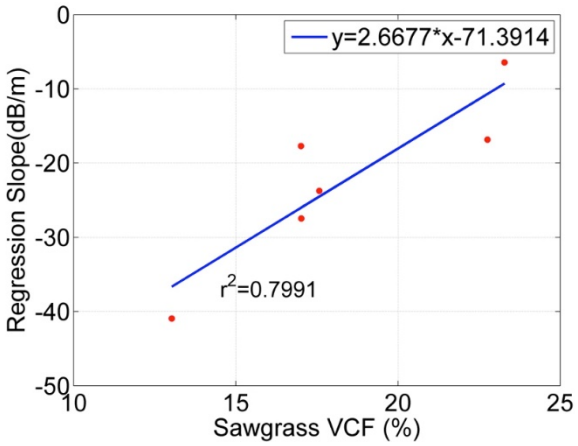

Figure 3-19 Regression analysis between the regression slopes (dB/m) and VCF over the six gauges located over the sawgrass-dominated Everglades wetlands.

For a future study, two-dimensional maps of water level changes obtained can be generated using Equation (3-3). To do so, it is noted that a more detailed VCF-like map, which has a high spatial resolution similar to that of the SAR image, is needed to estimate the water level change at each of SAR pixel. Although the map will not have the centimetric accuracy as the repeat-pass InSAR provides, it would still be useful over wetlands with low canopy such as the non-forested areas, where InSAR loses its coherence and thus interferograms cannot be generated. On the other hand, this method can also provide a useful independent dataset for the planned Surface Water Ocean Topography (SWOT) satellite mission which is a single-pass Ka-band radar interferometer that will provide simultaneous measurements of water levels and inundated area for inland water bodies. Currently, InSAR is the only tool that can provide a comparable dataset for SWOT observations over the wetlands. However, again, as can be seen in Figure 3-17, interferometric coherence cannot be maintained over the non-forested land, and InSAR requires a stable corner-reflector such as tree trunks to maintain interferometric coherence over the wetlands (*Lu and Kwoun*, 2008).

Chapter 4 Congo Wetland Hydraulics using PALSAR InSAR and Envisat Altimetry Data

4.1 Introduction

Water flow through the wetlands, which governs biogeochemical process, sediment delivery and nutrient exchange, is probably the most important controlling factor (*Mitsch and Gosselink*, 2007). However, the complexity of floodwater flows has not been well captured because floodwater moves laterally across wetlands and its movement is not bounded like that of typical channel flow. Water flow across wetlands is more complex than implied by one-dimensional, point-based measurements.

As an active microwave sensor, SAR has all-day and all-weather imaging capability. InSAR technique has been successfully used to map relative $\partial h/\partial t$ in the wetlands with high spatial resolution (~30 m) and centimetric accuracy (*Alsdorf et al.*, 2001; *Lu and Kwoun*, 2008; *Wdowinski et al.*, 2008). However, the interferograms can only provide a spatially relative gradient of water level changes. Therefore, a vertical reference is needed to convert the relative changes into absolute changes (*Kim et al.*, 2009). Since most wetlands are not monitored by *in situ* gauges, satellite altimetry-derived water level change has been used as the vertical reference instead (*Kim et al.*, 2009). Therefore, by integrating satellite radar altimetry and InSAR data, mapping spatially detailed absolute $\partial h/\partial t$ in the wetlands becomes possible.

Only a couple of studies have used InSAR and satellite altimetry data to explore the hydraulics of the Congo's wetlands. *Jung et al.* (2010) used two interferograms generated with L-band JERS-1 images obtained in 1996 over the interfluvial wetlands near

the confluence of the mainstem and its major tributaries including the Ubangi and Sangha, and reported that the flow patterns are not well defined and have diffuse patterns. *Lee et al.* (2015) generated two PALSAR interferograms over the similar central regions and revealed dense fringe patterns showing increasing $\partial h/\partial t$ toward the mainstem. Since multi-temporal water level changes and hydraulic processes have not been extensively investigated, this study aims to generate multiple temporal absolute $\partial h/\partial t$ maps over the middle reach of the Congo near the city of Lisala using PALSAR images, and quantifying and characterize the flow dynamics in the wetlands.

4.2 Study Area

The study area is located along the middle reach of the Congo mainstem, as shown in Figure 4-1, near the city of Lisala, the capital of the Mongala District in the Democratic Republic of the Congo. Large islands can be seen in the river, which is typical in the Congo River. The wetlands next to the mainstem and the islands are covered with seasonally flooded forest (*Hansen et al.*, 2008). The river surface slope is relatively high (6~8 cm/km) compared to other reaches of the Congo River (*O'Loughlin et al.*, 2013).

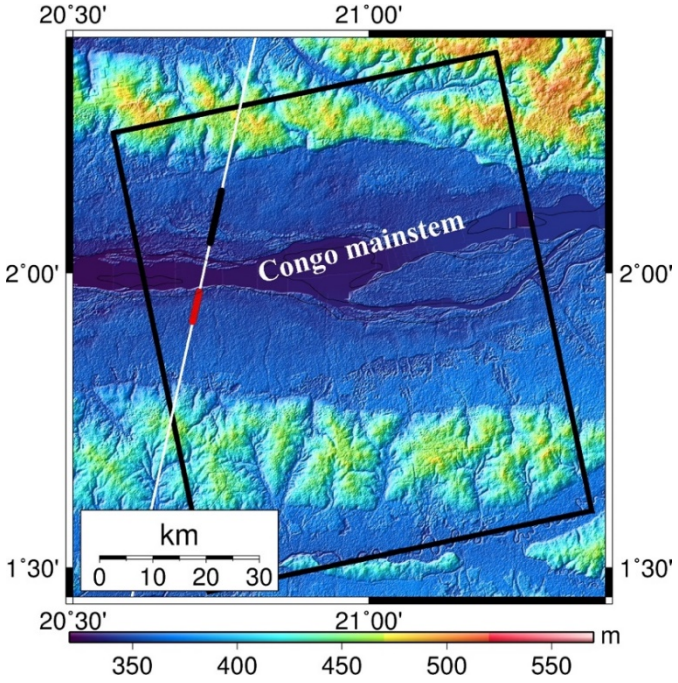

Figure 4-1 Study area with Envisat pass 300 (white line), coverage of ALOS PALSAR (black box), and intersections of Envisat pass with the southern (red dots) and northern (black dots) wetlands. Background is from C-band SRTM DEM.

4.3 Dataset

4.3.1 Envisat Altimetry

Envisat RA2 GDR of pass 300 from Oct 2002 to Sep 2010 has been used in this study. As explained in Section 3.3.1, ICE-1 retracked measurements contained in Envisat RA2 GDR were used.

4.3.2 ALOS PALSAR

Sixteen fine-beam mode ALOS PALSAR images were used in this study, as summarized in Table 4-1. Seven of them were obtained with FBS mode (HH polarization) while the other eleven were obtained with FBD mode (both HH and HV polarizations). As explained in Section 3.3.2, HH polarization mode SAR images were adopted in this study.

FBD HH data shown in Table 4-1 were oversampled by a factor of 2 to obtain consistent resolution as FBS HH data (see Section 3.3.2 for detail).

Table 4-1 List of PALSAR scenes used in this study.

Scene ID	Operation Mode	Date	Path	Frame	Polarization Mode
ALPSRP074660020	FBD	2007/6/19	640	20	HH/HV
ALPSRP121630020	FBS	2007/8/4	640	20	HH
ALPSRP269250020	FBD	2007/9/19	640	20	HH/HV
ALPSRP262540020	FBS	2007/12/20	640	20	HH
ALPSRP101500020	FBS	2008/3/21	640	20	HH
ALPSRP222280020	FBD	2008/5/6	640	20	HH/HV
ALPSRP155180020	FBD	2008/6/21	640	20	HH/HV
ALPSRP114920020	FBS	2008/12/22	640	20	HH
ALPSRP081370020	FBD	2009/6/24	640	20	HH/HV
ALPSRP215570020	FBD	2009/9/24	640	20	HH/HV
ALPSRP249120020	FBS	2010/2/9	640	20	HH
ALPSRP182020020	FBD	2010/5/12	640	20	HH/HV
ALPSRP128340020	FBD	2010/6/27	640	20	HH/HV
ALPSRP088080020	FBD	2010/9/27	640	20	HH/HV
ALPSRP228990020	FBS	2010/12/28	640	20	HH
ALPSRP235700020	FBS	2011/2/12	640	20	HH

4.4 Results and Discussions

4.4.1 Inundated Areas from PALSAR Backscattering Coefficients

The energy backscattered to the SAR antenna is sensitive to surface roughness, dielectric constant and terrain slope (*Bayer et al.*, 1991; *Mattia et al.*, 1997; *Freeman and Durden*, 1998). Accordingly, SAR intensity images have been utilized to map inundated areas based on different radar backscattering mechanisms depending on different vegetation types. Over open water surface, the radar pulse follows a specular travel path, which results in little energy backscattered to the SAR antenna. In cases of dry vegetation, the backscattering is dominated by volume backscattering from the vegetation canopy. On the other hand, over inundated but not submerged vegetation, the water surface and vegetation trunk allow the radar pulse to follow a double bounce travel path to the antenna. This double-bounce backscattering from the inundated vegetation results in brighter SAR intensity, compared to non-flooded vegetation. This phenomena has been reported by a number of studies, such as (*Hess et al.*, 1995; *Pope et al.*, 1997; *Lu and Kwoun*, 2008). Based on the fact that variation of hydrologic condition influences the signal amplitude backscattered to the SAR antenna, SAR images have been used to delineate flooded and non-flooded areas in the wetlands (*Hess et al.*, 1995, 2003; *Rosenqvist and Birkett*, 2002; *Lee et al.*, 2014).

To identify inundated areas, σ_0 from PALSAR images were used in this study. After generating SLC images from SAR raw data, all of the SLC images were first co-registered to a common SLC image obtained on September 19 2007. Secondly, all of the SAR images were multi-looked by a factor of 4×9 to reduce the speckle noise. Next, the multi-looked SAR intensity images were geocoded using the 1-arcsec SRTM DEM. Finally,

the backscattering coefficients were calculated using Equation (4-1) with the geocoded SAR images, following the method in (*Yuan et al.*, 2015). A median filter of 5 × 5 was applied to further reduce the speckle noise.

$$\sigma_0 = 10log_{10}(DN^2) + CF\ (dB), \tag{4-1}$$

where DN is the digital number of the geocoded SAR amplitude image, and CF is the radiometric calibration factor. The value of CF is -51.8 for FBD HH data and -51.9 for FBS HH data (*Werner et al.*, 2000).

Figure 4-2 shows the spatial and temporal variations of the calculated σ_0. The Congo mainstem shows constantly low σ_0 in all of the σ_0 images because of specular backscattering from open water surfaces. Significant temporal variations of σ_0 can be observed in the wetlands located along the mainstem. For example, the SAR image obtained on December 20 2007 shows the highest σ_0 while the SAR image obtained on February 11 2011 shows the lowest σ_0. Threshold classifier is a simple yet effective method to delineate inundation extents and vegetation types, and has been implemented in a number of studies, e.g. (*Hess et al.*, 2003; *Rosenqvist*, 2008; *Lee et al.*, 2014). Here, a threshold of −6 dB is used to classify inundated and non-inundated forest areas (*Lee et al.*, 2014). The threshold of −6 dB has been determined based on the feasibility of generating water level change time series using Envisat altimetry, and used in the central Congo wetland delineating the flooded and non-flooded forests with PALSAR ScanSAR images (*Lee et al.*, 2014). Then, the SAR pixels with σ_0 lower than −14 dB were classified as non-vegetated flooded areas (open water surface) as in (*Hess et al.*, 2003). The estimated inundation maps are shown in Figure 4-3.The temporal variation of total inundated areas

are shown in Figure 4-4. The maps of inundated areas will be used later to determine if the interferometric phases were dominated by water level change or atmospheric artifacts.

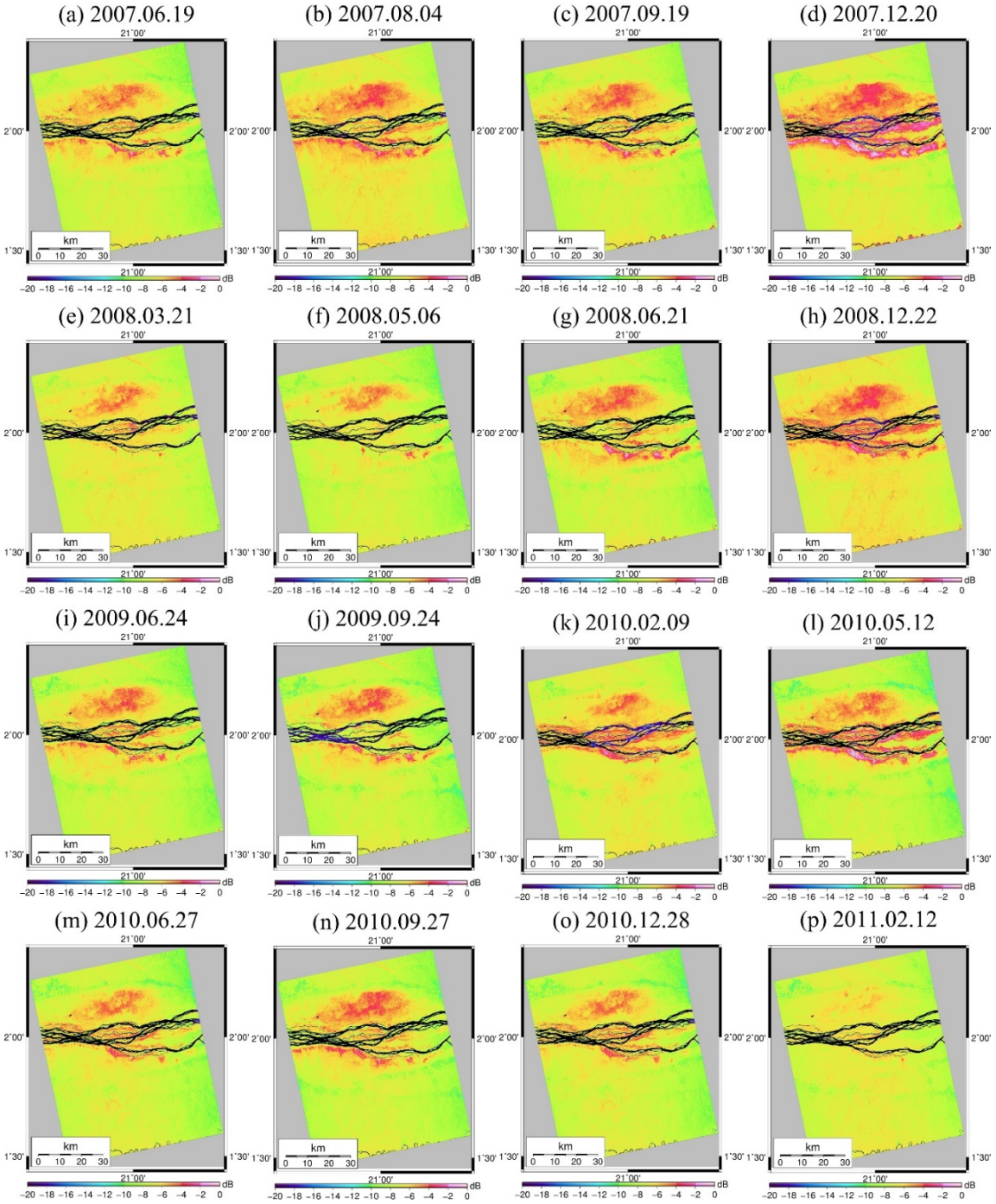

Figure 4-2 Maps of PALSAR backscattering coefficients showing seasonal variations over the wetlands.

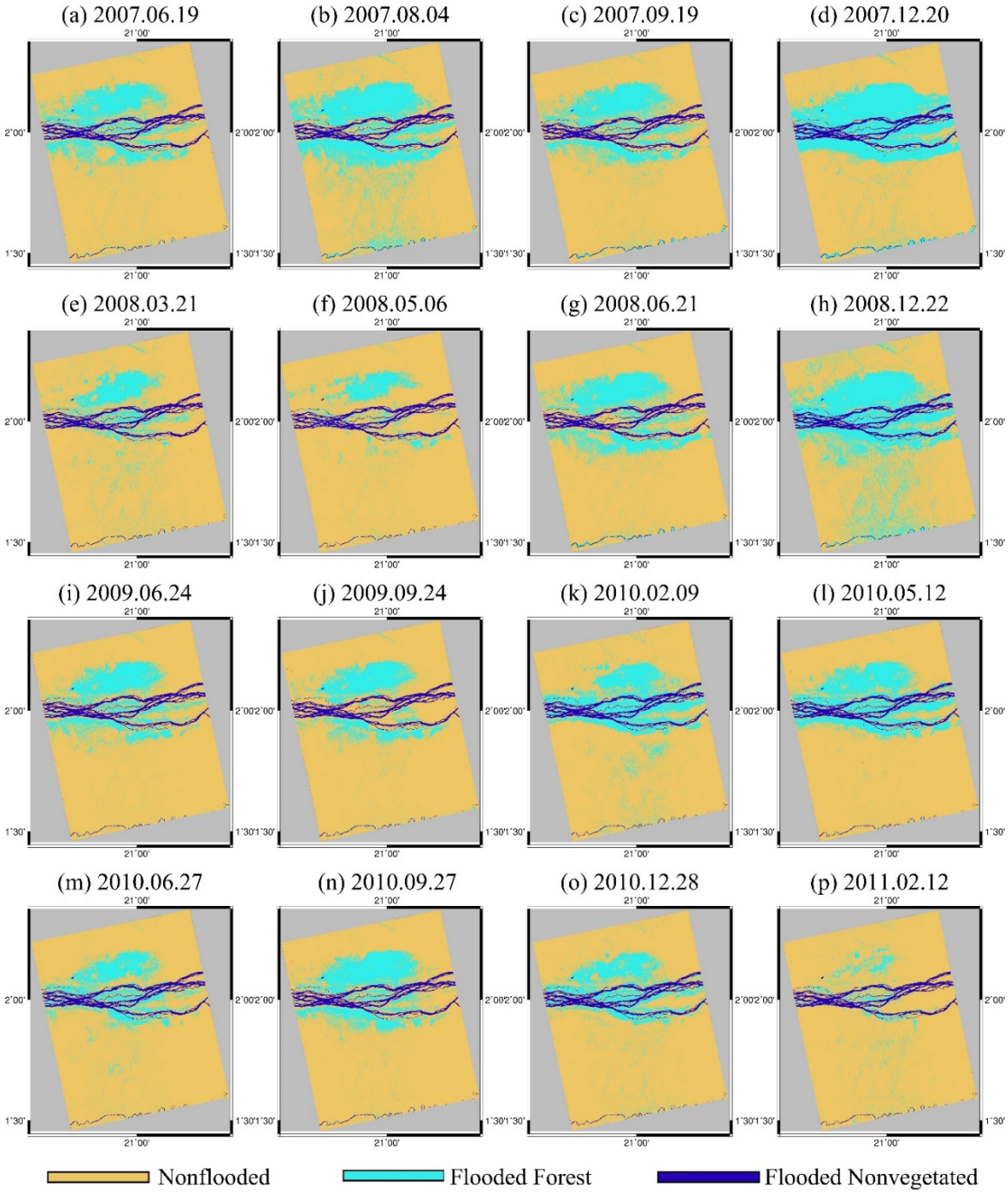

Figure 4-3 Classification maps of flooded non-vegetated (blue), flooded forests (cyan) and non-flooded areas (brown).

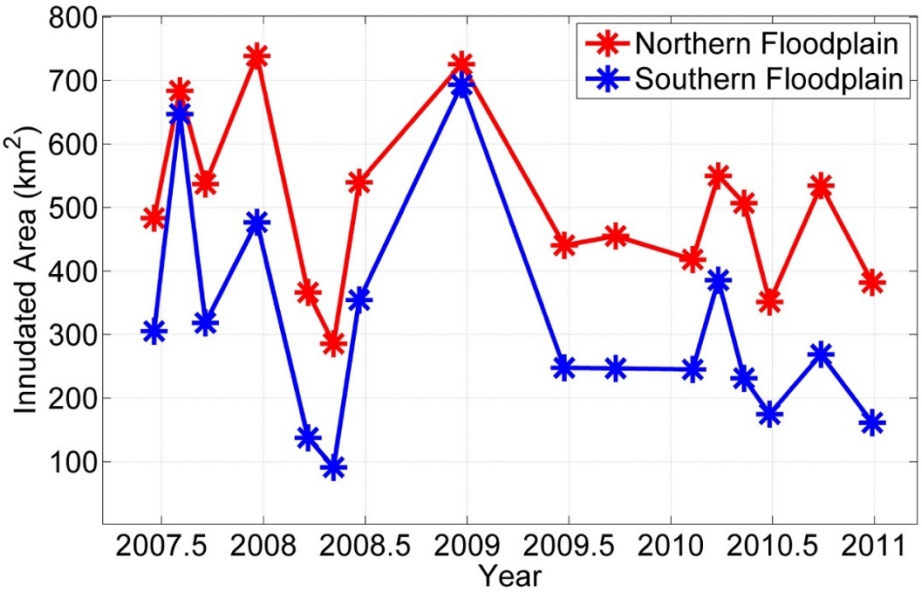

Figure 4-4 Temporal variation of total inundated areas.

4.4.2 InSAR Processing and Coherence Analysis

Two-pass repeat interferometry method has been applied to generate the interferograms. The interferometric processing uses two SAR images, obtained from different times with slightly different imaging positions. The two SAR images were firstly co-registered based on the correlation between the SAR intensity images. An interferogram was then generated by multiplying the first SAR image (master image) with the complex conjugate of the second co-registered SAR image (slave image). Flat earth phase was removed with the baseline and its variation throughout the interferogram using the satellite orbit information. The topographic phase in the interferogram was simulated using 1 arc-sec resolution SRTM DEM data, and then was subtracted from the interferogram. After removing the topographic component from the interferogram, a differential interferogram was generated which represents the relative $\partial h/\partial t$ in the wetlands. The residual phase trend throughout the differential interferogram caused by inaccurate orbit information was

estimated using a second-order polynomial, and then removed from the differential interferogram.

Overall, fifteen wrapped differential interferograms were generated as shown in Figure 4-5. The interferograms were generated using the Small Temporal Baseline Subset (STBAS) strategy (*Hong et al.*, 2010). The STBAS method generates interferograms with small temporal baseline criterion in order to obtain better coherence in wetland environments (*Kim et al.*, 2013). Following the STBAS method, interferograms were generated using every consecutive SAR image pairs except one interferogram shown in Figure 5 (d) generated using SAR images obtained on December 20 2007 and June 21 2008. The SAR image obtained on June 21 2008 was used as the slave image instead of the SAR images obtained on March 21 2008 or May 6 2008 which would have led to the interferogram with shorter temporal baseline. Because the SAR images obtained on March 21 2008 or May 6 2008 represent the dry season with the least inundated extents (see Figure 3), the interferograms generated with those SAR images as the slave images lost coherence. Thus, the interferogram was generated with the SAR image obtained on June 21 2008 as the slave image instead. The temporal and perpendicular baselines of the interferograms and the coherences over the wetlands are summarized in Table 4-2 (the letter in the first column is used to refer each interferogram hereafter). The coherence values were calculated only over the wetlands, located in the south and north of the mainstem. The extents of the southern and northern wetlands were delineated using the SAR image obtained on December 20 2007, which has the highest σ_0. The coherences listed in Table 4-2 are overall higher than 0.2 (except for the interferograms (d) and (s)), indicating that the interferometric phases are overall well maintained using STBAS.

Table 4-2 List of ALOS PALSAR interferometric pairs.

Pair	Master Date	Slave Date	Temporal Baseline (days)	Perpendicular Baseline (m)	Mean Coherence in southern wetland	Mean Coherence in northern wetland
(a)	20070619	20070804	46	273.20	0.34	0.33
(b)	20070804	20070919	46	-449.90	0.29	0.25
(c)	20070919	20071220	92	-36.37	0.29	0.29
(d)	20071220	20080621	92	-248.69	0.20	0.19
(e)	20080321	20080506	46	579.67	0.23	0.28
(f)	20080506	20080621	46	456.64	0.26	0.31
(g)	20080621	20081222	184	-828.84	0.22	0.23
(h)	20081222	20090624	184	397.32	0.19	0.20
(i)	20090624	20090924	92	-270.75	0.28	0.38
(j)	20090924	20100209	138	275.42	0.23	0.23
(k)	20100209	20100512	92	283.69	0.20	0.20
(l)	20100512	20100627	46	114.33	0.28	0.32
(m)	20100627	20100927	92	388.08	0.25	0.30
(n)	20100927	20101228	92	-544.35	0.24	0.24
(o)	20101228	20110212	46	364.13	0.25	0.26

The fringe patterns of the interferograms in the wetlands can be characterized by spatial patterns of water level changes and atmospheric artifacts. The interferometric phases due to water level changes and atmospheric artifacts have similar wavelength (*Hong et al.*, 2010). Thus, the approach used in *Mora et al.* (2002) to remove the atmosphere artifacts by applying a high-pass filter in time domain cannot be used in the wetlands

environment. However, the σ_0 images can be used to determine if the fringes in the interferogram are likely to be caused by water level change or atmospheric delay (*Lu and Kwoun*, 2008). In addition, it is expected that the fringes due to water level change should exhibit seasonal dynamics which are different from atmospheric artifacts, characterized by high spatial correlation but low temporal correlation (*Berardino et al.*, 2002). Based on these two criteria, three fringe patterns caused by water level changes were identified.

The first pattern is the fringes parallel to the Congo mainstem flow direction observed in the southern wetland, as shown in Figure 4-5 (c, d, g, h, j, k, l), and in the northern wetland, as shown in Figure 4-5 (c, d, j, k). These fringes are likely due to water level changes, not atmosphere delays. First of all, the atmosphere artifacts cannot result in such repeated patterns along the river. In addition, the locations of the fringes correspond to locations with significant σ_0 variations, implying variations in hydrologic conditions. Furthermore, these parallel fringe patterns are commonly observed in a number of interferograms along the mainstem, which further indicates that it is not due to the atmosphere effect. The second fringe pattern that could be due to water level change is the broad flooding pattern perpendicular to the Congo mainstem in the northern wetland which is observed in interferograms shown in Figure 4-5 (a, b, l). Similar to the first fringe pattern mentioned above, the atmosphere effect cannot result in this repeated fringe pattern. The third phase that could be due to water level change is the fringes observed along the boundary between the northern wetland and the upland, as can be seen from Figure 4-5 (f, m). The broad radial phase patterns in the southwestern edge of Figure 4-5 (i), and southeastern edge of Figure 4-5 (k), and the broad red phase pattern in Figure 4-5 (l), are

likely caused by atmospheric delay, not water level changes because of negligible variation in σ_0 as shown in Figure 4-2.

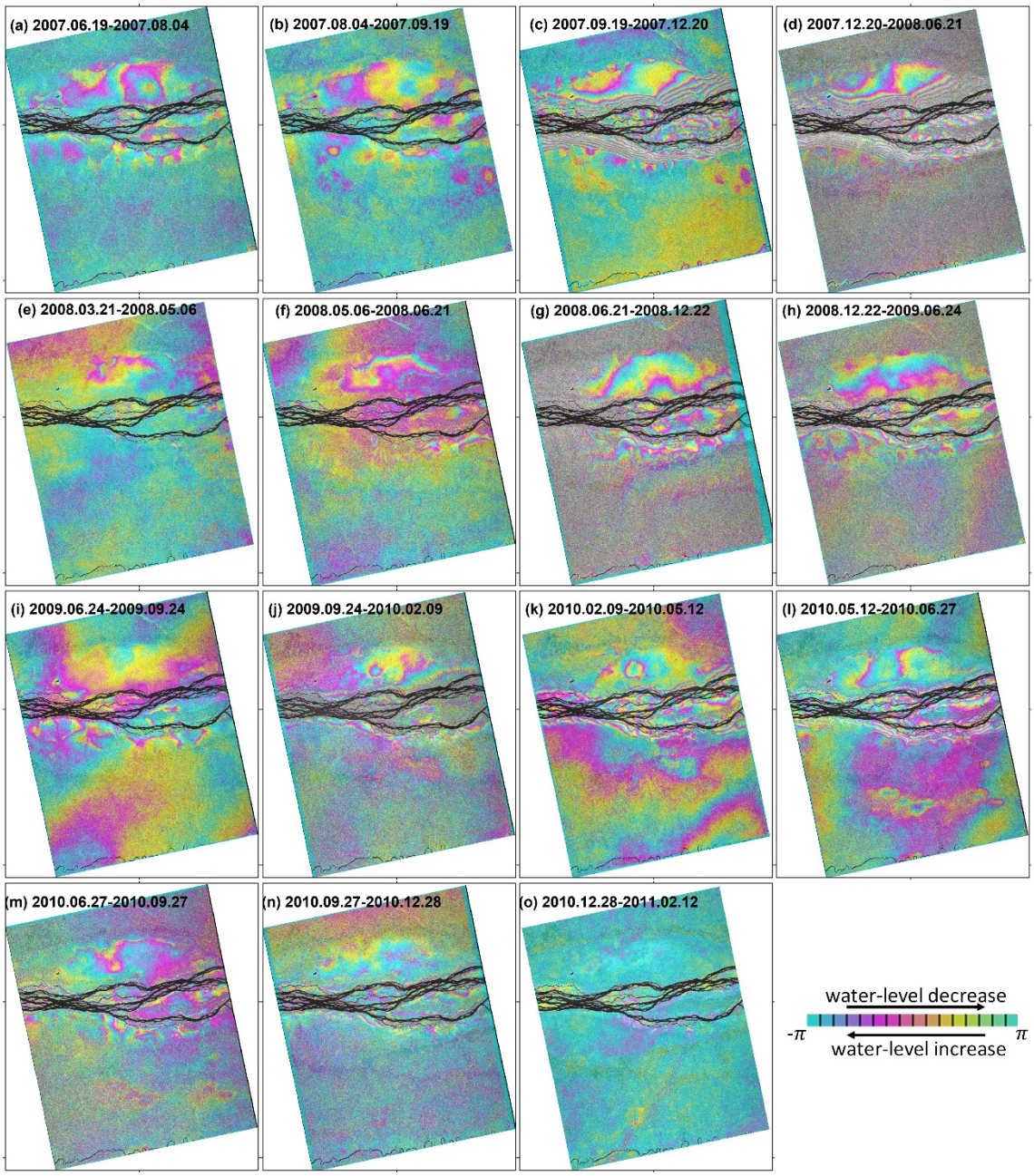

Figure 4-5 Wrapped PALSAR differential interferograms.

4.4.3 InSAR-derived $\partial h/\partial t$

Measurements of $\partial h/\partial t$ from InSAR were obtained by unwrapping the differential interferograms in Figure 4-5. Six interferograms (a, c, d, f, l, m) were selected for unwrapping as examples for each fringe pattern identified in Section 4.4.2 above. The interferograms (c) and (d) were selected for the first phase pattern (dense fringes parallel to the mainstem), (a) and (l) for the second phase pattern (broad fringes perpendicular to the mainstem), and (f) and (m) for the third fringes pattern observed along the boundary of northern wetland.

Because InSAR-derived $\partial h/\partial t$ only represents spatially relative water level changes in the wetlands (*Alsdorf et al.*, 2007a; *Kim et al.*, 2009; *Lu et al.*, 2009), a vertical reference (or offset) is necessary to convert the relative water level changes from InSAR to absolute water level changes. Since there is no *in situ* gauge in the study area, the offset estimation has been performed using two different methods. The first method is to use the water level change observed from Envisat altimetry as the offset for the interferograms in Figure 4-5(c, d). Profile comparisons of Envisat altimetry and InSAR measurements are shown in Figure 4-6 in order to examine the feasibility of using altimetry-derived water level changes as the offsets. Figure 4-6(a,b) show the profiles of Envisat altimetry-derived and InSAR-derived water level changes extracted along the Envisat altimetry ground track from interferograms shown in Figure 4-5(c,d). Figure 4-6(b,e) show the statistical comparsion between them over the southern wetland and Figure 4-6(c,f) illustrates the comparsion over the northern wetland. The location of the measurements within the southern floosplain and northern wetland is marked as red dots and black dots in Figure 4-1.

In Figure 4-6, the Envisat altimetry measurements have been interpolated to the SAR acquisition times. However, it should be noted that satellite altimetry measurements in the dry season can be erroneous such as the black dots in Figure 4-6(d), which have been excluded from the offset estimation. The comparison shows a good agreement between altimetry and interferograms (c, d) for the high water level season. The R-squared values are high varying from 0.8 to 0.93 and the root-mean-square differences are low varying from 7 cm to 11 cm. After unwrapping these interferograms and applying the offsets estimated from Figure 4-6, absolute $\partial h/\partial t$ maps were generated as shown in Figure 4-7 (a, b). The absolute water level change maps in Figure 4-7 (a, b) suggest that the proximal (channel marginal) wetland close to the mainstem has the largest water level change during high water season. The absolute $\partial h/\partial t$ range up to 1.2 m to 1.4 m over both the southern and northern wetlands.

For the interferograms (a, f, l, m), because they were not obtained in high water season, the Envisat altimetry measurements become too noisy to be used to estimate the offsets. However, by visually examining the two SAR images (obtained on June 19 2007 and August 4 2007) used to generate the interferogram (a), the SAR image obtained on August 4 2007 has higher σ_0 than the SAR image obtained on June 19 2007. The higher σ_0 is expected to be due to higher water level. Thus, the absolute $\partial h/\partial t$ is also expected to show positive (or increasing) water level change. With this positive water level change direction, the absolute $\partial h/\partial t$ map was generated in Figure 4-7 (c) by assigning zero to the pixel which has the lowest $\partial h/\partial t$. In this case, as it cannot be assumed that the wetlands have been completely drained on June 19 2007 based on its σ_0 image, this map is only used to examine whether $\partial h/\partial t$ has increased or decreased, and the directions of water flow.

Similarly, zero was assigned to the pixel with the lowest $\partial h/\partial t$ for the interferograms (f, m), to obtain the absolute $\partial h/\partial t$ maps shown in Figure 4-7 (e) and (f). For interferogram (l), the SAR image obtained on May 12 2010 has higher σ_0 than the SAR image obtained on June 27 2010. With decreasing σ_0, interferogram (l) is expected to show water level decreasing. Accordingly, zero was assigned to the pixel with the highest $\partial h/\partial t$ for interferogram (l) to obtain the absolute $\partial h/\partial t$ map shown in Figure 4-7 (d). Although Figure 4-7 (c)-(f) are not the true absolute $\partial h/\partial t$ maps, they still reflect the relative $\partial h/\partial t$ within the wetland. By visually observing the values in Figure 4-7 (c)-(f), the relative $\partial h/\partial t$ in the wetland are at decimeter level.

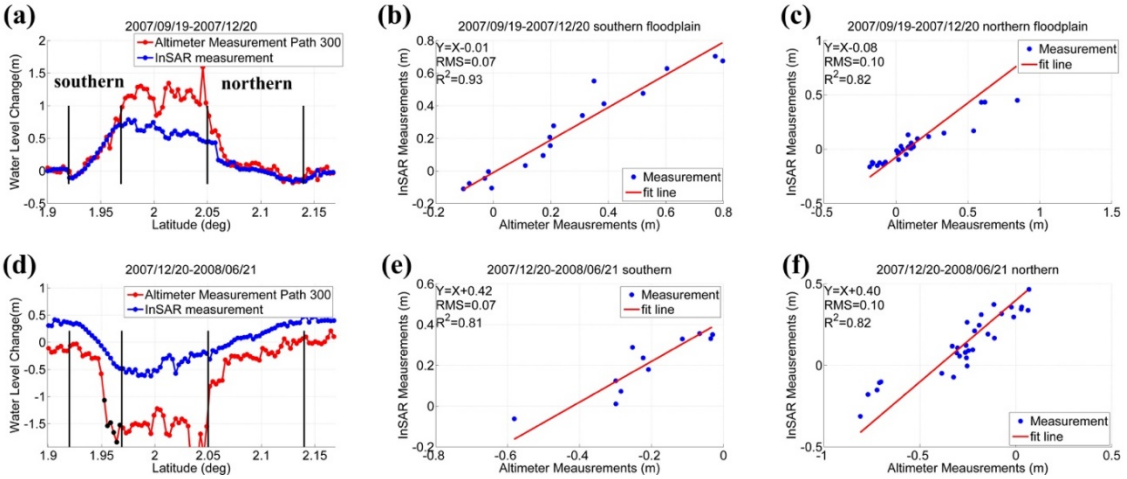

Figure 4-6 Offset estimation using Envisat altimetry-derived and InSAR-derived water level changes extracted along the Envisat altimetry ground track from interferograms shown in Figure 4-5 (c,d).

4.4.4 Hydraulic Processes from Absolute $\partial h/\partial t$

Based on the six absolute $\partial h/\partial t$ maps shown in Figure 4-7, the water flow hydraulics in the Congo wetland can be investigated based on mass continuity as in (*Alsdorf et al.*, 2007a) and (*Jung et al.*, 2010). This is based on the fact that the location

with greater $\partial h/\partial t$ receives more water than the locations with smaller $\partial h/\partial t$. Thus, the water should flow from smaller $\partial h/\partial t$ to greater $\partial h/\partial t$.

During high water season as shown in Figure 4-7 (a) and (b), both in the northern and southern wetlands, there is an overall increasing $\partial h/\partial t$ trend from upland to the mainstem. In other words, the proximal wetland closer to the mainstem has greater $\partial h/\partial t$ than the distal (valley marginal) wetland closer to the upland. Black flow arrows in Figure 4-7 (a) and (b) are based on continuity with directions pointing toward areas of greater water accumulation during water increasing times in Figure 4-7 (a) and pointing toward evacuation during water decreasing times in Figure 4-7 (b).

During low water season, $\partial h/\partial t$ shows a broad and diffuse pattern as discussed in Section 4.4.3. Hence, no obvious hydraulic processes based on subtle $\partial h/\partial t$ can be observed. Figure 4-7 (c) and (d) show broad water level change pattern parallel to the Congo mainstem in the northern wetland. Figure 4-7 (e) and (f) show water level change at the boundary in the northern wetland, with water flow from upland towards the wetland.

As in Figure 4-8, the relationship between our $\partial h/\partial t$ measurements and the 1 arc-sec resolution SRTM topography was examined for the broad and diffuse $\partial h/\partial t$ patterns observed in Figure 4-7 (c) and (d). The $\partial h/\partial t$ map, shown in Figure 4-7 (c), during the water filling period shows a flow convergence toward the red circular region. The $\partial h/\partial t$ and SRTM profile comparison in Figure 4-8 (a) shows that the greater $\partial h/\partial t$ values are within a topographic depression. On the contrary, the $\partial h/\partial t$ map in Figure 4-7 (d), during the water draining period shows a flow divergence from the identical depression area based on Figure 4-8 (b).

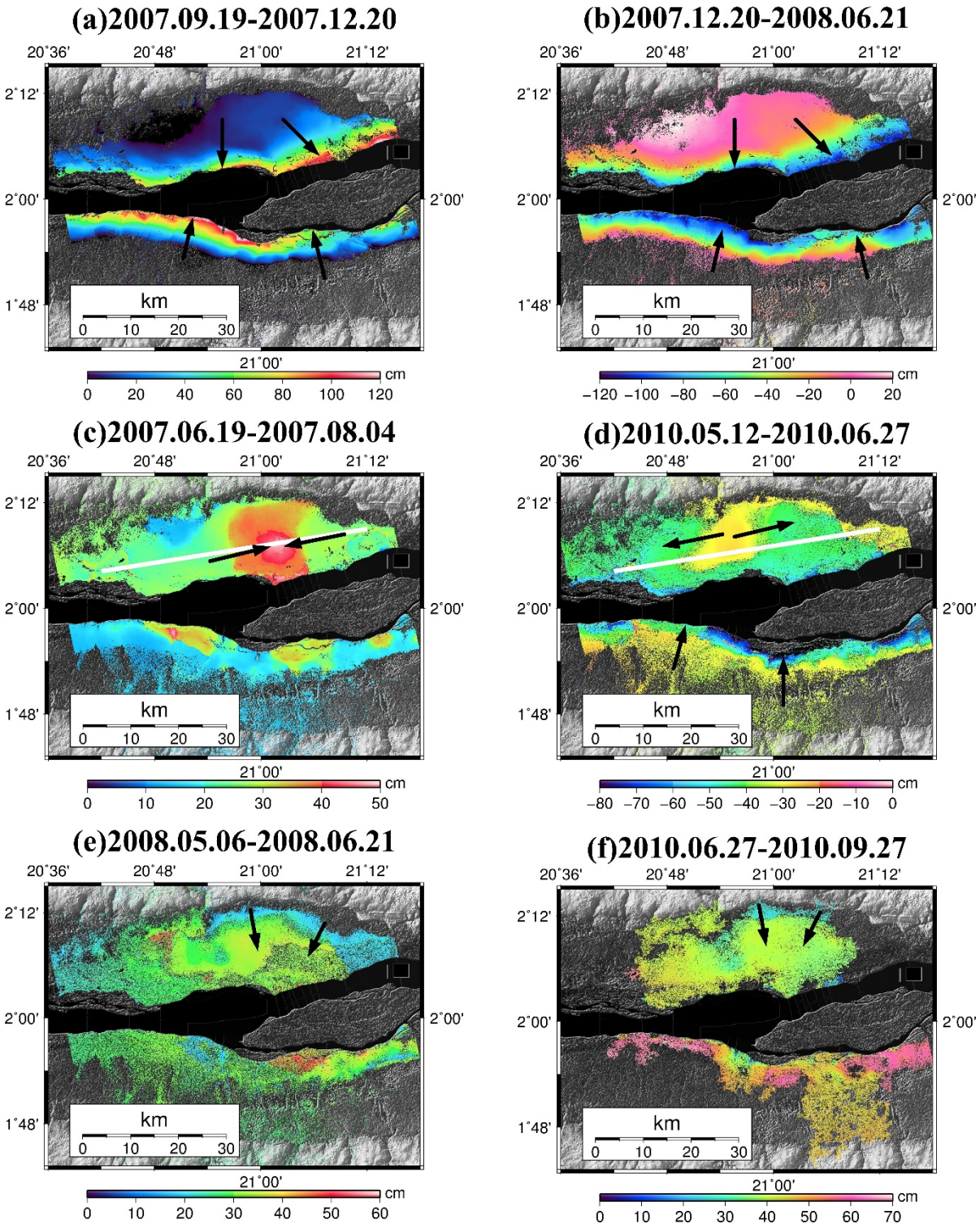

Figure 4-7 Absolute water level change map over the interfluvial wetlands from integration of Envisat altimetry and PALSAR InSAR. Black arrows show the water flow direction based on mass continuity.

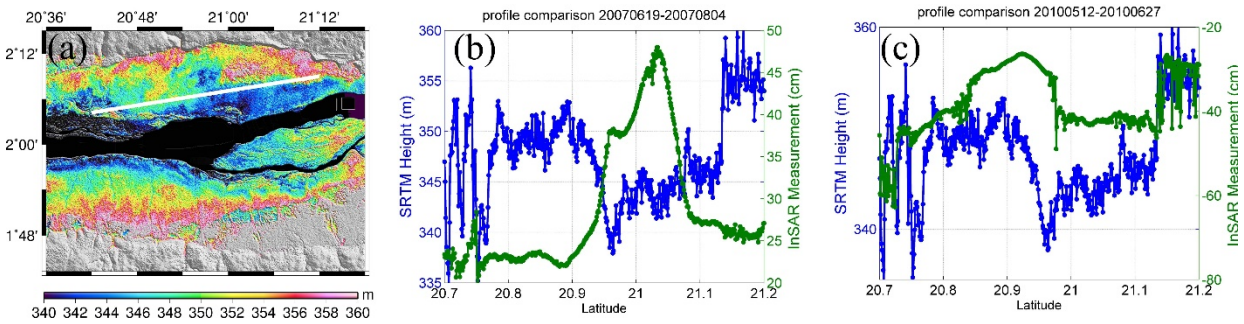

Figure 4-8 C-band SRTM DEM over the inundated wetlands (a). (b) and (c) show comparisons between absolute $\partial h/\partial t$ and SRTM topography extracted along the profiles shown as white lines in Figure 4-7 (c, d).

4.5 Conclusions

A stack of PALSAR interferograms was generated over the Congo wetland near the city of Lisala. Two absolute water level change maps were generated by integrating InSAR-derived relative $\partial h/\partial t$ and Envisat-derived absolute $\partial h/\partial t$. The proximal wetland close to the mainstem has greater absolute $\partial h/\partial t$ than the distal wetland close to the upland. Water level change differences within the wetlands can reach up to 1.2 m to 1.4 m while the difference is at decimeter level in low water season. The absolute $\partial h/\partial t$ maps have also been used to investigate the water flow hydraulics in the Congo wetland based on mass continuity. The absolute $\partial h/\partial t$ maps in low water season suggest that the water flow is not well confined and has a broad and diffuse pattern. On the other hand, the absolute $\partial h/\partial t$ maps in high water season show rapid spatial variation indicating water flow from the wetland toward the mainstem. The relationship between the absolute $\partial h/\partial t$ in low water season and SRTM elevation shows the low topography depression has greater water level changes during both the water filling and draining periods.

Chapter 5 Water Storages from Integration of Altimetry and InSAR

5.1 Introduction

The water storage over the wetlands represents a significant part of the water balance and water resource management in fluvial systems (*Richey et al.*, 1989; *Alsdorf et al.*, 2001). During water residence in the wetland, the biogeochemical environment of the floodwater is modified due to the influence of sedimentation, sorption and redox reactions and biotic processes (*Richey et al.*, 1989; *Hamilton*, 2002). The flux of sedimentation, nutrient and other solutes cannot be well estimated without knowing water storage variations in the wetland (*Richey et al.*, 1989; *Dunne et al.*, 1998; *Hamilton*, 2002).

Satellite remote sensing became a viable tool to investigate wetland water storage variations in large river basins. The Gravity Recovery and Climate Experiment (GRACE) has been applied to estimate total water storage (TWS) change in large river basins on a monthly basis (*Tapley et al.*, 2004; *Alsdorf et al.*, 2010; *Chen et al.*, 2010; *Lee et al.*, 2011). However, GRACE is limited by its coarse spatial resolution (~ 450 km by 450 km) (*Scanlon et al.*, 2012). Furthermore, GRACE does not measure surface water storage change directly, but captures all temporally varying components including not only surface water, but also snow, soil moisture and groundwater.

Alternatively, the water storage over the wetland can also be estimated by combining multiple remote sensing techniques. The L-band Synthetic Aperture Radar (SAR) instrument with a wavelength of 23.6 cm onboard JERS-1 and ALOS-1, have been successfully used to map the inundation extents of the forested wetlands in large river

basins (*Hess et al.*, 2003; *Rosenqvist and Birkett*, 2002; *Lee et al.*, 2014). By integrating the flooded extents derived from SAR images and water levels from satellite radar altimetry measurements, water storage changes in the forested wetlands were obtained (*Frappart et al.*, 2005; *Lee et al.*, 2014). In addition, SAR backscattering coefficients have been used to map water level changes in herbaceous wetlands (*Grings et al.*, 2006, 2008, 2009; *Kim et al.*, 2014; *Yuan et al.*, 2015) or in flooded forests (*Lee et al.*, 2015). However, the method relying on the SAR backscattering coefficients to estimate the flooded extents or water level changes is limited by the temporal coverage of the SAR data (*Prigent et al.*, 2007; *Aires et al.*, 2013). In other words, since the L-band SAR data is only provided by satellites JERS-1 (1992 – 1997), ALOS (2006 – 2011), and ALOS-2(2014 – present), there is a significant time span that is not covered by these datasets (e.g., 1998 – 2005). The lack of continuous long-term observations limits our understanding of the spatio-temporal changes of wetland storage. Moreover, the long revisiting periods of JERS-1 (44 days) and ALOS (46 days) can result in missing flooding periods if the water residence time is not long enough.

Given the short-term high spatial resolution SAR images to infer long-term inter-annual water storage variations, a new method is developed to estimate long-term local-scale (tens of kilometer) *absolute* water storage over the wetlands by establishing a water depth (d) versus volume (V) relationship using 2-D water depth maps from integration of InSAR and satellite altimetry measurements. This $d - V$ relationship is then combined with the water level measurements from Envisat altimetry to estimate absolute water storage over the wetland whenever the altimetry measurements are available. In this study, the $d - V$ relationship is established using PALSAR InSAR and Envisat altimetry over the

wetlands along the middle reach of the Congo River. A power function was used as in *Hayashi and Van Der Kamp* (2000) to model the $d - V$ relation and characterize the shape of the wetland bathymetry. Then this $d - V$ relation will be combined with Envisat altimetry measurements to generate long-term water storages time series for the period of 2002 – 2011 over the wetlands. The absolute water storages are then compared with the absolute water storages obtained from the water depth maps in (*Lee et al.*, 2015), TWS anomalies from GRACE, and precipitation anomalies from Tropical Rainfall Measuring Mission (TRMM).

5.2 Study Region and Dataset

5.2.1 Study Region

The study area covers the wetlands along the middle reach of the Congo River in the *Cuvette Centrale*, spanning from the cities of Lisala to Mbandaka (Figure 5-1). The vegetation over the riverine wetland is multi-layered (*Campbell*, 2005). The upper stratum is composed of evergreen forest with canopy heights of 35-45m (*Mayaux et al.*, 2000). These swamp forests are either permanently flooded or periodically flooded (*Hansen et al.*, 2008; *Bwangoy et al.*, 2010).

The average rainfall varies from 1,700 to 1,800 mm/year, and the evapotranspiration varies little across the whole basin, with estimated values from 1,100 to 1,200 mm/year (*Alsdorf et al.*, 2016). It is well known that the migration of rainfall across the basin results in a bi-modal hydrograph in the *Central Cuvette*, with a major peak around November to December and a minor peak around March to May (*Becker et al.*, 2014; *Alsdorf et al.*, 2016). The water level in the Congo mainstem fluctuates less than 3 m

(*Roberts and Stewart*, 1976). *Marlier* (1973) suggested that the little variation of the water level in the river could be due to the flat topography and attenuation of the flood waves by lakes and swamps.

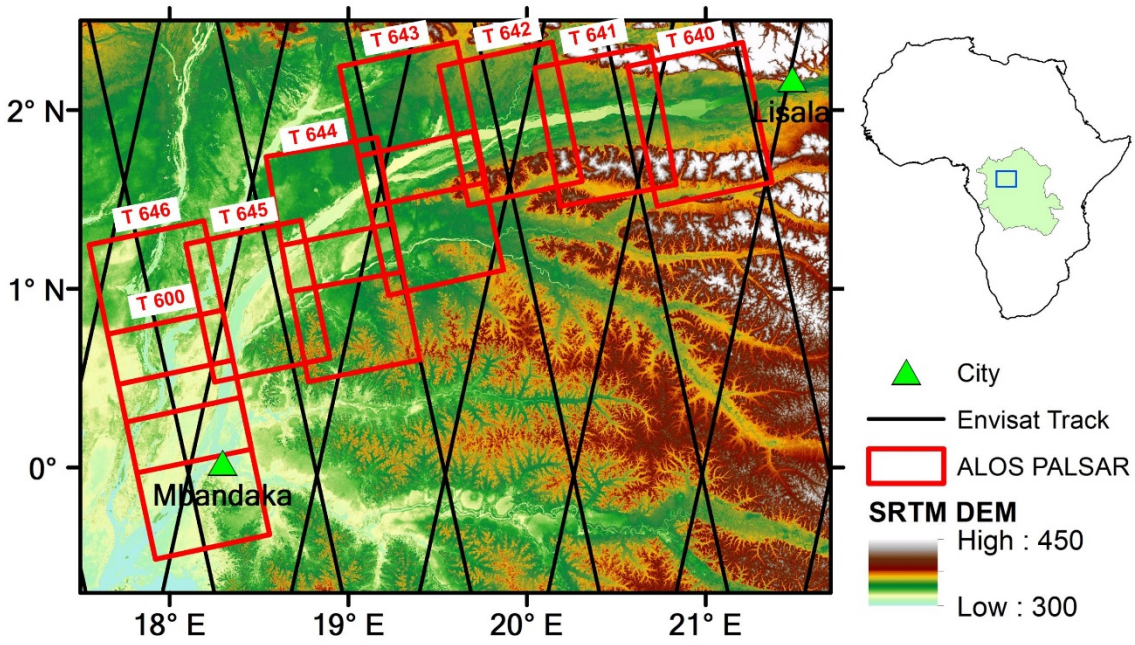

Figure 5-1 Map of study area with Envisat altimeter passes (black lines) and ALOS PALSAR coverage (red boxes). Background is topography from C-band SRTM DEM with a resolution of 30m.

5.2.2 Dataset

5.2.2.1 Envisat radar altimetry

In this study, Envisat RA2 GDR of passes 429, 930, 343, 386, 257, 300, and 715 was used with revisit period of 35 days from 2002 to 2010. ICE-1 retracked measurements were adopted in this study as explained in Section 3.3.1.

5.2.2.2 ALOS PALSAR data and its interferometric processing

ALOS PALSAR fine-beam images from 7 adjacent paths and 11 frames with total number of 151 were obtained, as summarized in Table 5-1. These PALSAR images were

acquired at L-band frequency with a nominal look angle of 34.3°. FBD HH SLC images were generated by oversampling with a factor of 2 in the range direction in order to obtain consistent resolution as FBS HH SLC images (see Section 3.3.2 for detail).

Differential interferograms were generated using the SLC images with multilook factor of 4 by 9 to reduce the speckle noise. The topographic effects in the interferograms were removed by subtracting the topographic phase simulated using 30-meter resolution C-band SRTM DEM. Fringe patterns over the upland area were used to estimate a best fitting plane to remove the phase caused by orbital error. Adaptive filtering is also applied to further reduce the noise and enhance fringe visibility (*Goldstein and Werner*, 1998). Minimum cost flow method was used to unwrap the interferograms (*Costantini*, 1998).

Table 5-1 List of PALSAR scenes obtained in this study.

Path	Frames	Orbit	Number of Scenes	Time Span
600	7180, 7190	Ascending	26	2006 – 2011
646	0000	Ascending	12	2006 – 2011
645	0000	Ascending	12	2007 – 2011
644	0000, 0010	Ascending	26	2007 – 2011
643	0010, 0020	Ascending	36	2007 – 2011
642	0020	Ascending	14	2006 – 2010
641	0020	Ascending	8	2007 – 2011
640	0020	Ascending	17	2007 – 2011

5.2.2.3 GRACE data

High-resolution GRACE Release 05 (RL05) mascon solution (*Save et al.*, 2016) provided by Center for Space Research (CSR) to obtain TWS changes was used in this

study. The CSR RL05 mascon solutions are generated on a 0.5-degree longitude-latitude grid with 1-degree resolution using GRACE Level-1 observations based on the same standards as CSR RL05 Spherical Harmonics (SH) solutions. It is well known that the SH solutions need filtering and de-striping to reduce random spatial noise and correlated north/south strips in the spatial domain (*Swenson and Wahr*, 2006). These filtering processes will introduce leakage errors that need to be addressed to get a correct signal (*Guo et al.*, 2010; *Landerer and Swenson*, 2012). On the other hand, *Save et al.* (2016) showed that, compared to RL05 SH solutions and other global mascon solutions, the CSR RL05 mascon solutions can provide more accurate mass change estimates without applying any additional filtering or de-striping. These data were downloaded from: http://www.csr.utexas.edu/grace.

5.2.2.4 TRMM data

Precipitation data from TRMM is used in this study in order to explain the inter-annual variations in the wetland storages. TRMM provides monthly precipitation with spatial resolution of 0.25°× 0.25°. *Beighley et al.* (2011) compared different precipitation datasets with the Hillslope River Routing (HRR) model in the Congo Basin, and showed that TRMM provided the best spatial and temporal distributions of the rainfall in the Congo Basin.

5.3 Method

The method used in this study consists of five steps: (1) generating interferograms and selecting interferograms showing most extensive fringes; (2) generating 2-D water depth maps for high-water season over the wetlands by calibrating InSAR-derived $\partial h/\partial t$

measurements with Envisat altimetry-derived h measurements; (3) constructing $d-V$ relationship using the water depth maps from Step 2; (4) generating time series of h in the wetlands using Envisat altimetry, and converting it to time series of maximum water depth (d^t_{max}) in the wetlands, (5) combining the time series of d^t_{max} from Step 4 and $d-V$ relation from Step 3 to estimate time series of absolute water storages over the wetland. The rest of this section will explain how each step is accomplished in detail.

5.3.1 Interferogram Generation and Selection

Interferograms were generated using all available PALSAR images listed in Table 5-1. Figure 5-2 illustrates three mosaics of differential wrapped interferograms generated using SAR images from low and high, low and mid-high, mid-high and high water seasons, respectively (Table 5-2). Each fringe in the interferograms represents a half-wavelength (11.8 cm) deformation along radar's line-of-sight (LOS) direction or about 15.4 cm in the vertical direction. These fringes in our interferograms mostly represent $\partial h/\partial t$ between two SAR acquisition dates. Overall, it can be seen that $\partial h/\partial t$ has the greatest spatial gradients from the distal wetland (region farther from the channel) towards the proximal wetland (region close to the channel). Close-ups of interferogram mosaics in Figure 5-3 support that the fringe direction in the wetland is perpendicular to the flow direction (invisible in the figure; north to south in Figure 5-3 (a-c) and east to west in Figure 5-3 (d-f)) on the mainstem. It shows few fringes in the distal wetland, and dense fringes in the proximal wetland from Figure 5-2(a). It indicates that the gradient of $\partial h/\partial t$ between low and high water seasons is low in the distal wetland but high in the proximal wetland. On the other hand, we observe only dense fringes in the proximal wetland from Figure 5-2(b), which indicates high gradient of $\partial h/\partial t$ in the proximal wetland between low and mid-high water

seasons. On the contrary, only few fringes in the distal wetland can be observed from Figure 5-2(c), which indicates low spatial gradient of $\partial h/\partial t$ in the distal wetland and little spatial gradient of $\partial h/\partial t$ in the proximal wetland between mid-high and high water seasons.

Table 5-2 List of ALOS PALSAR interferometric pairs used to generated InSAR mosaics in Figure 5-2.

Path	Figure 2(a)	Figure 2(b)	Figure 2(c)
600	12/27/2006 – 09/29/2007 (high – low)	09/29/2007 – 12/30/2007 (low – mid)	12/27/2006 – 12/30/2007 (high – mid)
646	12/27/2006 – 09/29/2007 (high – low)	09/29/2007 – 12/30/2007 (low-mid)	12/27/2006 – 12/30/2007 (high – mid)
645	06/12/2007 – 12/13/2007 (low – high)	10/30/2008 – 12/15/2008 (low – mid)	12/15/2008 – 12/13/2007 (mid – high)
644	01/08/2007 – 07/11/2007 (high – low)	01/16/2010 – 07/19/2010 (mid-low)	01/16/2010 – 04/18/2010 (high – -mid)
643	06/24/2007 – 12/25/2007 (low – high)	06/24/2007 – 12/27/2008 (low – mid)	12/25/2007 – 12/27/2008 (high – mid)
642	12/05/2006 – 06/07/2007 (high – low)	06/07/2007 – 12/08/2007 (low – mid)	12/05/2006 – 12/08/2007 (high – mid)
641	07/06/2007 – 01/06/2008 (low – high)	05/29/2010 – 08/29/2010 (mid – low)	05/29/2010 – 01/06/2008 (mid – high)
640	09/19/2007 – 12/20/2007 (low – high)	09/19/2007 – 05/12/2010 (low – mid)	05/12/2010 – 12/20/2007 (mid – high)

Next, the interferogram mosaic in Figure 5-2(a) was selected which shows the most extensive and dense fringes for further process because it shows $\partial h/\partial t$ gradient over both proximal and distal wetlands. Specifically, eight regions that have dense fringes across the wetland, and marked them with (A − H) were identified as target wetlands. Fringe visible

areas were delineated with the geocoded wrapped interferograms using ArcGIS software, and the wetland lengths along the Congo mainstem and areas were measured for each target wetland (Table 5-3).

Table 5-3 Details for each target wetland identified in Figure 5-2(a).

Wetland	Area (km^2)	Length along Congo mainstem (km)	PALSAR Tracks	Envisat Passes
A	208.74	39.2	646, 600	429, 930
B	3418.2	132	646, 600	429, 930
C	1706.8	81.14	644	343, 386
D	419.01	39.05	643	343, 386
E	132.72	27.18	641	257, 300
F	687.39	73.4	641	257, 300
G	474.96	75.85	640	300, 715
H	725.26	77.22	640	300, 715

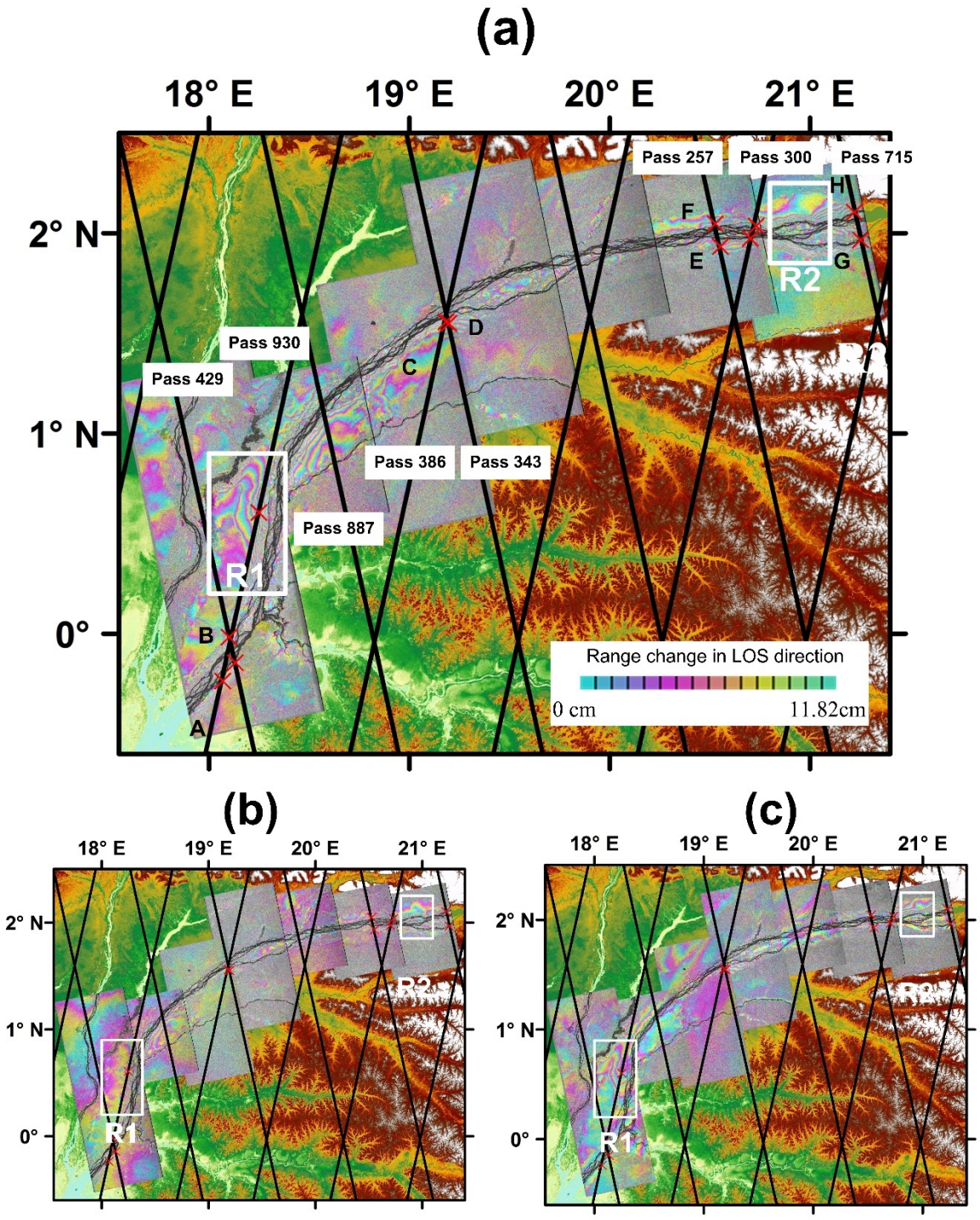

Figure 5-2 Mosaic of PALSAR interferograms from low and high (a), low and mid-high (b), mid-high and high (c) water seasons. Regions marked as (A – H), are our study areas. Red "×"s represent "virtual station".

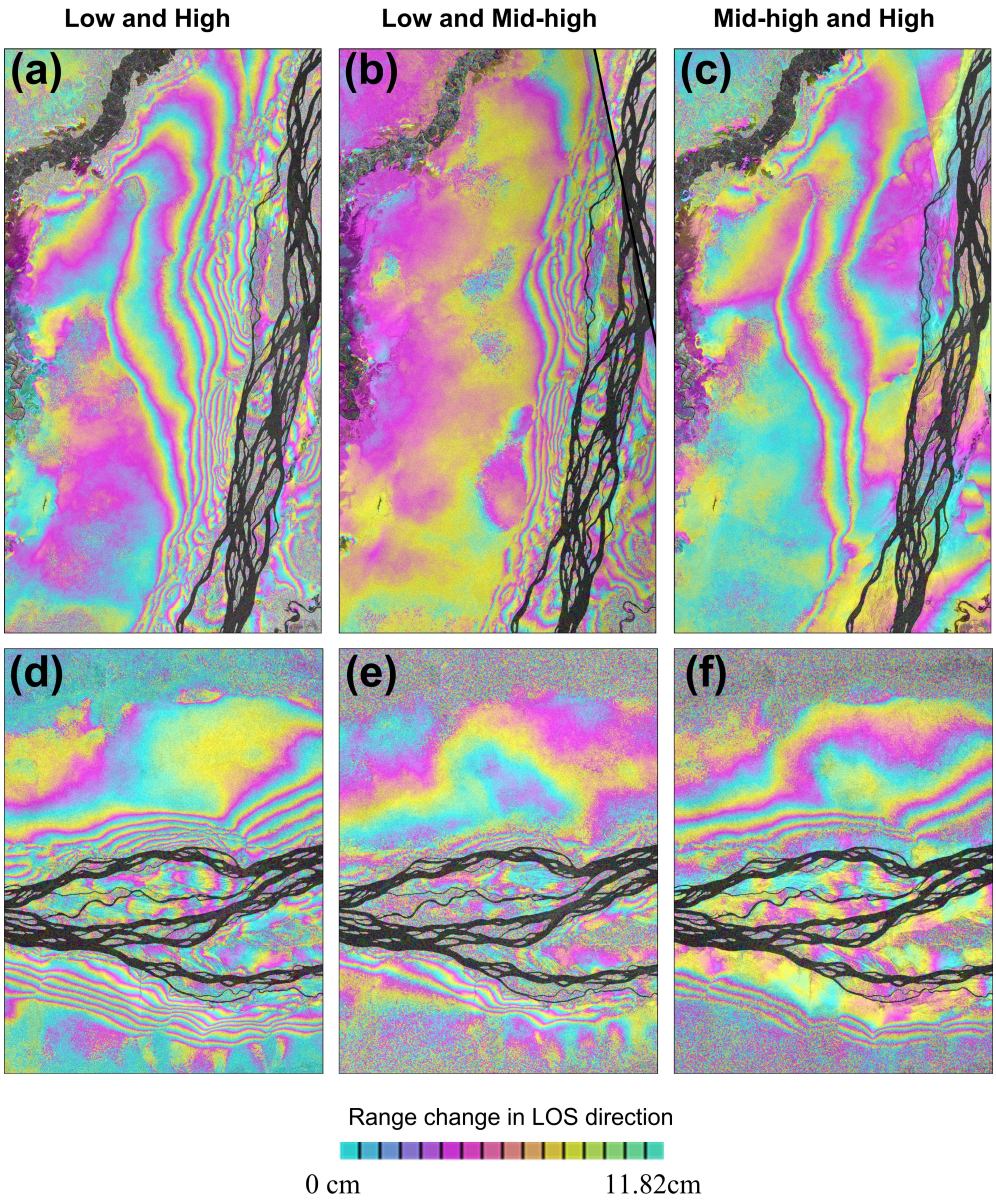

Figure 5-3 Close-ups of interferograms in Figure 5-2. (a)-(c) are plots of boxes R1 and (d)-(f) are plots of boxes R2.

5.3.2 Water Depth Maps from Calibration of InSAR-derived $\partial h/\partial t$

The interferograms shown in Figure 5-2(a) were unwrapped using the minimum cost flow method (*Costantini*, 1998). However, since the interferograms can provide only a spatially relative gradient of $\partial h/\partial t$ (*Alsdorf et al.*, 2007a; *Kim et al.*, 2009; *Lu et al.*, 2009), an offset (i.e., a vertical reference) is needed to convert it to absolute water level

changes. This offset is calculated by comparing InSAR-derived $\partial h/\partial t$ gradient with Envisat altimetry-derived $\partial h/\partial t$, following the method in (*Kim et al.*, 2009), which is explained next.

Since the water level from altimetry (h_{alt}) has a fixed reference (i.e., reference ellipsoid or geoid), water level change from altimetry ($\partial h_{alt}/\partial t$) can be considered as the absolute water level change. The difference between $\partial h_{alt}/\partial t$ and the InSAR-derived $\partial h_{InSAR}/\partial t$ is the offset to be estimated, such as

$$\partial h_{alt}/\partial t = \partial h_{InSAR}/\partial t + offset. \quad (5\text{-}1)$$

To perform the calibration (i.e., conversion to absolute water level change) of $\partial h_{InSAR}/\partial t$ measurements, the Envisat altimetry measurements were first temporally interpolated with respect to the SAR acquisition dates (Figure 5-4 left panels) except the low water profiles from Envisat pass 386 (Figure 5-4 b1 and c1). This is because low water level profiles from Envisat track 386 in 2007 were all noisy. Another less noisy (or smooth) low water level profile obtained on 03/07/2005 (cycle 35) was used as the low water level profile for Envisat pass 386 instead. This replacement should have little impact because the water level in the Congo wetland has distinctive seasonal variations and the water level varies little during low water seasons.

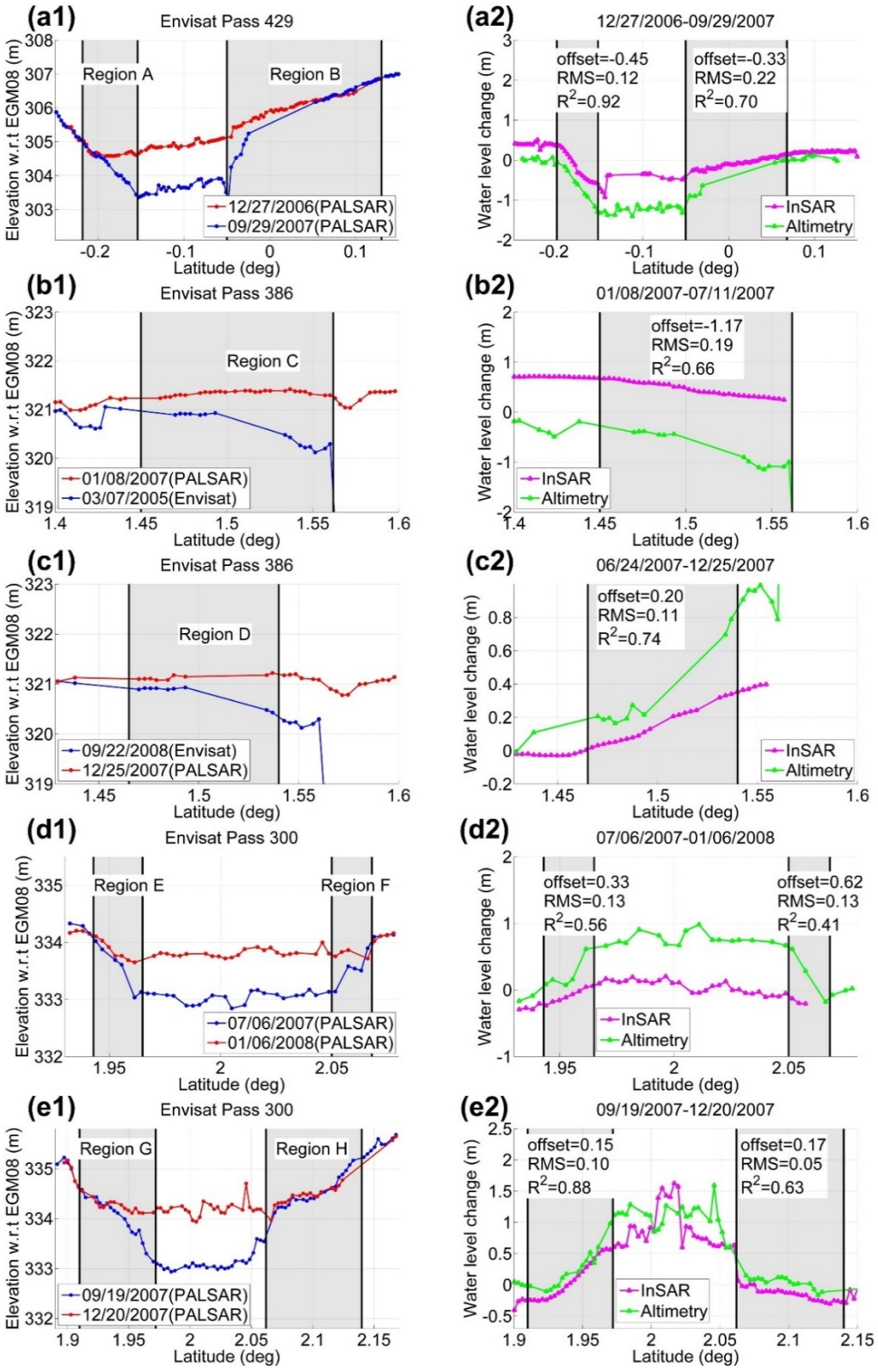

Figure 5-4 Left panels represent interpolated Envisat altimetry profiles. Right panels represent comparison between altimetry-derived and InSAR-derived $\partial h/\partial t$. Locations of each region are referred to Figure 5-2.

The $\partial h/\partial t$ from InSAR and Envisat altimetry are compared, as shown in Figure 5-4 (right panels). Both $\partial h_{alt}/\partial t$ and $\partial h_{InSAR}/\partial t$ show very similar spatial variations of water level changes in the wetlands. The R^2 values between them vary from 0.41 to 0.92 and the root-mean-squared (RMS) differences vary from 0.1 m to 0.22 m. The R^2 values between $\partial h_{InSAR}/\partial t$ and $\partial h_{alt}/\partial t$ are lower in regions E and F, with values of 0.56 and 0.41, respectively. This is because the interferograms over regions E and F have fewer fringes that result in a smaller number of valid measurements for comparison.

By adding the estimated offsets shown in Figure 5-4 to $\partial h_{InSAR}/\partial t$, absolute water level change maps are then obtained. Among the interferograms from 7 adjacent paths shown in Figure 5-2(a), this vertical reference was not estimated or interferograms from PALSAR paths 645 and 642. This is because Envisat altimetry track 887 intersecting with PALSAR path 645 did not perform well in the southern wetland. Therefore, the calibration could not be performed. The interferograms from path 642 were also excluded because there are few fringes which indicates little water level change in the wetland. Overall, the interferograms from paths 645 and 642 shown in Figure 5-2(a) were not used for further analysis.

Since the interferograms were generated using two SAR images obtained on low and high water seasons, the absolute water level change maps should be close to water depth maps for the high water season based on the assumption that little water is on the wetland during low water season. A similar assumption has been made in *Lee et al.* (2015). InSAR-derived $\partial h/\partial t$ maps represent water level change from acquisition dates of master images to slave images (Table 5-2). The interferograms generated from high water to low water seasons (PALSAR paths 600, 646 and 644) (Table 5-2), which represent decreasing

water levels in time, were converted into water depth maps by multiplying −1. Finally, eight water depth maps were obtained over eight target wetlands as shown in Figure 5-5(left panels).

5.3.3 Wetland Geomorphology and $d - V$ Relation using Water Depth Maps

Figure 5-6 schematically illustrates the wetland geomorphology and the impact of water level change to water storage changes. The wetland was modeled as a floodway elongated along the river with slope from the view of cross-section. The length of the wetland is denoted using L_f.The cross-sectional slope of the wetland is described using the relative elevation of y with respect to the elevation of the wetland floor ($h_{bathymetry}$). y is supposed to increase with an increase of distance r from the river. It is assumed that water level is almost flat in the wetland cross-section (assumption 1) and water surface slope in the wetland along the river flow direction has little temporal variation (assumption 2). Assumption 1 is valid for the Congo River wetland and confirmed by looking at the high water level profiles from Envisat altimetry in Figure 5-4 left panels except Figure 5-4(a1). This is because Envisat pass 429 in Figure 5-4(a1) does not fly over the wetland cross-sectional direction but captures upstream-downstream water surface slope. Assumption 2 is also almost valid because water surface slope in the Congo River varies little in time (*O'Loughlin et al.*, 2016). In addition, there are very few fringes in the proximal wetland from InSAR mosaic in Figure 5-2(c) which indicates $\partial h/\partial t$ has little spatial variations in the proximal wetland between mid-high and high water seasons.

The $d - V$ relationships for each wetland are constructed using each of the eight water depth maps from Section 5.3.2. First of all, histograms of water depths can be generated

by counting the number of pixels within each water depth bin (Figure 5-5 middle panels). Then, the volume of water in the wetland at time t_1 (i.e., the high water dates in Table 5-2) can be estimated from the histogram as:

$$V(d_{max}^{t_1}) = \sum_{d^{t_1}=0}^{d^{t_1}=d_{max}^{t_1}} d^{t_1} * A^{t_1}(d^{t_1}), \tag{5-2}$$

where $V(d_{max}^{t_1})$ is the total water volume of that target wetland with maximum water depth $d_{max}^{t_1}$ at time t_1; d^{t_1} is the water depth varying from 0 to $d_{max}^{t_1}$; $A^{t_1}(d^{t_1})$ is the inundated area that varies with the water depth d^{t_1}, and it can be computed by multiplying the number of pixels with depth d^{t_1} from the histogram in Figure 5-5 (middle panels) with the resolution of the interferogram or the water depth map (~ 30 m).

Considering water level is decreased by Δh at t_2, following the schematic plot in Figure 5-6(b), the maximum water depth will be

$$d_{max}^{t_2} = d_{max}^{t_1} - \Delta h, \tag{5-3}$$

and the water depths over all the wetland pixels d^{t_2} can be written as

$$\begin{cases} d^{t_2} = d^{t_1} - \Delta h, & where\ d^{t_1} \geq \Delta h \\ d^{t_2} = 0, & where\ d^{t_1} < \Delta h. \end{cases} \tag{5-4}$$

This relationship can be expanded for the inundated area $A^{t_2}(d^{t_2})$ such as:

$$\begin{cases} A^{t_2}(d^{t_2}) = A^{t_1}(d^{t_1}), & where\ d^{t_1} \geq \Delta h \\ A^{t_2}(d^{t_2}) = 0, & where\ d^{t_1} < \Delta h. \end{cases} \tag{5-5}$$

Using Equation (5-5), the total volume of water with maximum water depth $d_{max}^{t_2}$ can be estimated by

$$V\left(d_{max}^{t_2}\right) = \sum_{d^{t_2}=0}^{d^{t_2}=d_{max}^{t_2}} d^{t_2} * A^{t_2}(d^{t_2}) = \sum_{d^{t_1}=\Delta \mathrm{h}}^{d^{t_1}=d_{max}^{t_1}} (d^{t_1} - \Delta h) * A^{t_1}(d^{t_1}). \quad (5\text{-}6)$$

Therefore, with Δh varying from 0 to $d_{max}^{t_1}$, the volume of water can be estimated for cases with different maximum water depths from $d_{max}^{t_1}$ to 0 using Equation (5-6). In other words, if a water depth map of d^{t_1} with the maximum water depth $d_{max}^{t_1}$ is obtained, the water volumes for cases with different maximum water depths smaller than $d_{max}^{t_1}$ can also be obtained. An increment of 1 cm for Δh is arbitrarily chosen in this study. The $d - V$ relation is then finally constructed, as shown in the right panels of Figure 5-5. It should be noted that this $d - V$ relations for each region are established with respect to different maximum water depths that are smaller than the maximum water depths obtained from the left panels of Figure 5-5 ($d_{max}^{t} < d_{max}^{t1}$).

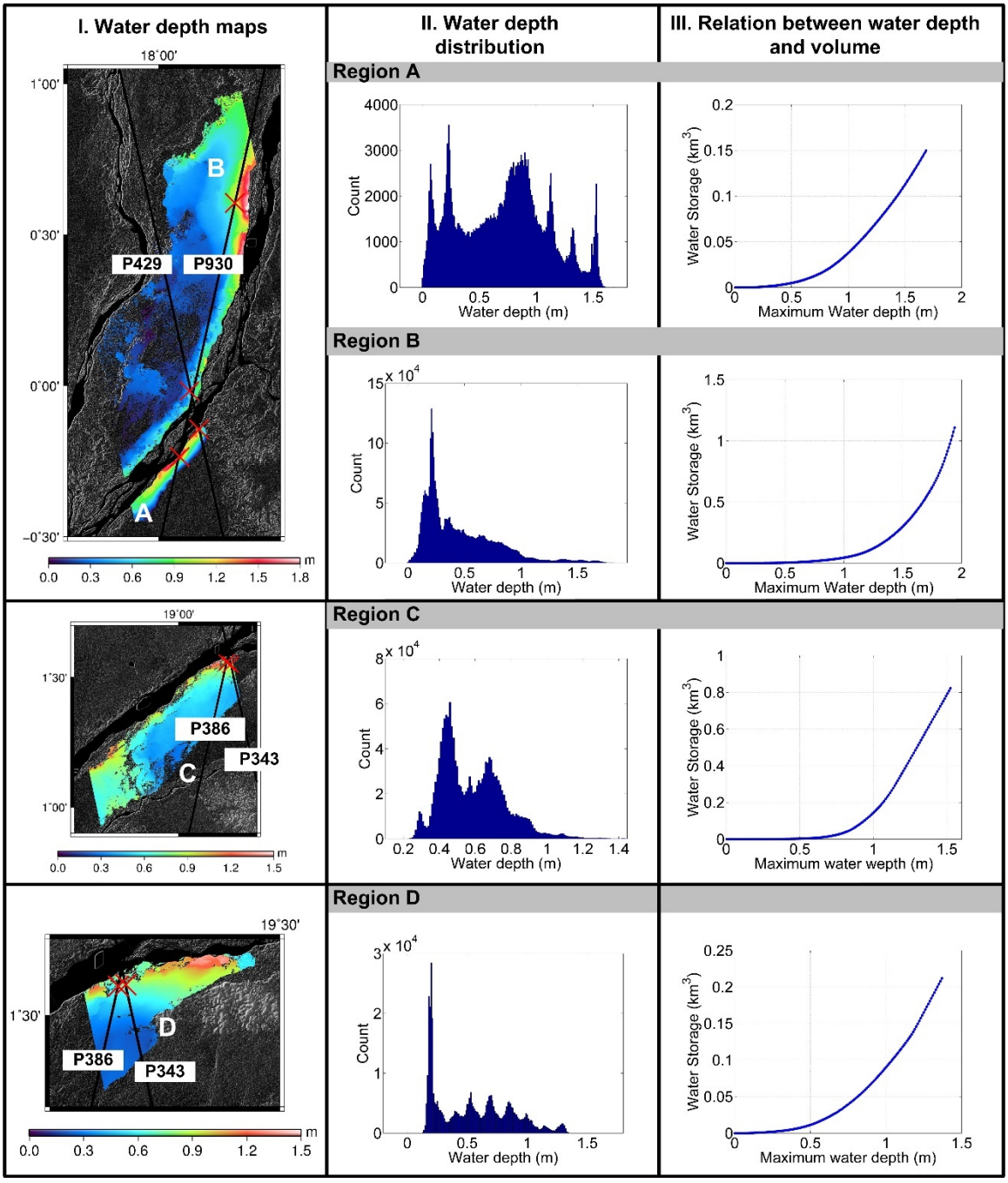
I. Water depth maps
II. Water depth distribution
III. Relation between water depth and volume
Region A
Region B
Region C
Region D
18°00'
1°00'
0°30'
0°00'
-0°30'
19°00'
1°30'
19°30'
P429
P930
P386
P343
A
B
C
D
m
0.0 0.3 0.6 0.9 1.2 1.5 1.8
Count
Water depth (m)
Water Storage (km3)
Maximum Water depth (m)
Maximum water wepth (m)
Maximum water depth (m)
x 10^4

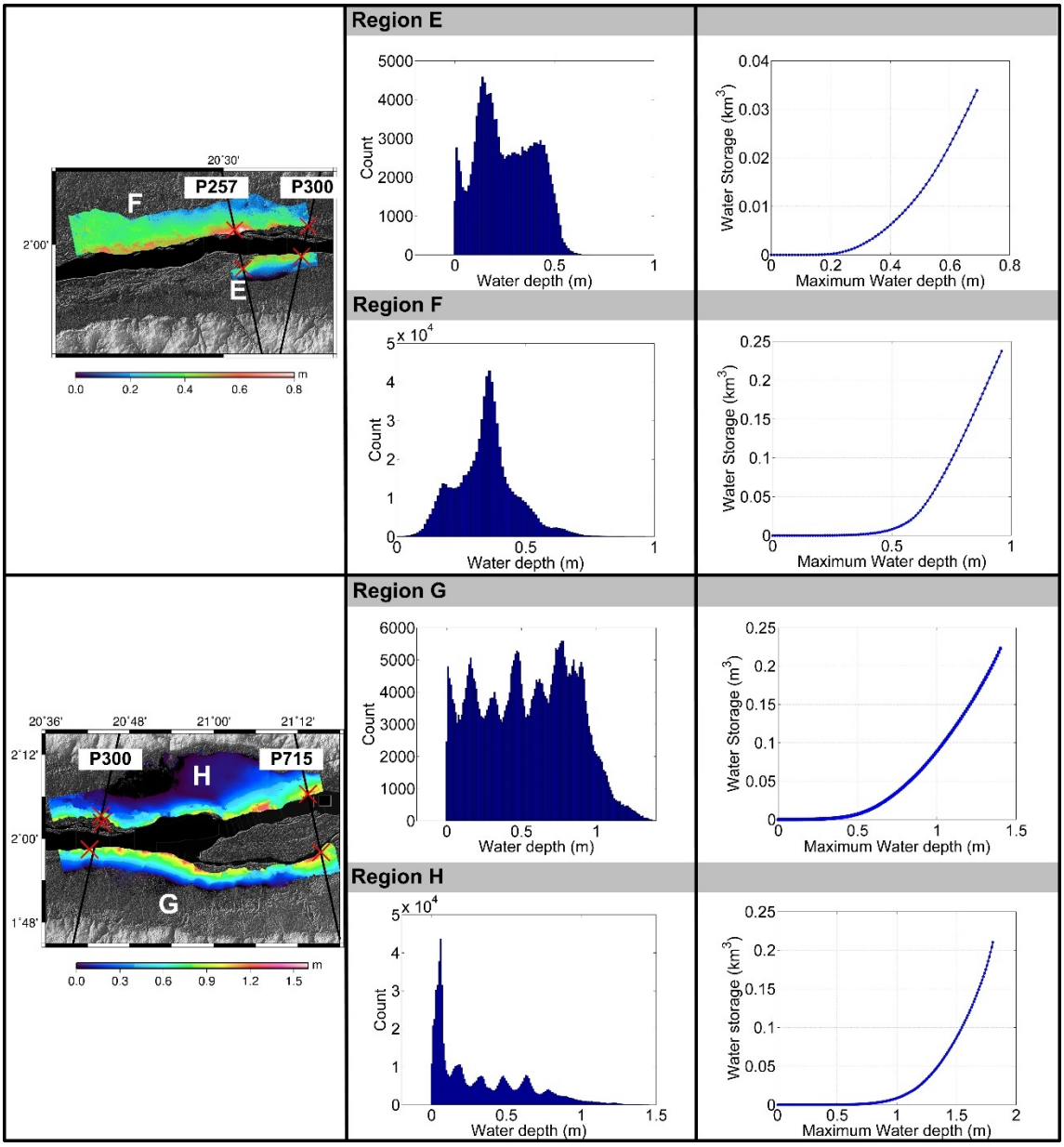

Figure 5-5 (Left) Water depth maps from InSAR and altimetry. (Middle) Distribution of water depths from water depth maps on the left panels. (Right) Relationship between maximum water depth (d_t^{max}) and absolute water volume (V).

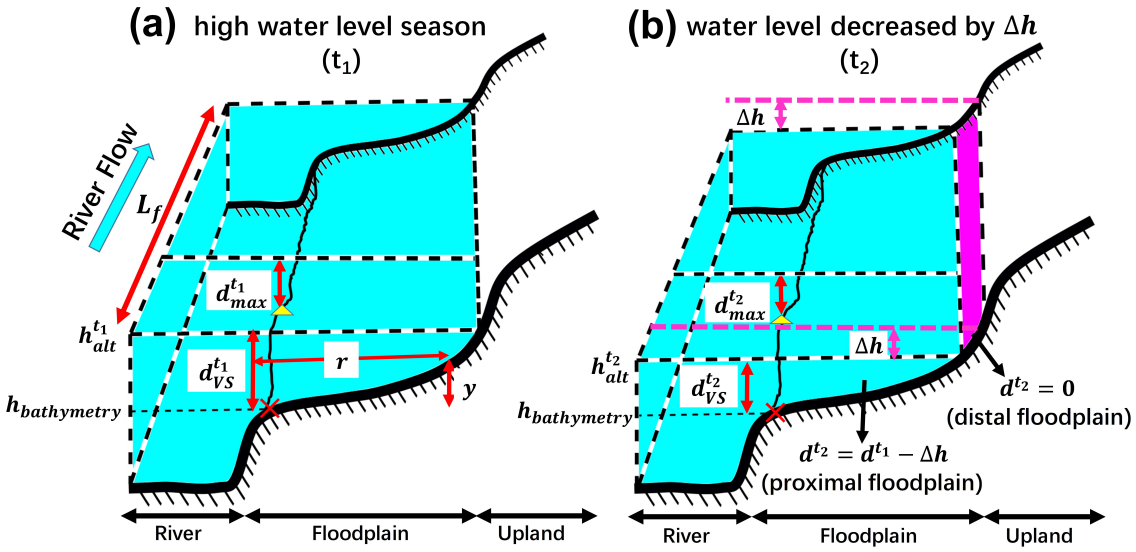

Figure 5-6 Schematic plot of wetland geomorphology and water surface at t_1 (a) and t_2 (b) with maximum water depth location (yellow triangles) and virtual station (red crosses). Magenta region in (b) represents region without water at t_2.

5.3.4 Time Series of Maximum Water Depths

In this section, the derivation for the time series of the maximum water depths (d_{max}^t) is described which will be used with the $d - V$ relationship derived in Section 5.3.3 in order to generate the time series of absolute water volumes.

From the left panels of Figure 5-5, each identified wetlands A – H has two overflying Envisat tracks. Over the intersections of the wetlands and Envisat tracks, so-called "virtual stations" (red "×"s in Figure 5-2) are defined. As a result, 12 virtual stations (Figure 5-2) were establised. The name of each virtual station is defined using the wetland region and its altimetry pass number. For example, virtual station A_429 represents the virtual station at wetland A with Envisat pass 429. It should be noted that some of the wetlands share common virtual stations. This is because some Envisat ground tracks are located at the intersection of two adjacent PALSAR images. For example, Envisat tracks 343 and 386 are located at the intersection of wetland Regions C and D, from which virtual

stations C(D)_386 and C(D)_343 are obtained. Similarly, Envisat track 300 is located at the intersection of PALSAR paths 641 and 640, from which virtual stations E(G)_300 and F(H)_300 are obtained. Consequently, there are 12 virtual stations from 16 intersections between the Envisat tracks and the target wetlands.

Over each virtual station, time series of water level (h_{alt}^{t}) were generated using Envisat altimetry measurements (Figure 5-7 left panels). Then, a smooth low water level profile is used as the vertical reference for each virtual station, following the same method as (*Lee et al.*, 2015). The elevations obtained from these low water level profiles are considered as the bathymetry elevations ($h_{bathymetry}$) of each virtual station (horizontal lines in left panels of Figure 5-7). Table 5-4 summarizes the selected low water level altimetry profiles and calculated $h_{bathymetry}$ for each virtual station. Next, time series of water depths (d_{VS}^{t}) were generated at each virtual station by subtracting $h_{bathymetry}$ from h_{alt}^{t}:

$$d_{VS}^{t} = h_{alt}^{t} - h_{bathymetry}. \tag{5-7}$$

It should be again noted that the $d - V$ relationship obtained in Section 5.3.3 is with respect to the maximum water depths in each wetland. However, an Envisat altimetry track does not always fly over the region with the maximum water depth. In order to obtain the time series of maximum water depths (d_{max}^{t}), a correction term $\Delta d_{conversion}$ was computed which is the difference between d_{max}^{t1} and the water depth interpolated at the virtual station location using Figure 5-5 (left panels). The calculated $\Delta d_{conversion}$ for each virtual station is summarized in Table 5-4. Finally, after adding $\Delta d_{conversion}$ to d_{VS}^{t} for each virtual

station, time series of d_{max}^{t} were obtained using measurements from two virtual stations for each wetland region (Figure 5 right panels) such as

$$d_{max}^{t} = d_{VS}^{t} + \Delta d_{conversion}. \quad (5\text{-}8)$$

The $\Delta d_{conversion}$ term addresses the spatial heterogeneity of water depth and linked the water depth at virtual stations and maximum water depth. One of the benefit of using two virtual stations to obtain time series of d_{max}^{t} is higher temporal sampling of d_{max}^{t} for each region. The good agreement of d_{max}^{t} from two virtual stations indicates the effect of spatial homogeneity of $\partial h/\partial t$ at the two virtual stations as suggested by Equation (5-5) and Figure 5-6.

Table 5-4 List of virtual stations over each target wetland identified in Figure 5-2(a).

Region	Virtual Stations	Location (longitude, latitude)	$h_{bathymetry}$ (m)	Envisat cycles for $h_{bathymetry}$	$d_{max}^{t_1}$ (m)	$d_{VS}^{t_1}$ (m)	$\Delta d_{correctio}$ (m)
A	A_429	(18.132, -0.144)	303.09	47	1.68	1.38	0.30
	A_930	(18.069, -0.235)	302.40	90		1.53	0.15
B	B_429	(18.101, -0.018)	304.5	30	1.95	0.82	1.13
	B_930	(18.249, 0.600)	309.66	34		0.95	1.00
C	C_386	(19.184, 1.557)	320.25	58	1.52	0.90	0.62
	C_343	(19.19, 1.55)	320.18	21		0.92	0.6
D	D_386	(19.184, 1.557)	320.25	58	1.41	0.67	0.74
	D_343	(19.19, 1.55)	320.18	21		0.65	0.76
E	E_300	(20.705 1.974)	332.83	37	0.71	0.46	0.25
	E_257	(20.554 1.934)	330.97	69		0.43	0.28
F	F_300	(20.732 2.055)	333.20	77	1.06	0.72	0.34
	F_257	(20.53 2.04)	331.62	49		0.80	0.26
G	G_300	(20.705, 1.974)	332.83	37	1.49	1.07	0.42
	G_715	(21.257 1.967)	338.10	31		0.84	0.65
H	H_300	(20.732 2.055)	333.20	77	1.8	0.82	0.98
	H_715	(21.224 2.1058)	338.14	83		1.15	0.65

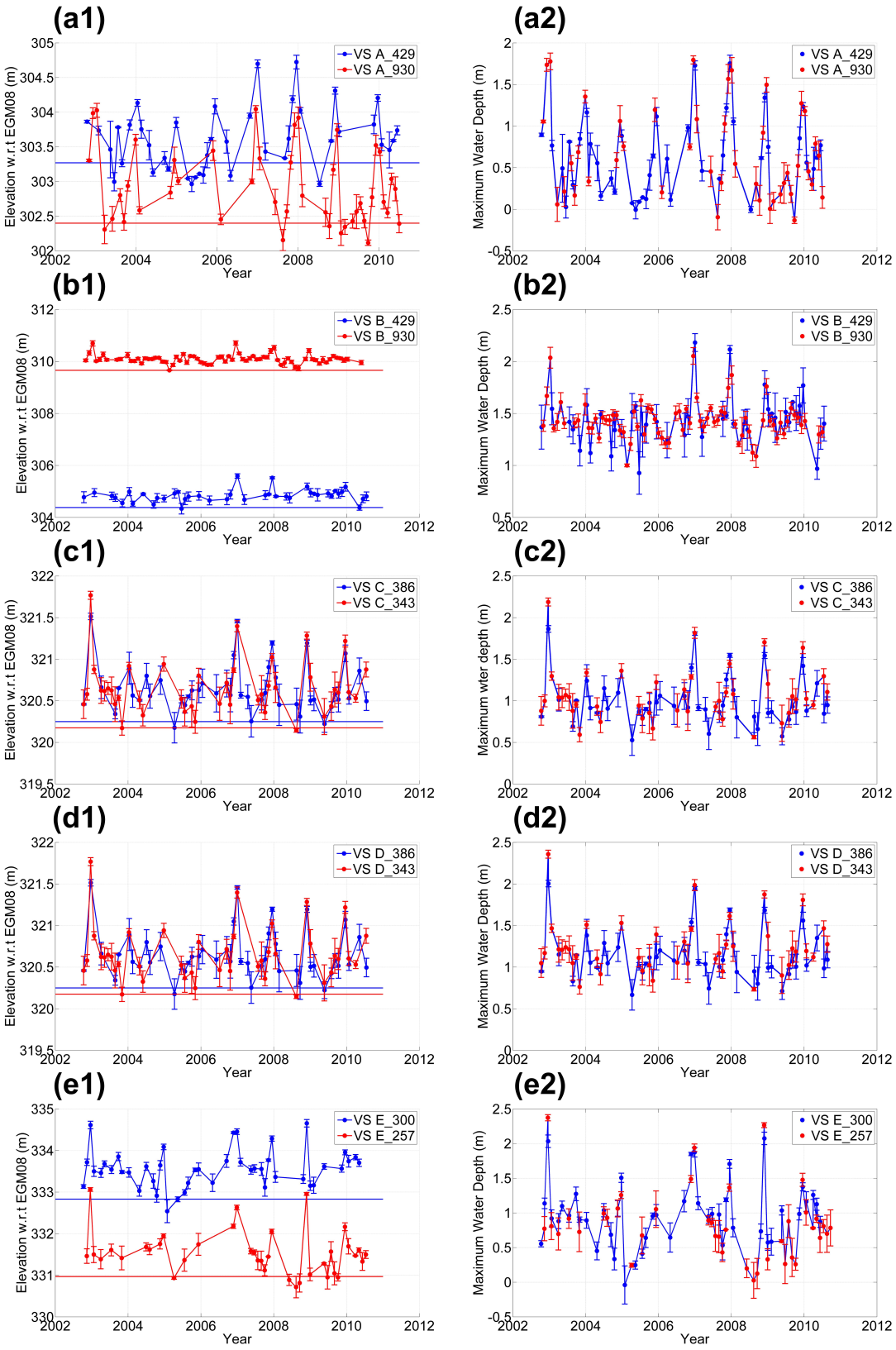
(a1)
VS A_429
VS A_930
Elevation w.r.t EGM08 (m)
Year
(a2)
VS A_429
VS A_930
Maximum Water Depth (m)
Year
(b1)
VS B_429
VS B_930
Elevation w.r.t EGM08 (m)
Year
(b2)
VS B_429
VS B_930
Maximum Water Depth (m)
Year
(c1)
VS C_386
VS C_343
Elevation w.r.t EGM08 (m)
Year
(c2)
VS C_386
VS C_343
Maximum wter depth (m)
Year
(d1)
VS D_386
VS D_343
Elevation w.r.t EGM08 (m)
Year
(d2)
VS D_386
VS D_343
Maximum Water Depth (m)
Year
(e1)
VS E_300
VS E_257
Elevation w.r.t EGM08 (m)
Year
(e2)
VS E_300
VS E_257
Maximum Water Depth (m)
Year

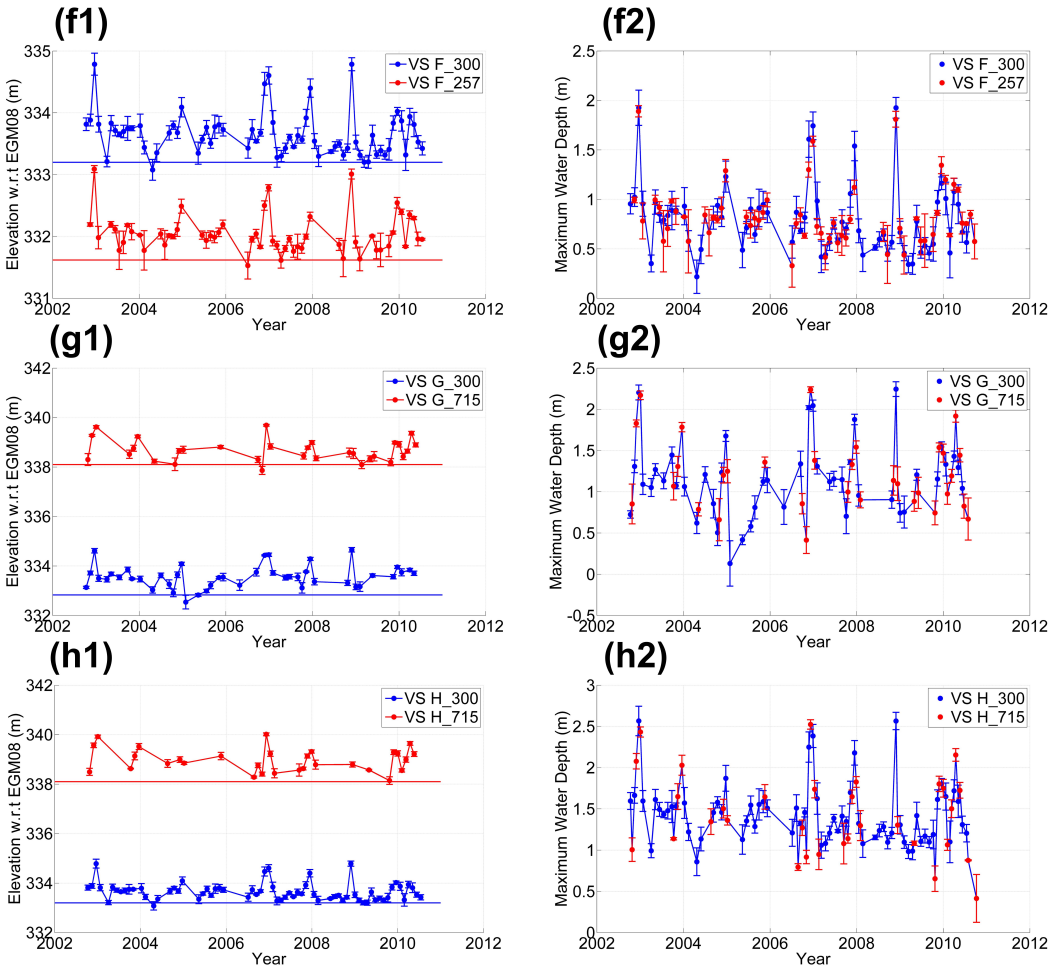

Figure 5-7 (Left) Time series of water levels (h_{alt}) derived from Envisat altimetry data over the 12 virtual stations. Locations of virtual stations are referred to Figure 5-2(a). (Right) Time series of d_t^{max} over each wetland.

5.3.5 Time Series of Absolute Water Volumes

Using the $d - V$ relationship from Section 5.3.3 and the time series of d_{max}^t from Section 5.3.4, time series of absolute water volumes were generated for each wetland region (Figure 5-8). The x-axis limit of $d - V$ shown in Figure 4 (right panels) represents the maximum water depths obtained from the water depth maps, i.e., $d_{max}^{t_1}$. If d_{max}^t from Equation (5-8) is smaller than $d_{max}^{t_1}$, the water storage is directly obtained from the $d - V$ curve. Otherwise, the water storage is computed by linearly extrapolating the $d - V$ curve.

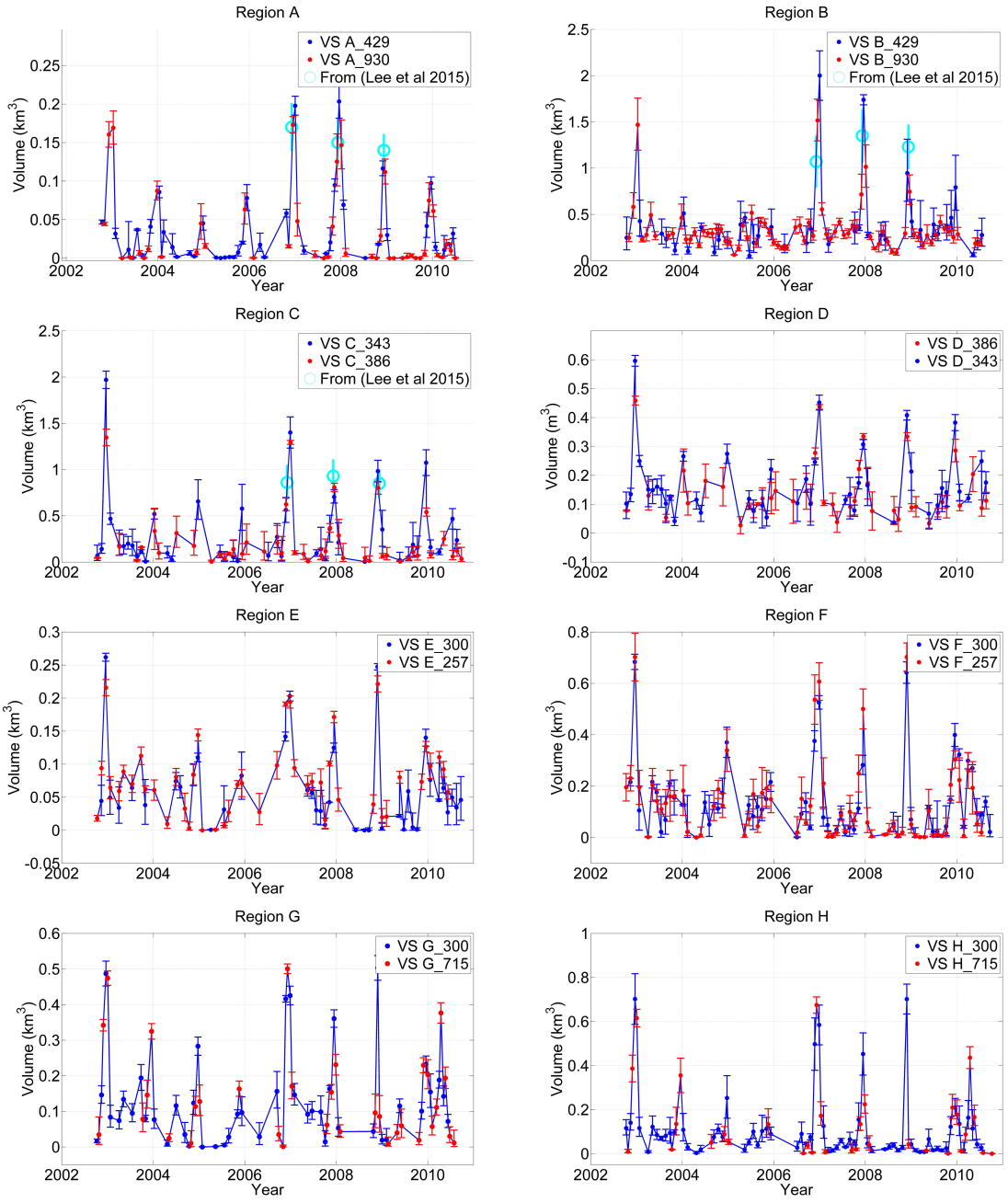

Figure 5-8 Time series of absolute water volumes over the eight wetlands.

5.4 Results

5.4.1 Modelling of the $d - V$ Relationship

The $d - V$ relationship in the wetland reveals how the wetlands store water, which is usually characterized by wetland bathymetry. Modeling of the $d - V$ relationship

contributes to the understanding of the shape of the bathymetry and thus the characteristics of water storage in the wetland.

Here, the wetland is modelled as in Figure 5-6 whose cross-sectional slope can be characterized with a power function proposed in *Hayashi and Van Der Kamp* (2002):

$$y/y_0 = (r/r_0)^p, \tag{5-9}$$

where y is the relative elevation of the wetland floor with respect to the cross-sectional lowest wetland bathymetry at a distance r from the river; y_0 is the unit elevation; r_0 is the distance to the river corresponding to y_0; p is the shape coefficient. Shapes of slope profiles with different p values are shown in Figure 5-9.

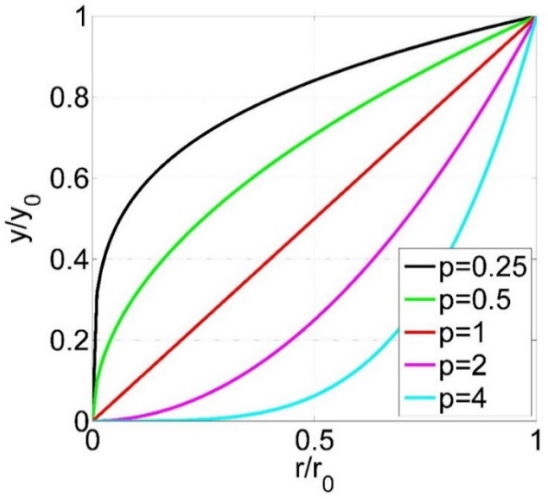

Figure 5-9 Slope profiles of wetland with $y/y_0 = (r/r_0)^p$; $p > 1$ indicates a concave slope; $p > 1$ indicates a convex slope; $p = 1$ indicates a flat slope.

Since the algorithm in *Hayashi and Van Der Kamp* (2002) has been derived for "pothole" wetlands which have different geometric shape from the wetlands in this study, Equation (5-10) was derived for wetland using the principle proposed in *Hayashi and Van Der Kamp* (2002). The derivation of Equation (5-10) is given in Appendix I.

$$V(d_{max}^t) = L_f \cdot \frac{r_0}{(1+\frac{1}{p})} \cdot \frac{(d_{max}^t)^{1+1/p}}{d_0^{1/p}}, \quad (5\text{-}10)$$

where $V(d_{max}^t)$ is water volume with maximum water depth d_{max}^t, L_f is the wetland length along the river (Table 5-3), and r_0 is a scaling constant which is equal to the width of inundated wetland when $d_{max}^t = d_0$.

Equation (5-9) was then used to determine the best-fit values of p and r_0 for each wetland using the least-squares method (Figure 5-10). From Figure 5-10, Equation (5-10) can be used to adequately represent the $d - V$ relationship obtained in Section 5.3.3. Meanwhile, all the p values are smaller than 1, which suggests that the shape of the wetland bathymetry is mostly convex. This shape coefficient derived over the wetlands in Congo is different from that for the potholes or lakes, which have p values higher than 1, representing a concave shape (*Hayashi and Van Der Kamp*, 2000).

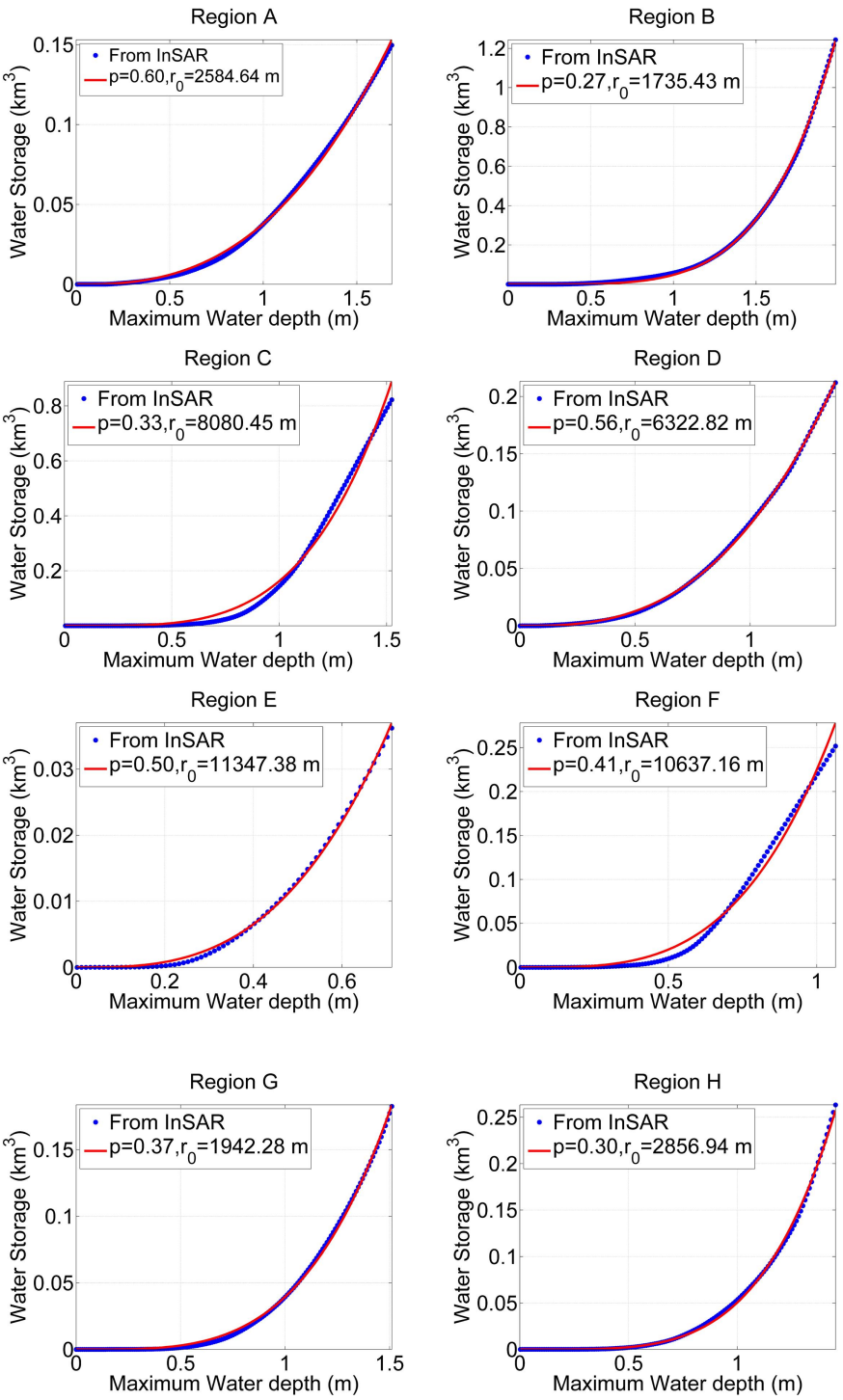

Figure 5-10 p and r_0 values for each wetland.

5.4.2 Quantitative Validations of Wetland Water Storages

The estimated absolute water volumes from Section 5.3.5 were compared with results from *Lee et al.* (2015) who estimated absolute water storages from the water depth maps generated using backscattering coefficients from PALSAR ScanSAR, water level changes from Envisat altimetry, and VCF from MODIS. The absolute water storages were calculated using the water depth maps from *Lee et al.* (2015) (by summing the water depths multiplied by the ScanSAR resolution) over the three common wetlands (A, B, and C). It is noted that *Lee et al.* (2015) were able to generate the water depth maps only for the dates of ScanSAR acquisitions on 12/5/2006, 12/8/2007 and 12/10/2008 (for more details, readers are referred to *Lee et al.* (2015)). For region A, the estimates of the absolute water volumes on 12/16/2006, 12/01/2007, and 12/02/2008 (Envisat altimetry dates which are closest to the ScanSAR acquisition dates of *Lee et al.* (2015)) are 0.17 ± 0.01 km^3, 0.13 ± 0.03 km^3, and 0.12 ± 0.01 km^3, respectively, which agree with the estimates from *Lee et al.* (2015) with differences smaller than 0.02 km^3 (Table 5-5). The uncertainties of water storages (σ_V) are calculated by an error propagation of d_{max}^t through the $d - V$ relationship. The uncertainties of d_{max}^t ($\sigma_{d_{max}^t}$) is assumed to be equivalent to the uncertainties of h_{alt} ($\sigma_{h_{alt}}$) which is calculated from the high-rate Envisat measurements as illustrated with error bars in Figure 5-7. It should be noted that the error propagation of $\sigma_{d_{max}^t}$ through the nonlinear $d - V$ relationship results in different lower and upper lengths of the error bars which have been used in the time series of absolute water volumes in Figure 5-8. The upper error bar lengths are slightly larger and described as the uncertainties of water storages, hereinafter. Consequently, for region B, it is estimated to be 1.51 ± 0.23 km^3, 0.72 ± 0.22 km^3 and 0.95 ± 0.37 km^3 for altimetry dates of 12/16/2006, 12/01/2007,

and 12/02/2008, respectively, with differences of 0.44 km^3, 0.53 km^3 and 0.28 km^3 from the estimates from *Lee et al.* (2015). The difference for region B in December of 2007 up to 0.53 km^3 could be due to timing differences between our estimates and estimates from *Lee et al.* (2015). For region C, absolute water storages are estimated to be 0.62 ± 0.07 km^3, 0.70 ± 0.08 km^3 and 0.8 ± 0.07 km^3 for altimetry dates of 11/27/2006, 12/15/2007, and 12/01/2008, respectively, with differences of 0.18 km^3, 0.23 km^3 and 0.05 km^3 from the estimates from *Lee et al.* (2015). Overall, estimation of absolute water volumes over regions A, B, and C in this study agree well with the estimates from *Lee et al.* (2015), with most of the nine values in Table 5-5 falling within the overlapping estimated uncertainty of the two methods.

Table 5-5 Comparisons of water storages from $d - V$ relation and from water depth maps in *Lee et al.* (2015).

	From $d - V$ relation		From *Lee et al.* (2015)	
Region	Date	Volume (km^3)	Date	Volume (km^3)
A	12/16/2006 (VS A_930)	0.17 ± 0.01	12/5/2006	0.17 ± 0.03
	12/01/2007 (VS A_930)	0.13 ± 0.03	12/8/2007	0.15 ± 0.30
	12/02/2008 (VS A_429)	0.12 ± 0.01	12/10/2008	0.14 ± 0.02
B	12/16/2006 (VS B_930)	1.51 ± 0.23	12/5/2006	1.07 ± 0.27
	12/01/2007 (VS B_930)	0.72 ± 0.22	12/8/2007	1.35 ± 0.28
	12/02/2008 (VS B_429)	0.95 ± 0.37	12/10/2008	1.23 ± 0.23
C	11/27/2006 (VS C_386)	0.62 ± 0.07	12/5/2006	0.86 ± 0.18
	12/15/2007 (VS C_343)	0.70 ± 0.08	12/8/2007	0.93 ± 0.17
	12/01/2008 (VS C_386)	0.80 ± 0.07	12/10/2008	0.85 ± 0.14

5.4.3 Evaluation of Wetland Water Storages with GRACE and TRMM

In this section, a qualitative comparison between absolute wetland water storages with TWS anomalies from GRACE data and precipitation anomalies from TRMM data was performed. Because of differences between the spatial resolutions of GRACE and TRMM and the size of our target wetlands, three aggregations were created by combining the water storages from adjacent wetlands together. The three aggregations are (i) A and B, (ii) C and D, and (iii) E, F, G, and H, respectively. Then, the CSR mascon grids which cover each of the three aggregated regions were used to calculate average TWS anomalies for each aggregated region. Similarly, the precipitation anomalies from TRMM data over each aggregated region were also selected and averaged. The wetland water storages, TWS anomalies from GRACE, and precipitation anomalies from TRMM for the period of 2002 – 2011 are illustrated in Figure 5-11(left panels). Our wetland water storages and the GRACE TWS anomalies show distinctive seasonal variations, and their timing agrees reasonably well. The amplitude difference between the TWS anomalies and wetland water storages can be explained by the fact that the GRACE TWS has contributions from water storages in the river channel, soil moisture, and groundwater as well as the wetland. In addition, inter annual variations in both of them are observed– relatively wet years in 2002 and 2007 while relatively dry years from 2003 to 2006. By summing up the water storages during peak seasons over all the studied wetlands, the mean annual amplitude over the entire studied wetlands (~7,777 km^2) is 3.98 ± 0.59 km^3. The maximum wetland water storage is observed in year 2002 with a volume of 6.3 ± 0.68 km^3 and minimum volume of 2.2 ± 0.61 km^3 in the dry year of 2005. In addition, the decreases in water storages are well correlated with the decreases in precipitation during the same period over all of the regions

(i) – (iii). In particular, region (i) (or regions A and B) suffered from the most significant water storage decreases compared to other regions. This can be explained by its more rapid decrease in precipitation (0.4 m to 0 m in peaks from 2003 to 2006) than the precipitation decrease over other regions (ii) and (iii) (0.2 m to 0.1 m in peaks from 2003 to 2006).

The monthly mean values of wetland water storage, TWS anomalies, and precipitation anomalies were also generated and compared. The maximum water storage in the wetland is observed in December which is one month lag behind the annual peaks (November) of TWS anomalies and precipitation anomalies. This is expected where the wetlands receive majority of its water from upland runoff, and confirms the finding of *Lee et al.* (2011).

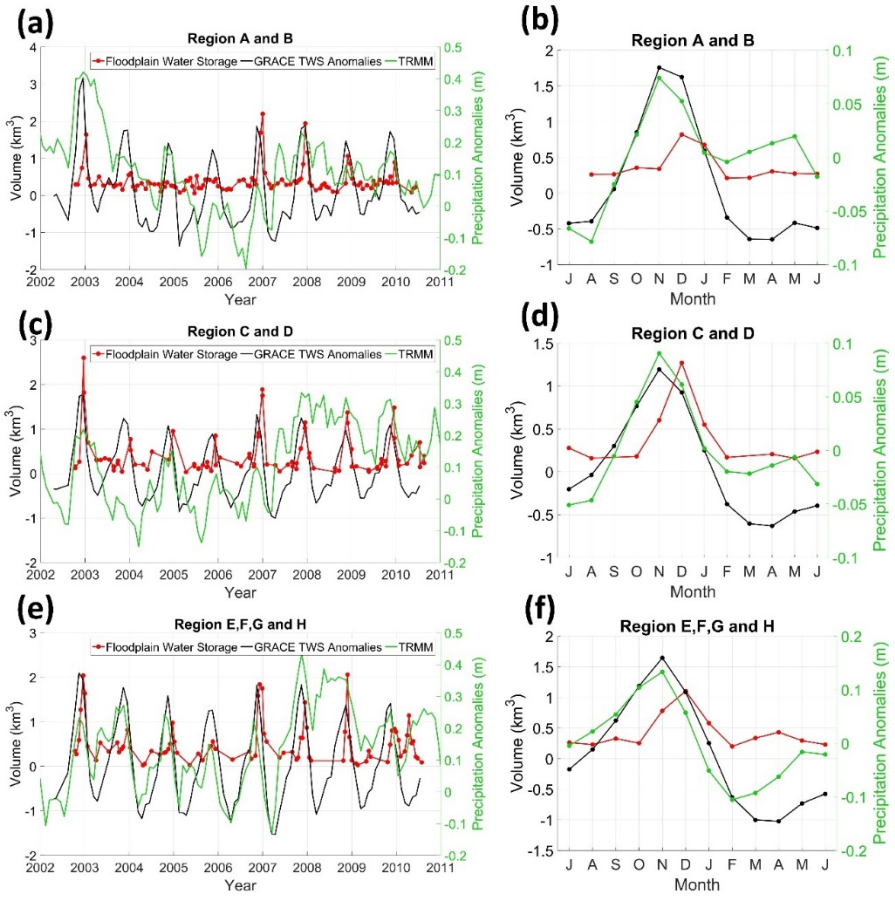

Figure 5-11 (Left) Comparison of wetland water storage with TWS anomalies from GRACE and precipitation anomalies from TRMM. (Right) Monthly mean anomalies of wetland water storage, GRACE TWS and precipitation.

5.5 Discussions and Conclusions

In this study, a new method was developed to estimate absolute water storage in the Congo wetlands for the period of 2002 – 2011 by constructing the $d - V$ relationship using two-dimensional water depth maps from integration of InSAR and altimetry measurements. This method of constructing the $d - V$ relationship is different from the method in previous studies (*Hayashi and Van Der Kamp*, 2000; *Lane and D'Amico*, 2010; *Minke et al.*, 2010) which used dense in-situ bathymetry networks in the wetlands. Those in-situ measurements allowed estimation of water depths, inundated area, and hence the water volumes in the wetlands. Our approach takes advantage of InSAR and altimetry measurements towards estimating absolute water storages and can be useful for relatively large wetlands where in-situ bathymetry data is limited. The established $d - V$ can contribute to understanding the role of wetlands in storing water and its contribution to river runoff. However, it should be noted that our method is established based on Equation (5-5) which assumes that water depth decreases by the same amount of Δh for all pixels with water depth larger than Δh. This assumption is generally valid for relatively small lakes or wetlands with little temporal variation in their water surface slopes. Extra caution is needed if the method is applied to the wetlands which may have significant temporal variation of water surface slopes.

It is not straightforward to directly assess the uncertainty of the estimated absolute water storages because it is estimated from multiple data sources and assumptions. Furthermore, there is no in-situ water level change or water depth data in the Congo wetlands that we have access to. Perhaps the Everglades wetlands in Florida, USA are the only wetlands equipped with a dense in-situ network. *Wdowinski et al.* (2008) evaluated

the accuracy of InSAR using JERS-1 L-band images to be 5 – 10 cm in measuring water level change by comparing it with that from in-situ gauges in the Everglades wetlands. *Hong et al.* (2010) suggested uncertainty of InSAR-derived water level changes to be 3 – 4 cm using Radarsat-1 C-band images over a water conservation area in the Everglades wetlands. On the other hand, the comparison between InSAR and altimetry-derived water level changes in Figure 5-4 reveals that the RMSDs between them vary from 5 – 22 cm. Thus, the accuracy of altimetry-derived water level changes over the wetlands in this study ranges from 7.1 cm to 24.2 cm (from sum of the variances). Given that this value is similar to the accuracy of d^t_{max} which we used in the $d - V$ relationship, the relative accuracy of the water storage can be estimated using $\frac{\sigma_V}{V} = (1 + 1/p) * (d^t_{max})^{-1} \cdot \sigma_{d^t_{max}}$. Hence, the relative accuracy of our method can improve with an increase of p value and d^t_{max}. If d^t_{max} equals to 2 m and p equals to 0.4 like the case in the Congo wetlands, the relative accuracy of our method varies from 12.4% to 42%.

Overall, absolute wetland water storage estimates was compared with those from *Lee et al.* (2015). The agreement between our results and estimates from *Lee et al.* (2015) suggest our method can predict reasonable water storages over the wetland. A comparison between our wetland water storages anomalies with GRACE TWS anomalies, and TRMM precipitation anomalies was presented. Our wetland water storages overall agree with the seasonal variations of TWS and precipitation anomalies. The mean amplitude of wetland water storage is about 3.98 ± 0.59 km^3 with peaks at December which lags behind TWS changes and precipitation changes by one month. The results also exhibit inter-annual variability, with maximum water volume of 6.3 ± 0.68km^3 in wet year of 2002 and

minimum volume of 2.2 ± 0.61 km^3 in dry year of 2005. The inter-annual variation of wetland water storages can be explained by the changes of precipitation from TRMM.

Chapter 6 Wetland Hydrology in the Central Cuvette

6.1 Introduction

A wetland's formation and maintenance is highly connected to its seasonal flood dynamics (*Hughes*, 1997; *Ward et al.*, 1999; *Tockner and Stanford*, 2002). During water residence in the floodplain, the biogeochemical environment of the floodwater is modified due to the influence of sedimentation, sorption and redox reactions, and biotic processes (*Richey et al.*, 1989; *Hamilton*, 2002). Inundation of the wetlands is the usually the composite consequences of different influxes. The influxes can be classified by its origination, such as regional water of over-bank flow from the river, and local water including ground water, hyporheic water, local tributary water and direct precipitation (*Mertes*, 1997). Different water sources could make a difference in the sediment supplies, carbon and nutrient exchange. Few studies have investigated the sources and sinks of the water in the Congo wetlands. *Lee et al.* (2011) has investigated the source and amount of water in the Congo wetland in sub-basin scale and concluded that local water is the main source of Congo's wetlands water. However, there has been no attempt to quantify local-scale hydrologic fluxes in the Congo wetlands.

In this study, we quantify the fluxes including precipitation P, upland runoff Q_{upland}, evapotranspiration ET and wetland-river exchanges Q_{river}^{mb} supplying and draining the wetlands using mass balance analysis. With Q_{river}^{mb}, water depth and water surface slope from altimetry measurements, two hydrological parameters (K_f and β) were derived specific to Congo wetlands using a 1-D diffusion model (*Kadlec*, 1990).

6.2 Method

6.2.1 Rate of Water Storage Changes

Rate of water storage changes ΔS is calculated using water storages (V) from Chapter 5 with Equation (6-1),

$$\Delta S = \Delta V / \Delta t, \tag{6-1}$$

where ΔV is computed using every two temporally adjacent water storage estimates, and Δt is the time span between the acquisition time of water storages. It should be noted that V from Chapter 5 are computed using two Envisat passes intersecting with each wetland which results in different temporal sampling rates of V for each wetland Table 6-1. The differences in temporal sampling rate is due to the revisiting time of the two intersecting Envisat passes. Regions C, D, E and F have 33 or 2 days sampling rates. The dramatic difference in temporal sampling could results in large errors in estimating ΔS. Thus, V from only one Envisat pass was used to estimate ΔS for regions C, D, E and F. V from Pass 386 is used for regions C and D while V from Pass 300 is used for regions E and F. Also, V from noisy altimetry measurements are interpolated with zeros based on the fact that dry land results in noisy altimetry measurements.

Table 6-1 Summary of temporal sampling rate over each floodplain.

Wetland	Length along Congo mainstem (km)	Envisat Passes	Temporal Sampling Rate (day)
A	39.2	429, 930	17, 18
B	132	429, 930	17, 18
C	81.14	343, 386	33, 2
D	39.05	343, 386	33, 2
E	27.18	257, 300	33, 2
F	73.4	257, 300	33, 2
G	75.85	300, 715	14, 21
H	77.22	300, 715	14, 21

6.2.2 Hydrological Flux Balance

The mass balance analysis will be conducted to estimate wetland river water exchange rate $Q_{river}^{mb}(t)$ using Equation (6-2).

$$\Delta S = Q_{river}^{mb}(t) - q - Q_{upland}(t), q = P - ET, \quad (6\text{-}2)$$

where ΔS is rate of water storage change from Equation (6-1), q is difference of precipitation and evapotranspiration, P is precipitation from TRMM data, ET is evapotranspiration from MODIS data, $Q_{upland}(t)$ is upland runoff estimated from Hillslope River Routing (HRR) Model, and $Q_{river}^{mb}(t)$ is the wetlands river exchange rate to be estimated.

6.2.3 1-D Wetlands Flow

A 1-D model wetland model will be applied to simulate the wetland river water exchange rate. Equation (6-3) was adopt to simulate wetland and river water exchanges:

$$\mathrm{U} = K_f * h^{\beta} * S_f^{\lambda},\ Q_{river}^{model} = \mathrm{U} * h * L_f, \tag{6-3}$$

where U is speed of flow, $\mathrm{K_f}$ is the flow conductivity coefficient (m/day/ $\mathrm{m^{\beta}}$), h is surface water depth from satellite altimetry which is the maximum water depth in Figure 5-7, β is the depth exponent, S_f is the friction slope (or hydraulic gradient) (m/m), λ depends on the flow regime, with $\lambda = 1$ for laminar flow and $\lambda = 0.5$ for turbulent flow and L_f is the length of the floodplain along the Congo main-stem which is listed in Table 5-3. The value of $\mathrm{K_f}$ represents the total flow conductance. β depends on the microtopography and stem density distribution. The friction slope S_f is estimated as $\partial h/\partial x$, where h is surface elevation and x is distance. S_f will be derived from altimetry measured water surface level. The water flow in this study is treated as laminar flow. Calibration of λ, $\mathrm{K_f}$, and β will be illustrated in Section 6.3.3.

6.3 Results

6.3.1 Temporal Dynamics of Fluxes

Each flux in Equation (6-2) is shown in Figure 6-1. Positive values indicate water filling the wetland while the negative values indicate water draining from the wetland. For most of the time of each year, P and Q_{upland} are the dominant sources in filling the wetlands. Q_{river} is the dominant inflow sources only in high water seasons. Instead, for most of each year, Q_{river} drains the wetlands which is demonstrated by the negative red columns in Figure 6-1. Overall, ET drains less water than Q_{river}.

Table 6-2 summarizes all the cumulative fluxes through the wetlands 2003 to 2010. Q_{river} contributes less than 15% of the total inflows into the wetlands. Precipitation contributes 26% to 49% while upland runoff contributes 42% to 64% of the total inputs.

Q_{river} drains 59% to 80% of the total outputs while ET is responsible for 20% to 41% of the total outputs. The mass balance analysis suggests that the Congo wetlands don't receive much water from the river but supply water to the river.

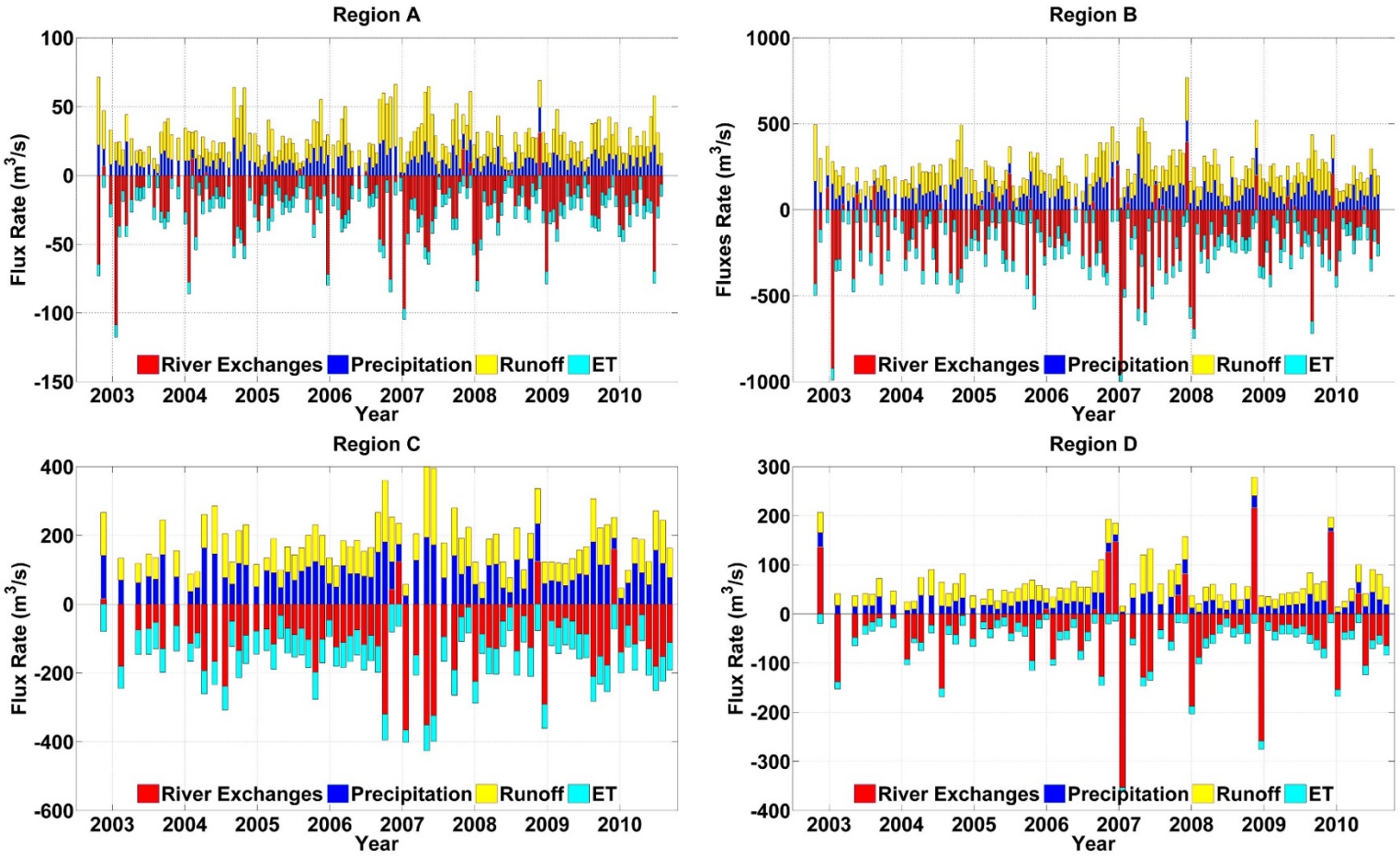
Region A
Flux Rate (m3/s)
100
50
0
-50
-100
-150
River Exchanges
Precipitation
Runoff
ET
2003
2004
2005
2006
2007
2008
2009
2010
Year
Region B
Fluxes Rate (m3/s)
1000
500
0
-500
-1000
River Exchanges
Precipitation
Runoff
ET
2003
2004
2005
2006
2007
2008
2009
2010
Year
Region C
Flux Rate (m3/s)
400
200
0
-200
-400
-600
River Exchanges
Precipitation
Runoff
ET
2003
2004
2005
2006
2007
2008
2009
2010
Year
Region D
Flux Rate (m3/s)
300
200
100
0
-100
-200
-300
-400
River Exchanges
Precipitation
Runoff
ET
2003
2004
2005
2006
2007
2008
2009
2010
Year

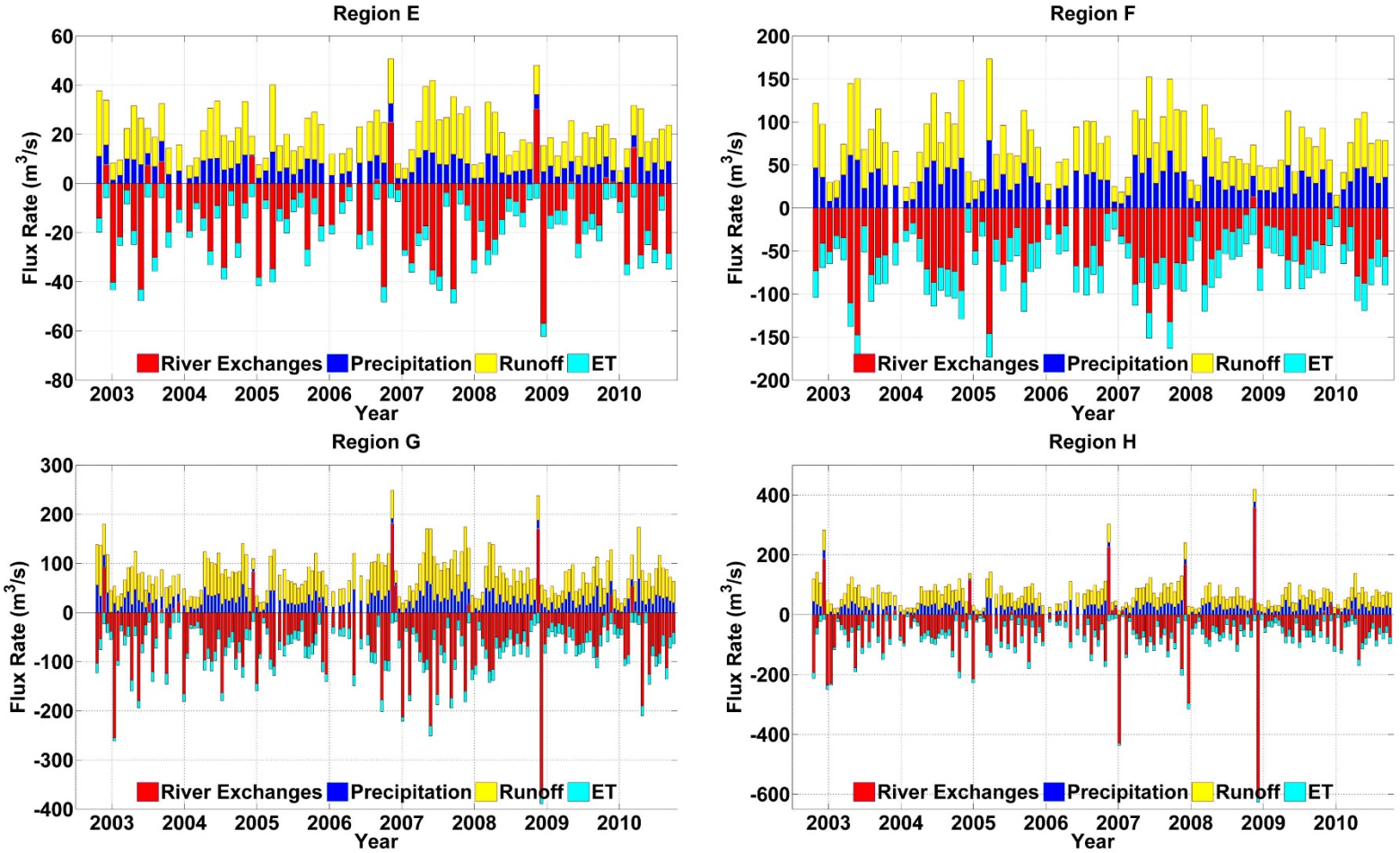

Figure 6-1 Flux rates over each wetland. The location of each region is referred to Figure 5-2.

Table 6-2 Annual cumulative fluxes over each region. Shaded data represents the percentage of each flux in filling and draining the wetlands.

	Source terms (m)			Sink terms (m)		Source terms (m)			Sink terms (m)	
	Region A					Region B				
Year	Qriver	P	Runoff	Qriver	ET	Qriver	P	Runoff	Qriver	ET
2003	0.17	1.42	1.12	1.85	1.25	0.25	1.43	1.79	2.81	1.25
2004	0.21	1.63	1.45	2.12	1.37	0.04	1.88	2.52	3.28	1.30
2005	0.09	1.46	1.17	1.56	1.37	0.36	1.56	1.93	2.55	1.31
2006	0.49	1.78	1.68	1.59	1.42	0.66	1.73	2.51	2.52	1.33
2007	0.45	1.73	1.59	2.72	1.28	0.54	2.01	3.03	4.93	1.23
2008	0.37	1.45	1.17	2.18	1.36	0.17	1.75	2.35	3.27	1.34
2009	0.13	1.58	1.33	1.49	1.40	0.27	1.78	2.51	3.28	1.36
Average	0.27	1.58	1.36	1.93	1.35	0.33	1.73	2.38	3.23	1.30
Percent in sources and sinks	0.08	0.49	0.42	0.59	0.41	0.07	0.39	0.54	0.71	0.29
	Region C					Region D				
2003	0.09	1.54	1.34	1.99	1.37	0.06	1.51	3.40	4.13	1.32
2004	0.47	1.73	1.68	2.62	1.19	0.94	1.71	4.36	5.76	1.16
2005	0.26	1.64	1.45	2.28	1.34	0.58	1.53	3.58	4.73	1.31
2006	0.34	1.71	1.69	1.92	1.28	0.21	1.73	4.44	4.42	1.25
2007	0.17	2.01	2.08	3.29	1.18	0.56	2.02	5.56	7.24	1.15
2008	0.41	1.52	1.37	2.16	1.39	0.82	1.42	3.41	4.58	1.39
2009	0.56	1.55	1.42	2.08	1.34	0.94	1.47	3.42	4.37	1.33
Average	0.33	1.67	1.58	2.33	1.30	0.59	1.63	4.02	5.03	1.28
Percent in sources and sinks	0.09	0.47	0.44	0.64	0.36	0.09	0.26	0.64	0.80	0.20
	Region E					Region F				
2003	0.92	1.52	3.11	5.42	1.28	0.29	1.60	2.41	3.90	1.24
2004	0.65	1.51	3.15	3.43	1.11	0.42	1.47	2.15	2.60	1.13
2005	0.10	1.58	3.03	3.88	1.22	0.24	1.48	2.02	2.81	1.20

Table 6-2 continued

2006	1.15	1.59	3.21	3.95	1.35	0.69	1.36	1.91	1.97	1.31
2007	1.27	2.07	4.37	7.21	1.29	0.76	1.82	2.65	4.73	1.28
2008	0.90	1.37	2.79	4.01	1.31	0.95	1.18	1.66	2.45	1.33
2009	0.79	1.43	2.81	3.00	1.36	0.25	1.32	1.78	1.64	1.37
Average	0.83	1.58	3.21	4.41	1.27	0.51	1.46	2.08	2.87	1.27
Percent in sources and sinks	0.15	0.28	0.57	0.78	0.22	0.13	0.36	0.51	0.69	0.31
	Region G					**Region H**				
2003	0.28	1.44	3.04	4.34	1.24	0.17	1.48	3.04	4.31	1.16
2004	0.32	1.59	3.43	4.07	1.16	0.50	1.43	2.82	3.80	1.14
2005	0.06	1.48	3.09	3.70	1.21	0.05	1.49	2.86	3.27	1.15
2006	0.84	1.54	3.34	3.51	1.32	0.99	1.38	2.74	2.61	1.24
2007	0.07	2.02	4.36	5.60	1.24	0.69	1.69	3.30	5.51	1.19
2008	0.65	1.53	3.28	4.51	1.40	1.38	1.31	2.55	4.04	1.36
2009	0.09	1.38	2.96	2.63	1.41	0.17	1.33	2.55	2.60	1.35
Average	0.33	1.57	3.36	4.05	1.28	0.56	1.45	2.84	3.73	1.23
Percent in sources and sinks	0.06	0.30	0.64	0.76	0.24	0.12	0.30	0.59	0.75	0.25

6.3.2 Water Surface Slope from Envisat Altimetry

Almost no sizeable channels are observed in the central Congo wetlands as shown in Figure 5-2. The river water flows into the adjacent wetlands as diffusive, non-channelized overbank flow. Overbank flow occurs only during high water level seasons as shown in Figure 6-1.

Variations of water surface slope are observed from Envisat altimetry measurements (Figure 6-2). Shaded areas in Figure 6-2 represent the intersection of wetlands and river. In low water seasons, elevation of the wetland is higher than the river while in high water season, elevation in the river is slightly higher than in the wetland. During low water season, it is higher in the wetlands than in the river, which means water can only flow from wetlands into the river. While during high water season, it is slightly higher in the river than in the wetlands, which means water can flow from river into the wetlands. The variations of water surface are consistent with the mass balance analysis in Section 6.3.1. A first order polynomial was applied to fit the measurements in the shaded areas in Figure 6-2 to represent water surface slope between the river and the wetlands.

Envisat passes 257, 300, 343, and 715 are almost perpendicular to the flow direction of the Congo mainstem. These measurements contain little contribution from river upstream-downstream slope. While the rest of the Envisat passes 429, 930 and 386 contain the contribution from river upstream downstream slope. In order to obtain water surface slope between the river and the wetlands, river upstream-downstream slope contributions are estimated and removed using the angle between Envisat ground pass and river slope in *O'Loughlin et al.* (2016).

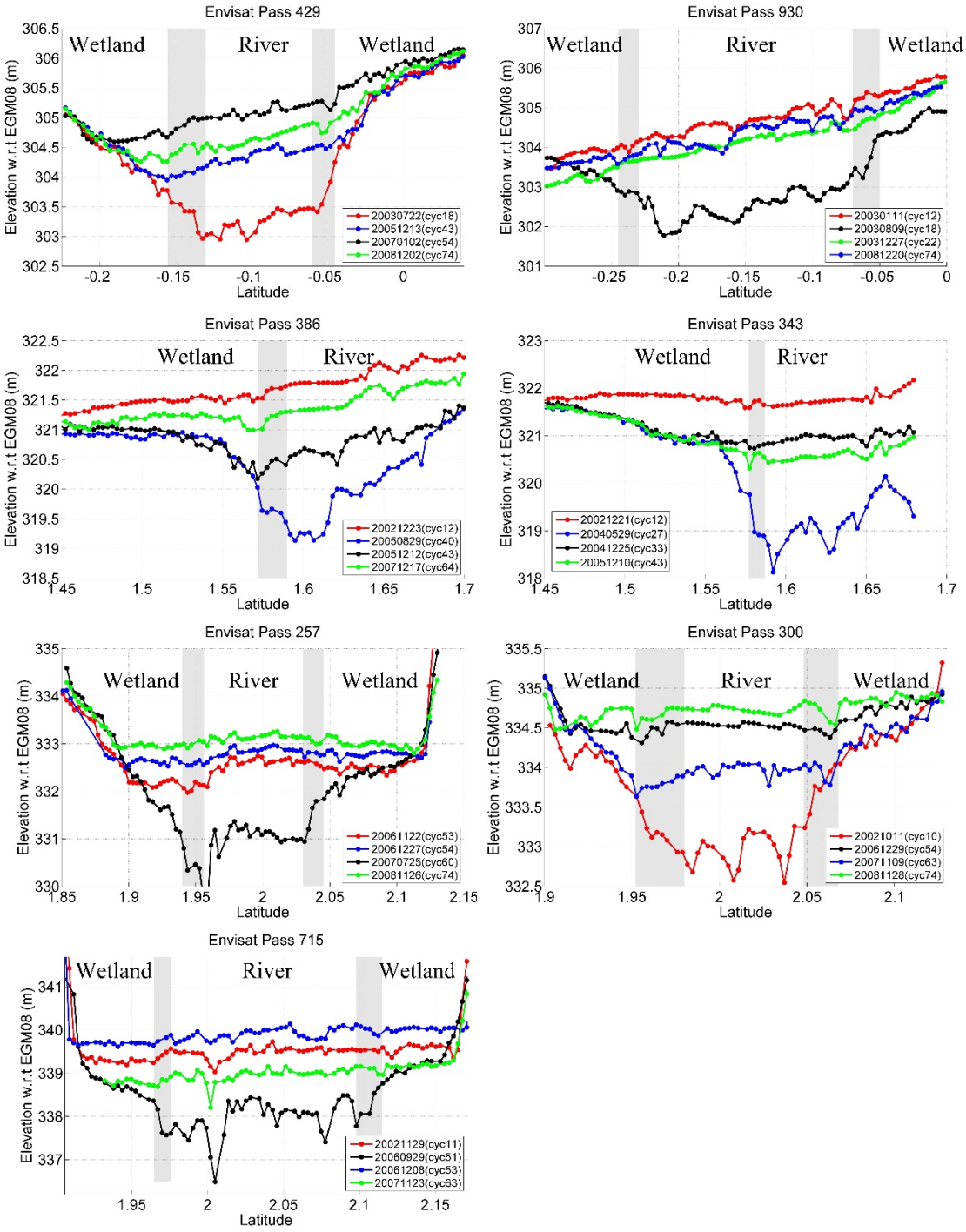

Figure 6-2 Selected profiles of Envisat altimetry measurements showing variations of the water surface. Location of each Envisat pass is referred to Figure 5-2.

6.3.3 Model Calibration

Three parameters (λ, K_f, β) in Equation (6-3) are unknown. λ is calibrated by calculating Reynold Number. The Reynold Number is calculated using

$$Re=d\rho U/\mu, \quad (6\text{-}4)$$

where Re is Reynold number, d is water depth, U is velocity of water flow, μ is the dynamic viscosity. If Re is lower than 2000, the flow is laminar and λ will be 1. If Re is higher than 4000 the flow is turbulent and λ will be 0.5. The Re value is computed to be 2083 by using d=1.5 m, ρ=1000 kg/m^3, U=0.14 cm/s, $\mu = 10^{-3}$(N s/m^2). Thus, $\lambda = 1$ is used in this study.

High water level profiles from the seven passes in Figure 6-2 are selected to calibrate the parameters K_f and β. This is because radar altimetry measurements work well in high water seasons and wetlands-river exchanges are active during high water seasons. Since each studied wetland (see Figure 5-2 for location the wetlands) has different sizes, the fluxes in Figure 6-1 were firstly converted into flow rate by dividing floodplain length (L_f) and water depth (d_{mat}^t) for each wetland using

$$U^{mb} = \frac{Q_{river}^{mb}}{d_{mat}^t * L_f}, \quad (6\text{-}5)$$

where U^{mb} the is velocity of water exchange rates estimated using Q_{river}^{mb} from Equation (6-2), d_{mat}^t is maximum water depth with the same values as Figure 5-7.

The calibration processes determined the values of K_f and β using a search space based on minimum values of Root Mean Squared Error (RMSE) between U^{model} and U^{mb}, following the same method in (*Choi and Harvey*, 2013). The RMSE values with different

K_f and β are shown in Figure 6-3. The minimum RMSE value is 1.45 m/hr with optimized values of $K_f = 65220\ (m/d/m^{\beta})$ and $\beta = 3.1$. By inserting $K_f = 65220\ (m/d/m^{\beta})$ and $\beta = 3.1$ into Equation (6-3), a model derived U^{model} is obtained. The comparison between U^{mb} and U^{model} is shown in Figure 6-4. As we can see in Figure 6-4, the 1-D wetlands model adequately represents the wetlands river exchanges.

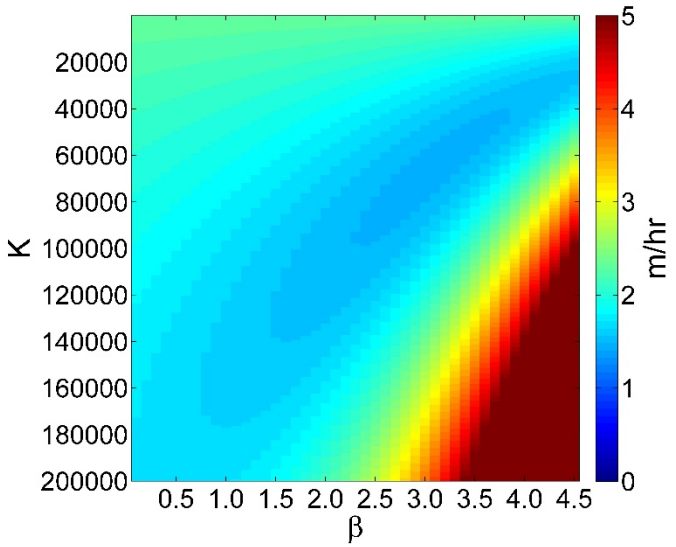

Figure 6-3 RMSE between U^{mb} and U^{model} with different K_f and β values.

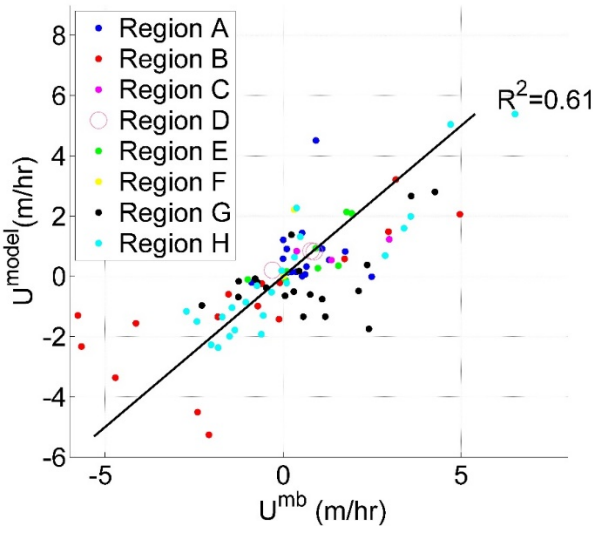

Figure 6-4 Comparison between U^{mb} and U^{model}.

6.4 Discussions and Conclusions

The mass balance analysis over the Congo wetlands has been conducted in this chapter. It shows that the Congo wetlands receives a majority of its water from local water, not from regional water. This indicates that the wetlands receive little carbon and sedimentation from the river. Instead, the wetland river exchanges drain most of the water in the wetlands, which suggests the wetlands is a supplier of carbon to the Congo River.

The water surface slope dynamics observed from Envisat altimetry between wetlands and the Congo main-stem also support the results from this mass balance analysis. A one-dimensional wetlands model is applied to simulate wetlands river exchanges. Two parameters K_f and β specific to Congo wetlands are derived using space-borne measurements.

Chapter 7 Conclusions and Future Work

7.1 Contributions and Conclusions

Tropical wetlands are one of the most important sources of global carbon and methane emissions, and play a significant role in regulating water balance and maintaining biodiversity (*Barbier*, 1994; *Neue et al.*, 1997; *Hayashi et al.*, 1998). The water flow through the wetlands, which governs biogeochemical process, sediment delivery and nutrient exchange, is probably the most important controlling factor (*Mitsch and Gosselink*, 2007). The Congo River Basin is one of the least studied major river basins and little is known about its hydrology and hydrodynamics. In order to better understand the spatio-temporal variations of wetlands water as well as the its sources and sinks, this study focused on the opportunities provided by the integration of radar altimetry, SAR, and InSAR because it permits mapping $\partial h/\partial t$ within the wetlands with high spatial resolution.

This dissertation starts from investigating the relationship between L-band PALSAR σ_0 and seasonal water level changes obtained from Envisat altimetry over the island of Île Mbamou in the Congo Basin where two distinctly different vegetation types (forested and non-forested) are found. PALSAR σ_0 exhibits positive correlation with water level changes over the forested southern Île Mbamou whereas both positive and negative correlations are observed over the non-forested northern Île Mbamou depending on the amount of water level increase. Based on the analysis of σ_0 sensitivity, denser vegetation canopy leads to less sensitive σ_0 variation with respect to the water level changes regardless of forested or non-forested canopy. Furthermore, a method was developed by integrating PALSAR σ_0, Envisat altimetry and MODIS VCF to estimate water level

changes which were then compared with the Envisat altimetry and InSAR results. This σ_0 method suggests adequate accuracy in regions with medium-low vegetation canopy where InSAR could lose coherence. On the other hand, the accuracy of the σ_0 method is hampered in regions with dense forested canopy where InSAR can maintain coherence for measuring $\partial h/\partial t$.

Multi-temporal $\partial h/\partial t$ maps were then generated with ALOS PALSAR interferograms and Envisat altimetry data in the Congo forested wetland near Lisala in Democratic Republic of the Congo. Three fringe patterns from PALSAR interferograms were identified due to spatio-temporal water level changes in the wetland: (1) dense fringes parallel to the Congo mainstem in high water season; (2) broad fringes across the wetland; (3) fringes around the wetland boundary in low water season. The absolute water level change maps generated by integrating InSAR and Envisat altimetry data suggest that $\partial h/\partial t$ can reach up to 1.2 m in the proximal wetland in high water level season. During low water season, $\partial h/\partial t$ can be several decimeters. Based on the maps of absolute $\partial h/\partial t$ and the principle of mass continuity, the analysis of temporal hydraulic variations was also presented. The hydraulic analysis suggests that $\partial h/\partial t$ is subtle and the water flow in the wetland is not well confined during low water season. On the other hand, the proximal wetland has greater $\partial h/\partial t$ than the distal wetland during high water season, which suggests that water mostly flows from the wetland to river.

To better understand the inter-annual variations of water storages in the Congo wetlands, a new method was developed to estimate absolute water storages over the wetlands by establishing relationships between water depths (d) and water volumes (V) using 2-D water depth maps from the integration of InSAR and altimetry measurements.

This $d-V$ relation method and Envisat altimetry measurements were combined to construct time series of wetland's absolute water storages from 2002 to 2011. The $d-V$ relation was modelled using a power function, which revealed the cross-sectional geometry of the wetlands as a convex curve. The mean annual amplitude from 2002 to 2011 over the wetlands (~7,777 km^2) is 3.98 ± 0.59 km^3 with peaks in December, which lags behind total water storage (TWS) changes from the Gravity Recovery and Climate Experiment (GRACE) and precipitation changes from Tropical Rainfall Measuring Mission (TRMM) by about one month. The absolute water storages also exhibit inter-annual variability, with maximum water volume of 6.3 ± 0.68 km^3 in the wet year of 2002 and minimum volume of 2.2 ± 0.61 km^3 in the dry year of 2005. The inter-annual variation of water storages can be explained by the changes of precipitation from TRMM.

The absolute water storages were then used to investigate sources and sinks in the wetlands along the middle reach of the Congo mainstem using a mass balance equation. Mass balance analysis suggests water in the river can only flow into the wetlands during high water season, which is also supported by the water surface slope variations from Envisat altimetry measurements. The averaged influxes values from 2003 to 2011 suggest that local water contributes more than 85% of total water inflow while regional supplies less than 15% of total water inflow to the wetlands. The averaged outfluxes suggest that wetland river exchanges drain 59% to 80 % of the outflow and evapotranspiration drain 20% to 41% of the out flow. A wetland model integrated with water surface slope and water depth from satellite altimetry was applied to derive hydrological parameters K_f of 65220 $(m/d/m^{\beta})$ and β of 3.1 which are specific to the Congo wetlands.

7.2 Future Work

7.2.1 Correcting InSAR-derived $\partial h/\partial t$ with SAR σ_0

Satellite altimetry has been used to convert InSAR-derived relative $\partial h/\partial t$ into absolute $\partial h/\partial t$. However, some regions do not have altimetry tracks or altimetry measurements does not perform well over rough terrain. One of the solutions to overcome the absence of altimetry measurements is to use the SAR backscattering coefficient which can be also used to estimate water level changes but less accurate than InSAR. The method in Chapter 3 has the potential to calibrate InSAR derived $\partial h/\partial t$ over regions without altimetry tracks.

7.2.2 Mapping Two-dimensional Wetland Bathymetry

The water level changes in the Congo wetlands appear to be mostly controlled by wetlands bathymetry and water level. Chapter 5 characterized the wetlands bathymetry to be a convex shape by establishing the $d - V$ relationships. The method in Chapter 5 increased the temporal sampling of water storage but lost spatial resolution in mapping $\partial h/\partial t$. One method to improve this limitation is to map the two-dimensional wetland bathymetry. The implementation is composed of two steps: 1) first interpolate the water level in the high water season to each InSAR pixel and obtain $h(i,j)$; 2) then subtract the absolute water level changes from $h(i,j)$ to obtain $h_{bathymetry}(i,j)$, such as

$$h_{bathymetry}(i,j) = h(i,j) - \partial h/\partial t(i,j), \tag{7-1}$$

where i,j represent the location of each SAR pixel position. It is expected that this wetlands bathymetry can be used to obtain two dimensional $\partial h/\partial t$ with altimeter measurements.

This $h_{bathymetry}$ can also be used in a hydrodynamic model to simulate two dimensional water flow in the wetlands.

7.2.3 Quantifying Interannual Water Storage Variations over the Whole Congo Basin

Water storage estimations in Chapter 5 show interannual variations of water storages over the identified wetlands with driest year in 2005. However, there are no studies quantifying the interannual surface water storages over the whole Congo Basin yet. GIEMS datasets and GRACE measurements can be used to quantify this interannual variations. The results can be used to evaluate the impacts of El Niño over the Congo Basin by comparing interannual water storages over the Amazon Basin, which also experienced exceptional dry year in 2005.

7.2.4 Modelling of Wetland Hydrodynamics

Mass balance analysis in Chapter 6 suggests that during low water seasons, wetlands are not flooded by water from the river but supply water to the river. On the other hand, during high water seasons, water in wetlands is partially supplied by the river. Detailed flooding process within the wetlands and the interactions of different water sources are unknown. For example, it is unknown to what extents the wetlands is only flooded by local water and to what extents the wetlands is flooded by mixed water. Different flooding patterns are likely to have different effects on the ecosystem (Tockner et al., 2000). Numerical models permit the study of interactions among different water sources. One of the input for the hydrodynamic models – wetlands bathymetry can be obtained using the method proposed in 7.2.2.

References

Aires, Filipe, Fabrice Papa, and Catherine Prigent. 2013. "A Long-Term, High-Resolution Wetland Dataset over the Amazon Basin, Downscaled from a Multiwavelength Retrieval Using SAR Data." *Journal of Hydrometeorology* 14 (2): 594–607.

Alsdorf, Doug, Paul Bates, John Melack, Matt Wilson, and Thomas Dunne. 2007. "Spatial and Temporal Complexity of the Amazon Flood Measured from Space." *Geophysical Research Letters* 34 (L08402): 1–5.

Alsdorf, Douglas, Ed Beighley, Alain Laraque, Hyongki Lee, Raphael Tshimanga, Fiachra O'Loughlin, Gil Mahé, Bienvenu Dinga, Guy Moukandi, and Robert G. M. Spencer. 2016. "Opportunities for Hydrologic Research in the Congo Basin." *Reviews of Geophysics* 54 (2): 378–409.

Alsdorf, Douglas E., Laurence C. Smith, and John M. Melack. 2001. "Amazon Floodplain Water Level Changes Measured with Interferometric SIR-C Radar." *IEEE Transactions on Geoscience and Remote Sensing* 39 (2): 423–31.

Alsdorf, Douglas E, Ernesto Rodríguez, and Dennis P Lettenmaier. 2007. "Measuring Surface Water from Space." *Reviews of Geophysics* 45 (2): RG2002.

Alsdorf, Douglas, Shin-Chan Han, Paul Bates, and John Melack. 2010. "Seasonal Water Storage on the Amazon Floodplain Measured from Satellites." *Remote Sensing of Environment* 114 (11): 2448–56.

Bailey, R. G., and K. E. Banister. 1986. "The Zaïre River System." In *The Ecology of River Systems*, edited by Bryan. R. Davies and Keith. F. Walker, 60:201–24. Netherlands: Springer.

Bamber, J. L. 1994. “Ice Sheet Altimeter Processing Scheme.” *International Journal of Remote Sensing* 15 (4): 925–38.

Barbier, Edward B. 1994. “Valuing Environmental Functions: Tropical Wetlands.” *Land Economics* 70 (2). University of Wisconsin Press: 155–73.

Baugh, Calum A., Paul D. Bates, Guy Schumann, and Mark A. Trigg. 2013. “SRTM Vegetation Removal and Hydrodynamic Modeling Accuracy.” *Water Resources Research* 49 (9): 5276–89.

Bayer, T., R. Winter, and G. Schreier. 1991. “Terrain Influences in SAR Backscatter and Attempts to Their Correction.” *IEEE Transactions on Geoscience and Remote Sensing*.

Becker, Mélanie, Joecila da Silva, Stéphane Calmant, Vivien Robinet, Laurent Linguet, and Frédérique Seyler. 2014. “Water Level Fluctuations in the Congo Basin Derived from ENVISAT Satellite Altimetry.” *Remote Sensing* 6 (10): 9340–58.

Beighley, R. E., R. L. Ray, Y. He, H. Lee, L. Schaller, K. M. Andreadis, M. Durand, D. E. Alsdorf, and C. K. Shum. 2011. “Comparing Satellite Derived Precipitation Datasets Using the Hillslope River Routing (HRR) Model in the Congo River Basin.” *Hydrological Processes* 25 (20): 3216–29.

Berardino, Paolo, Gianfranco Fornaro, Riccardo Lanari, and Eugenio Sansosti. 2002. “A New Algorithm for Surface Deformation Monitoring Based on Small Baseline Differential SAR Interferograms.” *IEEE Transactions on Geoscience and Remote Sensing* 40 (11): 2375–83.

Berry, P. A. M., J. D. Garlick, J. A. Freeman, and E. L. Mathers. 2005. “Global Inland

Water Monitoring from Multi-Mission Altimetry." *Geophysical Research Letters* 32 (16): L16401.

Birkett, C. M. 1995. "The Contribution of TOPEX/POSEIDON to the Global Monitoring of Climatically Sensitive Lakes." *Journal of Geophysical Research* 100 (C12): 25179.

Birkett, C. M., L. A. K. Mertes, T. Dunne, M. H. Costa, and M. J. Jasinski. 2002. "Surface Water Dynamics in the Amazon Basin: Application of Satellite Radar Altimetry." *Journal of Geophysical Research: Atmospheres* 107 (D20): LBA-26.

Birkett, Charon M. 1998. "Contribution of the TOPEX NASA Radar Altimeter to the Global Monitoring of Large Rivers and Wetlands." *Water Resources Research* 34 (5). Wiley Online Library: 1223–39.

Brown, Charles G., Kamal Sarabandi, and Leland E. Pierce. 2010. "Model-Based Estimation of Forest Canopy Height in Red and Austrian Pine Stands Using Shuttle Radar Topography Mission and Ancillary Data: A Proof-of-Concept Study." *Geoscience and Remote Sensing, IEEE Transactions on* 48 (3): 1105–18.

Bwangoy, Jean Robert B., Matthew C. Hansen, David P. Roy, Gianfranco De Grandi, and Christopher O. Justice. 2010. "Wetland Mapping in the Congo Basin Using Optical and Radar Remotely Sensed Data and Derived Topographical Indices." *Remote Sensing of Environment* 114 (1): 73–86.

Campbell, D. 2005. "The Congo River Basin." In *The World's Largest Wetlands: Ecology and Conservation*, edited by Lauchlan H. Fraser and Paul A. Keddy, 149–65. Cambridge, UK: Cambridge University Press.

Chen, J. L., C. R. Wilson, and B. D. Tapley. 2010. "The 2009 Exceptional Amazon Flood

and Interannual Terrestrial Water Storage Change Observed by GRACE." *Water Resources Research* 46 (12): W12526.

Choi, Jungyill, and Judson W. Harvey. 2013. "Relative Significance of Microtopography and Vegetation as Controls on Surface Water Flow on a Low-Gradient Floodplain." *Wetlands* 34 (1): 101–15.

Coe, Michael T. 1998. "A Linked Global Model of Terrestrial Hydrologic Processes: Simulation of Modern Rivers, Lakes, and Wetlands." *Journal of Geophysical Research: Atmospheres* 103 (D8): 8885–99.

Costa, M. P. F., O. Niemann, E. Novo, and F. Ahern. 2002. "Biophysical Properties and Mapping of Aquatic Vegetation during the Hydrological Cycle of the Amazon Floodplain Using JERS-1 and Radarsat." *International Journal of Remote Sensing* 23 (7): 1401–26.

Costantini, M. 1998. "A Novel Phase Unwrapping Method Based on Network Programming." *Geoscience and Remote Sensing, IEEE Transactions on* 36 (3): 813–21.

Davis, C. H. 1997. "A Robust Threshold Retracking Algorithm for Measuring Ice-Sheet Surface Elevation Change from Satellite Radar Altimeters." *IEEE Transactions on Geoscience and Remote Sensing*.

Deng, Xiaoli. 2003. "Improvement of Geodetic Parameter Estimation in Coastal Regions from Satellite Radar Altimetry." Ph.D Dissertation, Curtin University of Technology.

DiMiceli, C.M., M.L. Carroll, R.A. Sohlberg, C. Huang, M.C. Hansen, and J.R.G. Townshend. 2011. "Annual Global Automated MODIS Vegetation Continuous Fields

(MOD44B) at 250 M Spatial Resolution for Data Years Beginning Day 65, 2000 - 2010, Collection 5 Percent Tree Cover." College Park, Maryland, Maryland: University of Maryland.

Dunne, Thomas, Leal A. K. Mertes, Robert H. Meade, Jeffrey E. Richey, and Bruce R. Forsberg. 1998. "Exchanges of Sediment between the Flood Plain and Channel of the Amazon River in Brazil." *Geological Society of America Bulletin* 110 (4): 450.

ESA. 2007. "ENVISAT RA2/MWR Product Handbook."

Foster, J., B. Brooks, T. Cherubini, C. Shacat, S. Businger, and C. L. Werner. 2006. "Mitigating Atmospheric Noise for InSAR Using a High Resolution Weather Model." *Geophysical Research Letters* 33 (16): L16304.

Frappart, F., K. Do Minh, J. L'Hermitte, A. Cazenave, G. Ramillien, T. Le Toan, and N. Mognard-Campbell. 2006. "Water Volume Change in the Lower Mekong from Satellite Altimetry and Imagery Data." *Geophysical Journal International* 167 (2): 570–84.

Frappart, F., S. Calmant, M. Cauhope, F. Seyler, and A. Cazenave. 2006. "Preliminary Results of ENVISAT RA-2-Derived Water Levels Validation over the Amazon Basin." *Remote Sensing of Environment* 100 (2): 252–64.

Frappart, Frédéric, Frédérique Seyler, Jean-Michel Martinez, Juan G. León, and Anny Cazenave. 2005. "Floodplain Water Storage in the Negro River Basin Estimated from Microwave Remote Sensing of Inundation Area and Water Levels." *Remote Sensing of Environment* 99 (4): 387–99.

Freeman, A., and S. L. Durden. 1998. "A Three-Component Scattering Model for

Polarimetric SAR Data." *IEEE Transactions on Geoscience and Remote Sensing*.

Goldstein, Richard M., and Charles L. Werner. 1998. "Radar Interferogram Filtering for Geophysical Applications." *Geophysical Research Letters* 25 (21): 4035–38.

Grings, F. M., P. Ferrazzoli, H. Karszenbaum, M. Salvia, P. Kandus, J. C. Jacobo‐Berlles, and Pablo Perna. 2008. "Model Investigation about the Potential of C Band SAR in Herbaceous Wetlands Flood Monitoring." *International Journal of Remote Sensing* 29 (17–18): 5361–72.

Grings, F., M. Salvia, H. Karszenbaum, P. Ferrazzoli, P. Kandus, and P. Perna. 2009. "Exploring the Capacity of Radar Remote Sensing to Estimate Wetland Marshes Water Storage." *Journal of Environmental Management* 90 (7): 2189–98.

Grings, F.M., Paolo Ferrazzoli, J.C. Jacobo-Berlles, Haydee Karszenbaum, Javier Tiffenberg, Paula Pratolongo, and Patricia Kandus. 2006. "Monitoring Flood Condition in Marshes Using EM Models and Envisat ASAR Observations." *IEEE Transactions on Geoscience and Remote Sensing* 44 (4): 936–42.

Guo, J. Y., X. J. Duan, and C. K. Shum. 2010. "Non-Isotropic Gaussian Smoothing and Leakage Reduction for Determining Mass Changes over Land and Ocean Using GRACE Data." *Geophysical Journal International* 181 (1): 290–302.

Hamilton, Stephen K. 2002. "Comparison of Inundation Patterns among Major South American Floodplains." *Journal of Geophysical Research* 107 (D20): 8038.

Hansen, M. C., P. V. Potapov, R. Moore, M. Hancher, S. A. Turubanova, A. Tyukavina, D. Thau, S.V., Goetz, S.J., Loveland, T.R. and Kommareddy, A. 2013. "High-Resolution Global Maps of 21st-Century Forest Cover Change." *Science* 342 (6160).

American Meteorological Society: 850–53.

Hansen, Matthew C., David P. Roy, Erik Lindquist, Bernard Adusei, Christopher O. Justice, and Alice Altstatt. 2008. "A Method for Integrating MODIS and Landsat Data for Systematic Monitoring of Forest Cover and Change in the Congo Basin." *Remote Sensing of Environment* 112 (5): 2495–2513.

Hayashi, M, and G. Van Der Kamp. 2000. "Simple Equations to Represent the Volume-Area-Depth Relations of Shallow Wetlands in Small Topographic Depressions." *Journal of Hydrology* 237 (1–2): 74–85.

Hayashi, Masaki, Garth Van Der Kamp, and Dave L. Rudolph. 1998. "Water and Solute Transport between a Prairie Wetland and Adjacent Upland, 1. Water Balance." *Journal of Hydrology* 207: 42–55.

Hess, Laura L., John M. Melack, Solange Filoso, and Yong Wang. 1995. "Delineation of Inundated Area and Vegetation along the Amazon Floodplain with the SIR-C Synthetic Aperture Radar." *IEEE Transactions on Geoscience and Remote Sensing* 33 (4): 896–904.

Hess, Laura L., John M. Melack, Evlyn MLM Novo, Claudio CF Barbosa, and Mary Gastil. 2003. "Dual-Season Mapping of Wetland Inundation and Vegetation for the Central Amazon Basin." *Remote Sensing of Environment* 87 (4): 404–28.

Hong, Sang-Hoon, Shimon Wdowinski, Sang-Wan Kim, and Joong-Sun Won. 2010. "Multi-Temporal Monitoring of Wetland Water Levels in the Florida Everglades Using Interferometric Synthetic Aperture Radar (InSAR)." *Remote Sensing of Environment* 114 (11): 2436–47.

Hughes, Francine M.R. 1997. “Floodplain Biogeomorphology.” *Progress in Physical Geography* 21 (4): 501–29.

Hughes, Ralph H. 1992. *A Directory of African Wetlands*. IUCN.

JPL. 2014. “NASA Shuttle Radar Topography Mission Global 1 Arc Second.” https://lpdaac.usgs.gov/products/measures_products_table/srtmgl1.

Jung, Hahn Chul, and Doug Alsdorf. 2010. “Repeat-Pass Multi-Temporal Interferometric SAR Coherence Variations with Amazon Floodplain and Lake Habitats.” *International Journal of Remote Sensing* 31 (4): 881–901.

Jung, Hahn Chul, James Hamski, Michael Durand, Doug Alsdorf, Faisal Hossain, Hyongki Lee, A. K. M. Azad Hossain, Khaled Hasan, Abu Saleh Khan, and A.K.M. Zeaul Hoque. 2010. “Characterization of Complex Fluvial Systems Using Remote Sensing of Spatial and Temporal Water Level Variations in the Amazon, Congo, and Brahmaputra Rivers.” *Earth Surface Processes and Landforms* 35 (3): 294–304.

Jung, Hahn Chul, Michael Jasinski, Jin-Woo Kim, C. K. Shum, Paul Bates, Jeffrey Neal, Hyongki Lee, and Doug Alsdorf. 2012. “Calibration of Two-Dimensional Floodplain Modeling in the Central Atchafalaya Basin Floodway System Using SAR Interferometry.” *Water Resources Research* 48: 1–13.

Kadlec, Robert H. 1990. “Overland Flow in Wetlands: Vegetation Resistance.” *Journal of Hydraulic Engineering* 116 (5): 691–706.

Kasischke, Eric S., Kevin B. Smith, Laura L. Bourgeau-Chavez, Edwin A. Romanowicz, Suzy Brunzell, and Curtis J. Richardson. 2003. “Effects of Seasonal Hydrologic Patterns in South Florida Wetlands on Radar Backscatter Measured from ERS-2 SAR

Imagery." *Remote Sensing of Environment* 88: 423–41.

Keddy, Paul A., Lauchlan H. Fraser, Ayzik I. Solomeshch, Wolfgang J. Junk, Daniel R. Campbell, Mary T. K. Arroyo, and Cleber J. R. Alho. 2009. "Wet and Wonderful: The World's Largest Wetlands Are Conservation Priorities." *BioScience* 59 (1). Oxford University Press: 39–51.

Kim, Jin-Woo, Zhong Lu, John W. Jones, C.K. Shum, Hyongki Lee, and Yuanyuan Jia. 2014. "Monitoring Everglades Freshwater Marsh Water Level Using L-Band Synthetic Aperture Radar Backscatter." *Remote Sensing of Environment* 150 (July): 66–81.

Kim, Jin-Woo, Zhong Lu, Hyongki Lee, C.K. Shum, Christopher M. Swarzenski, Thomas W. Doyle, and Sang-Ho Baek. 2009. "Integrated Analysis of PALSAR/Radarsat-1 InSAR and ENVISAT Altimeter Data for Mapping of Absolute Water Level Changes in Louisiana Wetlands." *Remote Sensing of Environment* 113 (11): 2356–65.

Kim, Sang-Wan, Shimon Wdowinski, Falk Amelung, Timothy H. Dixon, and Joong-Sun Won. 2013. "Interferometric Coherence Analysis of the Everglades Wetlands, South Florida." *Geoscience and Remote Sensing, IEEE Transactions on* 51 (12). IEEE: 5210–24.

Kim, Sang-Wan, Sang-Hoon Hong, and Joong-Sun Won. 2005. "An Application of L-Band Synthetic Aperture Radar to Tide Height Measurement." *IEEE Transactions on Geoscience and Remote Sensing* 43 (7): 1472–78.

Kouraev, Alexei V., Elena A. Zakharova, Olivier Samain, Nelly M. Mognard, and Anny Cazenave. 2004. "Ob' River Discharge from TOPEX/Poseidon Satellite Altimetry

(1992–2002).” *Remote Sensing of Environment* 93 (1–2): 238–45.

Kruizinga, G.J. 1997. “Dual-Satellite Altimeter Crossover Measurements for Precise Orbit Determination.” Ph.D Dissertation, University of Texas at Austin.

Kwoun, Oh-ig, and Zhong Lu. 2009. “Multi-Temporal RADARSAT-1 and ERS Backscattering Signatures of Coastal Wetlands in Southeastern Louisiana.” *Photogrammetric Engineering & Remote Sensing* 75 (5): 607–17.

Landerer, F. W., and S. C. Swenson. 2012. “Accuracy of Scaled GRACE Terrestrial Water Storage Estimates.” *Water Resources Research* 48 (4): W04531.

Lane, Charles R., and Ellen D’Amico. 2010. “Calculating the Ecosystem Service of Water Storage in Isolated Wetlands Using LiDAR in North Central Florida, USA.” *Wetlands* 30 (5): 967–77.

Laxon, S. 1994. “Sea Ice Altimeter Processing Scheme at the EODC.” *International Journal of Remote Sensing* 15 (4): 915–24.

Lee, Hyongki. 2008. “Radar Altimetry Methods for Solid Earth Geodynamics Studies.” Ph.D. Dissertation, Ohio State University.

Lee, Hyongki, R. Edward Beighley, Douglas Alsdorf, Hahn Chul Jung, C. K. Shum, Jianbin Duan, Junyi Guo, Dai Yamazaki, and Konstantinos Andreadis. 2011. “Characterization of Terrestrial Water Dynamics in the Congo Basin Using GRACE and Satellite Radar Altimetry.” *Remote Sensing of Environment* 115 (12): 3530–38.

Lee, Hyongki, Hahn Chul Jung, Ting Yuan, R. Edward Beighley, and Jianbin Duan. 2014. “Controls of Terrestrial Water Storage Changes over the Central Congo Basin Determined by Integrating PALSAR ScanSAR, Envisat Altimetry, and GRACE Data.”

In *Remote Sensing of the Terrestrial Water Cycle*, 206:115–29. Hoboken, NJ: John Wiley & Sons, Inc.

Lee, Hyongki, C. K. Shum, Yuchan Yi, Motomu Ibaraki, Jin-Woo Kim, Alexander Braun, Chung-Yen Kuo, and Zhong Lu. 2009. "Louisiana Wetland Water Level Monitoring Using Retracked TOPEX/POSEIDON Altimetry." *Marine Geodesy* 32 (June): 284–302.

Lee, Hyongki, C.K. Shum, Yuchan Yi, Alexander Braun, and Chung-Yen Kuo. 2008. "Laurentia Crustal Motion Observed Using TOPEX/POSEIDON Radar Altimetry over Land." *Journal of Geodynamics* 46 (3): 182–93.

Lee, Hyongki, Ting Yuan, Hahn Chul Jung, and Edward Beighley. 2015. "Mapping Wetland Water Depths over the Central Congo Basin Using PALSAR ScanSAR, Envisat Altimetry, and MODIS VCF Data." *Remote Sensing of Environment* 159: 70–79.

Legresy, Benolt, and Frede Rique Remy. 1997. "Surface Characteristics of the Antarctic Ice Sheet and Altimetric Observation." *Journal of Glaciology* 43 (144): 1–11.

Lehner, B., K. Verdin, and A. Jarvis. 2008. "New Global Hydrography Derived from Spaceborne Elevation Data." *Eos, Transactions American Geophysical Union* 89 (10): 93–94.

Li, Z.W., X.L. Ding, C. Huang, G. Wadge, and D.W. Zheng. 2006. "Modeling of Atmospheric Effects on InSAR Measurements by Incorporating Terrain Elevation Information." *Journal of Atmospheric and Solar-Terrestrial Physics* 68 (11): 1189–94.

Lu, Zhong, Jin-Woo Kim, Hyongki Lee, C. K. Shum, Jianbin Duan, Motomu Ibaraki, Orhan Akyilmaz, and Chung-Hye Read. 2009. "Helmand River Hydrologic Studies Using ALOS PALSAR InSAR and ENVISAT Altimetry." *Marine Geodesy* 32 (3): 320–33.

Lu, Zhong, and Oh-ig Kwoun. 2008. "Radarsat-1 and ERS InSAR Analysis Over Southeastern Coastal Louisiana: Implications for Mapping Water-Level Changes Beneath Swamp Forests." *IEEE Transactions on Geoscience and Remote Sensing* 46 (8): 2167–84.

Marlier, G. 1973. "Limnology of the Congo and Amazon Rivers." In *Tropical Forest Ecosystems in Africa and South America: A Comparative Review*, 223–38. Washington DC: Smithsonian Institution.

Martinez, Jean Michel, and Thuy Le Toan. 2007. "Mapping of Flood Dynamics and Spatial Distribution of Vegetation in the Amazon Floodplain Using Multitemporal SAR Data." *Remote Sensing of Environment* 108: 209–23.

Mattia, Francesco, Thuy Le Toan, J-C. Souyris, C. De Carolis, Nicolas Floury, Franco Posa, and N. G. Pasquariello. 1997. "The Effect of Surface Roughness on Multifrequency Polarimetric SAR Data." *IEEE Transactions on Geoscience and Remote Sensing*.

Mayaux, Philippe, Gianfranco De Grandi, and Jean-Paul Malingreau. 2000. "Central African Forest Cover Revisited." *Remote Sensing of Environment* 71 (2): 183–96.

Mertes, Leal A. K. 1997. "Documentation and Significance of the Perirheic Zone on Inundated Floodplains." *Water Resources Research* 33 (7): 1749.

Minke, Adam G., Cherie J. Westbrook, and Garth Van Der Kamp. 2010. "Simplified

Volume-Area-Depth Method for Estimating Water Storage of Prairie Potholes." *Wetlands* 30 (3): 541–51.

Mitsch, William J., and James G. Gosselink. 2007. *Wetlands*. 4th ed. New York: John Wiley & Sons, Inc.

Nelson, Mark D., Ronald E. McRoberts, and Matthew C. Hansen. 2004. "Forest Land Area Estimates from Vegetation Continuous Fields." In *Remote Sensing for Field Users: Proceedings of the Tenth Biennial Forest Service Remote Sensing Applications Conference*, 5–9. Salt Lake City, Utah.

Neue, H.U., J.L. Gaunt, Z.P. Wang, P. Becker-Heidmann, and C. Quijano. 1997. "Carbon in Tropical Wetlands." *Geoderma* 79 (1–4): 163–85.

O'Loughlin, F., M. A. Trigg, G. J.-P. Schumann, and P. D. Bates. 2013. "Hydraulic Characterization of the Middle Reach of the Congo River." *Water Resources Research* 49 (8): 5059–70.

O'Loughlin, Fiachra E., Jeffrey Neal, Dai Yamazaki, and Paul D. Bates. 2016. "ICESat-Derived Inland Water Surface Spot Heights." *Water Resources Research* 52 (4): 3276–84.

Pope, Kevin O., Eliska Rejmankova, Jack F. Paris, and Robert Woodruff. 1997. "Detecting Seasonal Flooding Cycles in Marshes of the Yucatan Peninsula with SIR-C Polarimetric Radar Imagery." *Remote Sensing of Environment* 59 (2): 157–66.

Prigent, C., F. Papa, F. Aires, W. B. Rossow, and E. Matthews. 2007. "Global Inundation Dynamics Inferred from Multiple Satellite Observations, 1993–2000." *Journal of Geophysical Research* 112 (D12): D12107.

Rapley, C.G., M.A. Guzkowska, W. Cudlip, and I.M. Mason. 1987. “An Exploratory Study of Inland Water and Land Altimetry Using SEASAT Data.” http://agris.fao.org/agris-search/search.do?recordID=US201300446403#.V1X3FP-wCzg.mendeley.

Richey, Jeffrey E., Leal A. K. Mertes, Thomas Dunne, Reynaldo L. Victoria, Bruce R. Forsberg, Antônio CNS Tancredi, and Eurides Oliveira. 1989. “Sources and Routing of the Amazon River Flood Wave.” *Global Biogeochemical Cycles* 3 (3): 191–204.

Roberts, Tyson R., and Donald J. Stewart. 1976. “An Ecological and Systematic Survey of Fishes in the Rapids of the Lower Zaire or Congo River.” *Bulletin of the Museum of Comparative Zoology* 147 (6): 239–317.

Rosenqvist, Å., and C. M. Birkett. 2002. “Evaluation of JERS-1 SAR Mosaics for Hydrological Applications in the Congo River Basin.” *International Journal of Remote Sensing* 23 (7): 1283–1302.

Rosenqvist, Ake. 2008. “Mapping of Seasonal Inundation in the Congo River Basin Using PALSAR ScanSAR.” In *2nd ALOS PI Symposium*. Rhodes, Greece.

Rosenqvist, Ake, Masanobu Shimada, Norimasa Ito, and Manabu Watanabe. 2007. “ALOS PALSAR: A Pathfinder Mission for Global-Scale Monitoring of the Environment.” *IEEE Transactions on Geoscience and Remote Sensing* 45 (11): 3307–16.

Save, Himanshu, Srinivas Bettadpur, and Byron D. Tapley. 2016. “High-Resolution CSR GRACE RL05 Mascons.” *Journal of Geophysical Research: Solid Earth* 121 (10): 7547–69.

Scanlon, Bridget R., Claudia C. Faunt, Laurent Longuevergne, Robert C. Reedy, William M. Alley, Virginia L. McGuire, and Peter B. McMahon. 2012. “Groundwater

Depletion and Sustainability of Irrigation in the US High Plains and Central Valley." *Proceedings of the National Academy of Sciences of the United States of America* 109 (24): 9320–25.

Schmitt, Christine B., Neil D. Burgess, Lauren Coad, Alexander Belokurov, Charles Besançon, Lauriane Boisrobert, Alison Campbell, et al. 2009. "Global Analysis of the Protection Status of the World's Forests." *Biological Conservation* 142 (10): 2122–30.

Shimada, Masanobu, Osamu Isoguchi, Takeo Tadono, and Kazuo Isono. 2009. "PALSAR Radiometric and Geometric Calibration." *IEEE Transactions on Geoscience and Remote Sensing* 47 (12). IEEE: 3915–32.

Silva, Joecila Santos Da, Frédérique Seyler, Stéphane Calmant, Otto Corrêa Rotunno Filho, Emmanuel Roux, Afonso Augusto Magalhães Araújo, and Jean Loup Guyot. 2012. "Water Level Dynamics of Amazon Wetlands at the Watershed Scale by Satellite Altimetry." *International Journal of Remote Sensing* 33 (11): 3323–53.

Sita, P. 1968. "Etude Préliminaire de La Végétation de L'île M'Bamou." Brazzaville, ORSTOM.

Swenson, Sean, and John Wahr. 2006. "Post-Processing Removal of Correlated Errors in GRACE Data." *Geophysical Research Letters* 33 (8): L08402.

Tapley, Byron D., Srinivas Bettadpur, John C. Ries, Paul F. Thompson, and Michael M. Watkins. 2004. "GRACE Measurements of Mass Variability in the Earth System." Science 305 (5683): 503–5.

Tateishi, Ryutaro, Bayaer Uriyangqai, Hussam Al-Bilbisi, Mohamed Aboel Ghar,

Javzandulam Tsend-Ayush, Toshiyuki Kobayashi, Alimujiang Kasimu, Nguyen Thanh Hoan , Adel Shalaby , Bayan Alsaaideh , Tsevengee Enkhzaya et al. 2010. "Production of Global Land Cover Data – GLCNMO." *International Journal of Digital Earth* 4 (1): 22–49.

Thieme, Michele L., Robin Abell, Neil Burgess, Bernhard Lehner, Eric Dinerstein, and David Olson. 2005. *Freshwater Ecoregions of Africa and Madagascar: A Conservation Assessment*. Washington (DC): Island Press.

Toan, Thuy Le, Florence Ribbes, Li-Fang Wang, Nicolas Floury, Kung-Hau Ding, Jin Au Kong, Masaharu Fujita, and Takashi Kurosu. 1997. "Rice Crop Mapping and Monitoring Using ERS-1 Data Based on Experiment and Modeling Results." *IEEE Transactions on Geoscience and Remote Sensing* 35 (1): 41 – 56.

Tockner, K., F. Malard, and J. V. Ward. 2000. "An Extension of the Flood Pulse Concept." *Hydrological Processes* 14 (16–17): 2861–83.

Tockner, Klement, and Jack A. Stanford. 2002. "Riverine Flood Plains: Present State and Future Trends." *Environmental Conservation* 29 (3): 308–30.

Trung, Van Nguyen, Jung Hyun Choi, and Joong Sun Won. 2013. "A Land Cover Variation Model of Water Level for the Floodplain of Tonle Sap, Cambodia, Derived from ALOS PALSAR and MODIS Data." *IEEE Journal of Selected Topics in Applied Earth Observations and Remote Sensing* 6 (5): 2238–53.

Vörösmarty, Charles J., Berrien Moore, Annette L. Grace, M. Patricia Gildea, Jerry M. Melillo, Bruce J. Peterson, Edward B. Rastetter, and Paul A. Steudler. 1989. "Continental Scale Models of Water Balance and Fluvial Transport: An Application

to South America." *Global Biogeochemical Cycles* 3 (3): 241–65.

Ward, J.V., Klement Tockner, and Fritz Schiemer. 1999. "Biodiversity of Floodplain River Ecosystems: Ecotones and connectivity1." *Regulated Rivers: Research & Management* 15 (1–3): 125–39.

Wdowinski, Shimon, Sang-Wan Kim, Falk Amelung, Timothy H. Dixon, Fernando Miralles-Wilhelm, and Roy Sonenshein. 2008. "Space-Based Detection of Wetlands' Surface Water Level Changes from L-Band SAR Interferometry." *Remote Sensing of Environment* 112: 681–96.

Wegmuller, U. 1999. "Automated Terrain Corrected SAR Geocoding." In *IEEE 1999 International Geoscience and Remote Sensing Symposium*, 3:1712–14. Hamburg: IEEE.

Werner, Charles, Urs Wegmüller, Tazio Strozzi, and Andreas Wiesmann. 2000. "Gamma SAR and Interferometric Processing Software." In *Proc. ERS-Envisat Symp*. Vol. 461. Gothenburg, Sweden: Citeseer.

Wilson, Matthew D., Paul Bates, Doug Alsdorf, Bruce Forsberg, Matthew Horritt, John Melack, Frédéric Frappart, and James Famiglietti. 2007. "Modeling Large-Scale Inundation of Amazonian Seasonally Flooded Wetlands." *Geophysical Research Letters* 34: 4–9.

Wingham, D. J., C. G. Rapley, and H. Griffiths. 1986. "New Techniques in Satellite Altimeter Tracking Systems." In *ESA Proceedings of the 1986 International Geoscience and Remote Sensing Symposium(IGARSS'86) on Remote Sensing: Today's Solutions for Tomorrow's Information Needs*. Vol. 3.

Yuan, Ting, Hyongki Lee, and Hahn Chul Jung. 2015. “Toward Estimating Wetland Water Level Changes Based on Hydrological Sensitivity Analysis of PALSAR Backscattering Coefficients over Different Vegetation Fields.” *Remote Sensing* 7 (3): 3153–83.

Zebker, H. A., and J. Villasenor. 1992. “Decorrelation in Interferometric Radar Echoes.” *IEEE Transactions on Geoscience and Remote Sensing*.

Zwally, H. Jay. 1996. “GSFC Retracking Algorithms.” http://icesat4.gsfc.nasa.gov/.

Appendix I

Based on Figure 5-6(a), the water storage in the floodplain can be expressed as:

$$V(d_{max}^t) = L_f \cdot A_{cross-section}(d_{max}^t), \quad \text{(S 1)}$$

where $V(d_{max}^t)$ is water volume with maximum water depth d_{max}^t, L_f is the floodplain length along the river, $A_{cross-section}(d_{max}^t)$ is the averaged area of floodplain cross section when maximum water depth is d_{max}^t.

We followed power function proposed in *Hayashi and Van Der Kamp* (2002) to characterize the floodplain cross-section slope. Following *Hayashi and Van Der Kamp* (2002), the cross-section slope profiles are:

$$y/y_0 = (r/r_0)^p, \quad \text{(S 2)}$$

where y is the relative elevation of floodplain floor with respect to cross-sectional lowest floodplain floor at a distance r from the river; y_0 is the unit elevation; r_0 is the distance to the river corresponding to y_0, thus representing the floodplain width when y_0 is equal to 1 m; p is the shape coefficient.

Then, when maximum water depth equals to d_{max}^t, the averaged floodplain cross-sectional area represented in Figure 5-6(a) can be estimated using:

$$A_{cross-section}(d_{max}^t) = \int_0^{d_{max}^t} r(y)dy. \quad \text{(S 3)}$$

Rewriting Equation(S 2),

$$r = (\frac{y}{y_0})^{\frac{1}{p}} r_0. \quad \text{(S 4)}$$

Substituting Equation (S 4) into Equation (S 3), we can get

$$A_{cross-section}(d_{max}^{t}) = \int_{0}^{d_{max}^{t}} (\frac{y}{y_0})^{\frac{1}{p}} r_0 dy = \frac{r_0}{(1+\frac{1}{p})} \cdot \frac{(d_{max}^{t})^{1+1/p}}{y_0^{1/p}}. \quad \text{(S 5)}$$

Substituting Equation (S 5) into Equation (S 1), water storage can be written as:

$$V(d_{max}^{t}) = L_f \cdot \frac{r_0}{(1+\frac{1}{p})} \cdot \frac{(d_{max}^{t})^{1+1/p}}{y_0^{1/p}}. \quad \text{(S 6)}$$